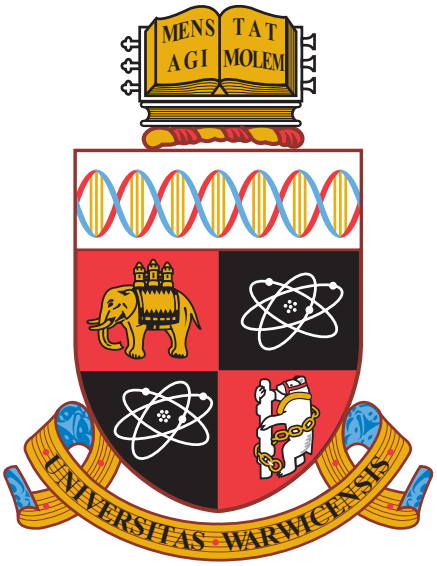

An Investigation of the Relationship Between the Structure and Properties of Some Stacked Perovskites

by

Dean Samuel Keeble

Thesis

Submitted to the University of Warwick

for the degree of

Doctor of Philosophy

Department of Physics

September 2009

THE UNIVERSITY OF WARWICK

Contents

List of Tables

List of Figures

List of Videos

On the attached CD the reader will find videos of the variable-temperature birefringence of a selection of materials covered in this study, as recorded using the Metripol software. The included videos are;

`SrBi2Nb2O9-sind.avi` False-colour image of $|\sin\delta|$ for $SrBi_2Nb_2O_9$

`SrBi2Ta2O9-sind.avi` False-colour image of $|\sin\delta|$ for $SrBi_2Ta_2O_9$

The videos comprise of false colour images representing $|\sin\delta|$ at various temperatures stitched together to form a visual representation of the birefringence of the crystal upon heating. The temperature is given in the legend in the top left corner. The scale of $|\sin\delta|$ is seen below.

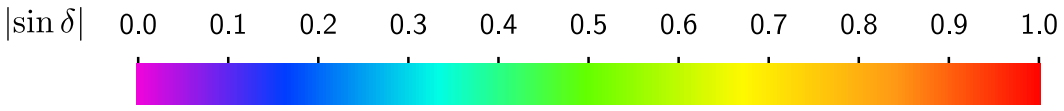

Acknowledgments

I would like to begin by expressing my heartfelt gratitude to my supervisor, Professor Pam Thomas, whose support and guidance has ensured that my studies have been well directed. In more recent times, her relentless use of red ink has hopefully ensured that this thesis reads fluently and that-there-are-no-incorrect-hyphens.

A great man once said that any experiment is only as good as the sample it is performed on, to which end my thanks must go to Professor Phil Lightfoot, Dr Richard Goff, and Dr Jess Marshall, all of whom supplied or aided in the synthesis of the samples in this work. This study formed part of an EPSRC project (EP/C008243/1), and so I thank them, and Advantage West Midlands, for funding and provision of equipment.

My thanks also to Dr David Walker and Mr Daniel Baker, for the many hours spent discussing strange results, and coming to strange conclusions. Thanks also to those that have had the pleasure of sharing an office with me; Ben, Emma, Robin, James, Kaustuv, Jeppe, Sem, Martin, Aoife, Iain: all of whom have shown me—in one way or another—what it means to be a good researcher.

On a more personal note, I must thank Nikki and Alex for their fine hospitality, members of the Warwick ten-pin bowling club for their fine socializing, and Ben and Dan for the fine golf they play.

Finally, there are those without whom this thesis would not even have been possible; my Mum and Dad, whose endless support and patience have been nothing short of remarkable, and my girlfriend Laura, who has ensured that the last four years have been the happiest in my life.

Declaration and published work

I declare that, to the best of my knowledge, the material in this thesis is my own original work unless otherwise stated, and has not been submitted in application for any other degree. Elements of this material have been presented at conferences and published in journals, details of which can be seen in Appendix C.

Abstract

This thesis discusses a comprehensive study of the structure and properties of selected stacked perovskites using non-ambient powder and single-crystal x-ray diffraction, powder neutron diffraction, birefringence microscopy and dielectric spectroscopy. The major portion of this work focuses on materials forming in Aurivillius phases, with the general chemical formula $[Bi_2O_2]^{2+}[A_{n-1}B_nO_{3n+1}]^{2-}$, and containing n perovskite layers sandwiched between fluorite-like interstices. Comparisons are made between the structure and properties of the isomorphous materials $SrBi_2Nb_2O_9$ and $BaBi_2Nb_2O_9$, and the ferroelectric phase transition in $SrBi_2Nb_2O_9$ is compared to that in $SrBi_2Ta_2O_9$. The latter shows two distinct phase transitions upon cooling from the high temperature phase: a ferroelastic transition to space group $Amam$ at 848 K, followed by a ferroelectric transition to $A2_1am$ at 608 K. By contrast, the transition in $SrBi_2Nb_2O_9$ does not go *via* the intermediate $Amam$ phase, as is demonstrated using both structural and property measurements. It is also shown that in a material that is both ferroelectric and ferroelastic, the individual contributions to the birefringence of strain and polarization can be isolated using birefringence microsocopy by applying the principles of Landau theory to extract the two contributions. The structure and properties of a number of other materials within the general class of ferroelectrics are investigated using similar techniques, in particular, single-crystal x-ray diffraction is used to reinvestigate the room-temperature structure of $BaTiO_3$ following prominent reports of monoclinicity of this phase. Quantitative investigation of the (101) ferroelastic twinning in these crystals was also undertaken. In addition, evidence for the existence of a ferroelectric phase transition in $CsBiNb_2O_7$ is derived from the results of powder neutron diffraction as a function of temperature. The effect of substituting fluorine on to the anion site on both the structure and properties of ferroelectric stacked perovskites is also investigated, and is shown to have a radical effect on the the ferroelectric properties of the material, as well as on their phase formation.

Glossary and abbreviations

ADP(s)	Atomic Displacement Parameter(s)
CCD	Charge Coupled Device
CF	Charge Flipping
FWHM	Full-width-at-half-maximum
OA	Optic Axis
NMR	Nuclear Magnetic Resonance
PND	Powder Neutron Diffraction
SOF	Site Occupancy Factor
XRD	X-ray Diffraction
SBN	$SrBi_2Nb_2O_9$
BBN	$BaBi_2Nb_2O_9$
CsBN	$CsBiNb_2O_7$

Hominem unius libri timeo.

"I fear the man of a single book"

- Thomas Aquinas

Chapter 1

Introduction

1.1 Aurivillius Phases

1.1.1 The Perovskite structure

For decades it has been known that many members of the perovskite family of materials exhibit a significant number of interesting properties. These properties include ferroelectricity and piezoelectricity, and it for this reason that they have been the focus of many studies. The basic perovskite structure is shown in figure 1-1. Perovskites form with the general formula ABX_3, where A is a large, usually mono- or divalent cation, typically an alkaline, alkaline earth, or rare earth metal, and B is a significantly smaller cation, usually a transition metal. X is an anion and is usually oxygen, but may be a halogen. In the ideal prototypic phase, perovskites form in the cubic space group $Pm\bar{3}m$, with the anions occupying the face centres $(0,\frac{1}{2},\frac{1}{2};\ \frac{1}{2},\frac{1}{2},0;\ \frac{1}{2},0,\frac{1}{2})$, forming octahedra. The larger A cation occupies the 12 coordinated corner sites (0,0,0), and the smaller B cation occupies the 8 coordinated body centre positions $(\frac{1}{2},\frac{1}{2},\frac{1}{2})$.

Perovskites have the potential to exhibit many structural properties because of the large range of ionic sizes that can be accommodated into the structure. Whilst the valencies stated above are commonplace, ions of different valencies can and do exist in the perovskite phase. Megaw [1] hypothesized that the ionic radii r_A, r_B and r_X should be connected *via* a simple geometric relationship;

$$r_A + r_X = t\sqrt{2}\,(r_B + r_X) \tag{1-1}$$

where t is the tolerance factor, which for a ferroelectric has a value of $0.78 < t < 1.05$[2]. This result, which shows that the sum of two neighbouring ions can be only 3/4 of what is ideal, demonstrates how adaptable the perovskite structure is.

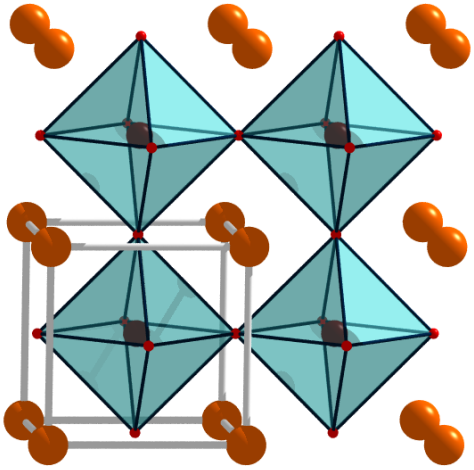

Figure 1-1: A schematic of the prototypic perovskite unit cell. The corners are the referred to as the "A-site", the cell centre as the "B-site", with anions occupying the face centres, to form octahedra.

1.1.2 Structural Distortions

Although many examples of the prototypic P$m\bar{3}m$ do exist in nature, many more examples of perovskites with lower symmetry exist, especially at room temperature and below. The lower symmetry arises from some distortion of the structure, which may be one or a combination of the following [3];

i. Displacements of the cations from the centre of their co-ordination polyhedra;
ii. Distortion of the anion octahedra;
iii. Tilting of the anion octahedra with respect to the cation framework;
iv. Cation ordering, in complex perovskites where multiple cations partially occupy the same site.

It is this wide range of potential distortions that lead to the large number of properties exhibited by perovskites and perovskite-containing structures.

1.1.3 Stacked Perovskites

Since perovskites are relatively simple structural units (the prototypic cubic cell has typically $a \approx 4\,\text{Å}$), there exist many phases that incorporate perovskite units

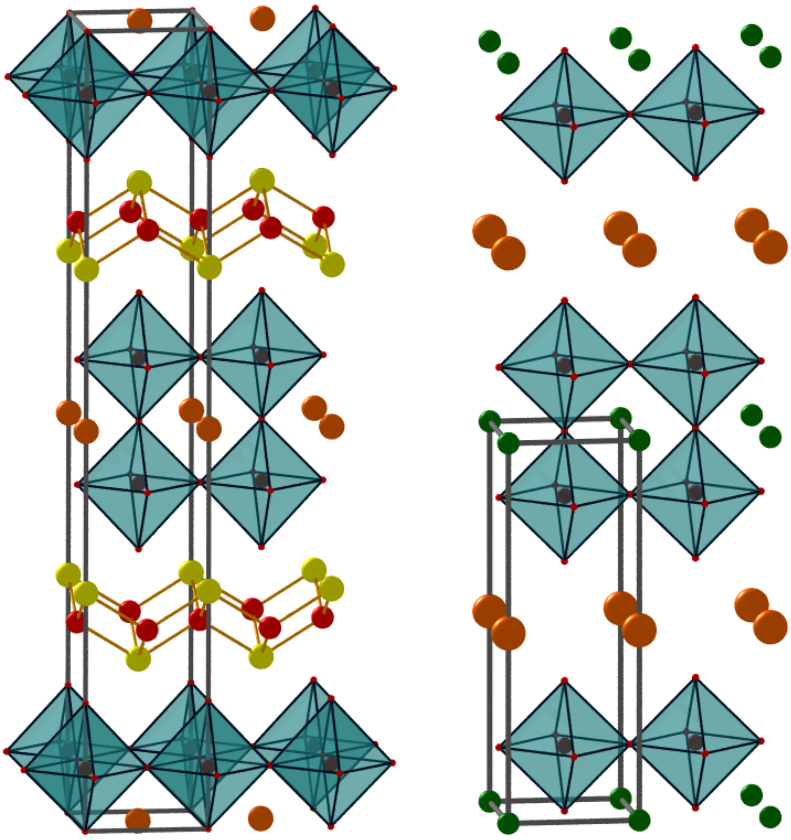

(a) Aurivillius (b) Dion-Jacobson

Figure 1-2: Schematics of the $n = 2$ prototypic Aurivillius and Dion-Jacobson phases. The Aurivillius phase (figure (a)) has formula $ABi_2B_2X_9$, where A is orange, Bi is yellow, B is maroon and O is red. The Dion-Jacobson phase (figure (b) has formula $A'AB_2O_7$, where A' is orange, A is green, B is maroon, and O is red.

in a larger structural framework. Many of these larger phases can be classified as stacked perovskites, that is where two of the lattice parameters are equal to, or a multiple of, the basic perovskite dimension of 4 Å. The third lattice parameter is lengthened by the introduction of extra structure, which takes the form of sheets that separate sections of perovskite blocks. This sheet may be something as simple as a square grid of cations, as is the case for the Dion-Jacobson structure, or more complicated such as the fluorite-like layer in the Aurivillius phase. The prototypic structure of both of these phases is seen in figure 1-2.

An Aurivillius material with n perovskite blocks per fluorite layer has the general chemical formula $[Bi_2O_2]^{2+}[A_{n-1}B_nO_{3n+1}]^{2-}$, where $[Bi_2O_2]^{2+}$ is the formula for the fluorite layer, and $[A_{n-1}B_nO_{3n+1}]^{2-}$ the perovskite layer. A and B represent

the A- and B-sites of the basic perovskite phase, and the same principles for the selection of the cations apply as for the perovskite structure. The perovskite blocks in adjacent layers are sheared with respect to each other along $\frac{1}{2}[111]$.

The Dion-Jacobson phase is another stacked perovskite, which has the formula $[A']^{2+}[A_{n-1}B_nO_{3n+1}]^{2-}$. A' is a divalent cation, that forms in a "2-dimensional" grid, with spacing equivalent to the A-site within the perovskite block (hence the denotation A'). The simplicity of the interstitial layer means that no shear transformation exists between adjacent perovskite blocks, and so the stacking-direction unit cell parameter is usually shorter, close to half of that of an Aurivillius structure of the same n. The isolation of the perovskite sheets from each other means that in these phases there are more possible types of distortion and therefore the potential for properties not observed in the basic perovskites.

1.2 Ferroelasticity, Ferroelectricity, and Structural Phase Transitions

1.2.1 Ferroelectricity

The technologically important phenomenon of ferroelectricity has been found to be relatively common in perovskites, and stacked perovskites such as the Aurivillius phase, when compared with other structures. A ferroelectric material displays a spontaneous polarization, P_s, that is reversible upon the application of an external electric field. A pyroelectric is a material that has a polarization that is temperature dependent but one that is not necessarily reversible, and so a ferroelectric is also a pyroelectric. A piezoelectric is a material that exhibits an electrical polarity when subject to an external stress, and conversely exhibits a strain in response to an applied electric field. The effect is observed in all except one of the 21 non-centrosymmetric crystallographic point groups, and 10 of these exhibit a polar direction; it is these latter groups that are pyroelectric.

One of the defining characteristics of a ferroelectric is the existence of hysteresis in the response to an electric field. A typical hysteresis is seen in figure 1-3. The

magnitude of the external field required to reverse the polarization is known as the coercive field, E_c.

As discussed in section 1.1, the perovskite and related structures can undergo a large number of structural distortions which can lead to ferroelectric behaviour. Ignoring melting and decomposition that may occur, any structure distorted from a theoretical prototype has the potential to undergo a transition to higher symmetry upon heating. This transition is observed in many ferroelectrics, and in the proximity of such a transition, the material demonstrates enhanced properties; the dielectric constant of $BaTiO_3$ increases 10-fold in a 10 kelvin region approaching the transition temperature. The temperature at which the polarization falls to zero is referred to as the Curie temperature, or Curie point, T_c. Thermodynamically, this change in structure is defined by the order parameter, η. The primary order parameter in a ferroelectric phase transition is the polarization, but the form of the order parameter can often be expressed *via* one or more structural coordinate. It then follows that the order parameter is zero in the prototypic phase, and is non-zero in the ferroelectric phase, and the form of $\eta(T)$ defines the type of transition. If $\frac{\partial g}{\partial T}$ is discontinuous, then the transition is said to be first order. If $\frac{\partial g}{\partial T}$ is continuous, but $\frac{\partial^2 g}{\partial T^2}$ is discontinuous, then the transition is said to be second

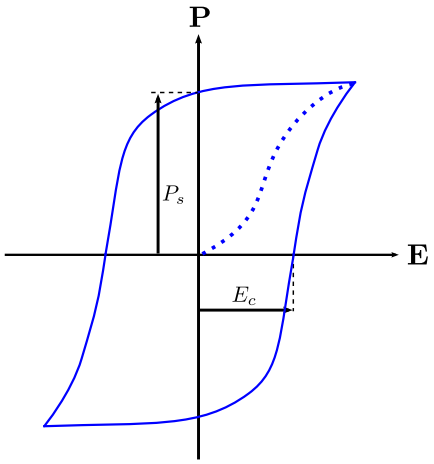

Figure 1-3: A typical hysteresis curve seen in a ferroelectrics' response to an applied electric field. Marked on the diagram is the path from zero to non-zero net polarization upon application of a field of positive **E**. Also marked is the value of the coercive field, E_c, and the spontaneous polarization, P_s.

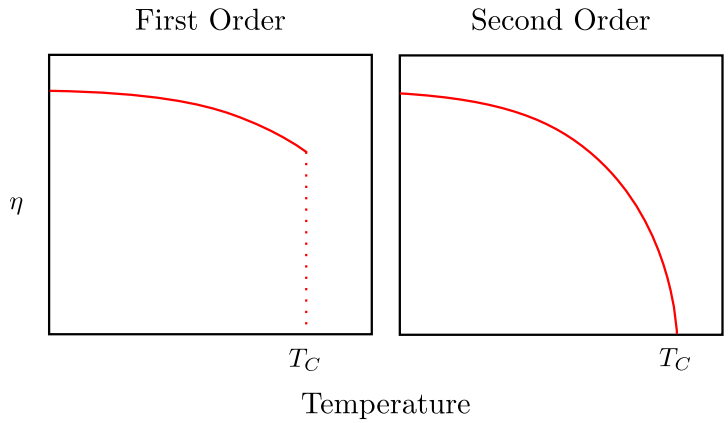

Figure 1-4: The order parameter for first and second order transitions. A first order transition shows a discontinuity at the phase transition.

order. The idealized behaviour of the order parameter for perfect first and second order phase transitions can be seen in figure 1-4.

When a material cools from the high-temperature, prototypic phase, to a low-temperature, ferroelectric phase, there is no energetic predisposition for the polarization direction within a crystal, from all of the symmetry-allowed possibilities. For this reason, there are always at least two possible orientations of the polarization, all of which will be present in various areas within the unpoled sample. These areas are known as ferroelectric domains and the boundaries between them are known as domain walls. When a suitably large external field is applied to the crystal, domain walls "propagate" through the material, with energetically favourable domains growing at the expense of the others. This is the process that is defined by the blue line in figure 1-3. It is the force required to move the domain wall that effects the coercive field.

1.2.2 Ferroelasticity

Because of the distortions of the unit cell that accompany a ferroelectric phase transition, as well as exhibiting a spontaneous polarization, P_s, a ferroelectric can also have a spontaneous strain, ϵ_s. This strain is due to the elongation or contraction of one or more of the lattice parameters, that is symptomatic of a reduction in the Laue group of the crystal *i.e.* from cubic to tetragonal. If the applica-

tion of an external mechanical stress can switch the structure to another stable enantiomorph, then parallels can obviously be drawn with other ferroics. If this is the case the material is said to be ferroelastic. When a material is brought from the high temperature prototypic phase to a ferroelectric state through a ferroelectric and ferroelastic phase transition then the material will contain ferroelastic domains as well as ferroelectric domains.

1.2.3 Soft Modes

The mechanisms behind a ferroelectric phase transition can be thought of by considering a phonon mode within the crystal that becomes unstable. This soft mode reduces in frequency with temperature because of the restoring force causing the oscillation being reduced. At some critical temperature, the restoring force becomes so low that the frequency of the soft mode goes to zero, and a defect is frozen in to the structure. A soft optic mode at the Brillouin zone centre is associated with a cation displacement, and a soft optic mode at the zone boundary is associated with a cell-doubling transition caused by oxygen octahedra tilting or antiferroelectric displacements of the cations. An acoustic soft mode is associated with a ferroelastic phase transition. The slope of the soft mode, which is proportional to the speed of sound and the square root of one of the elastic constants, goes to zero in this case.

1.2.4 Landau Theory

The nature of a phase transition can be easily studied if the free energy of the system is analysed. This is the principle behind Landau theory, which is a very powerful framework for studying the thermodynamics of phase transitions. If one considers the Helmholtz free energy as a function of the order parameter, $F(\eta)$, of a material that undergoes a second order phase transition, then one can make the following observations [4, 5]. Firstly, we can stipulate that at some temperature well above T_c, in the prototypic phase, no distortions are present, and so the free energy minima must be at $\eta = 0$. Conversely, at some temperature well below the phase transition, the free energy must have minima at some non-zero value

of η. If the order parameter is in fact the polarization, then the free energy must be identical for the two polarization states, and hence $F(\eta) = F(-\eta)$. For this reason, the free energy function must be symmetric about $\eta = 0$, and so the Landau expansion cannot contain any odd powers of the order parameter. At temperatures above the phase transition, the free energy will have the form:

$$F(\eta) = F_0 + \frac{1}{2}A\eta^2 + \dots \tag{1-2}$$

where A is a positive coefficient, and F_0 is the free energy of the system that is invariant across the transition. At a temperature below the phase transition, the free energy will have a minimum at a non-zero value of η, and so the coefficient A must be a function of temperature, and change sign at T_c. In a second order transition, we see that the order parameter moves gradually from zero to non-zero at T_c, and so we can suggest that $A(T) = a(T - T_c)$. Applying this to equation 1-2, and including fourth order terms to ensure the required form of the free energy gives:

$$F(\eta) = F_0 + \frac{a}{2}(T - T_c)\eta^2 + \frac{b}{4}\eta^4 + \dots \tag{1-3}$$

The form of this low-temperature free energy, and the high-temperature energy seen in equation 1-2, is shown in figure 1-5. Landau theory then predicts the solution of equation 1-3, to give:

$$\eta = (a/b)^{1/2}(T_c - T)^{\beta} \tag{1-4}$$

where β is a critical exponent, which defines the temperature-dependent behaviour of the order parameter, η. Accompanying the schematics of the free energy for the second-order transition are those for the first-order transition, which show the differences between the two types of transition in terms of the free energy. In a first-order phase transition, where there is a discontinuity in the value of the order parameter at T_c, there must be a temperature at which there exist three minima in the free energy: the minimum at $\eta = 0$, and the two minima associated with the low-temperature phase. Only a small modification of equation 1-3 is required to model this, *i.e.* a changing of the sign of the coefficient of the fourth order term:

$$F(\eta) = F_0 + \frac{a}{2}(T - T_c)\eta^2 - \frac{b}{4}\eta^4 + \frac{c}{6}\eta^6 + \dots \tag{1-5}$$

which allows for the free energy to have 3 minima at $T = T_c$.

1.3 Literature Review

1.3.1 The Aurivillius Structure

The Aurivillius structure, which is closely related to the other stacked perovskites such as Dion-Jacobsen and Ruddleston-Popper phases, was first reported by Aurivillius [6] in 1949. Publications on Aurivillius materials have always been dwarfed in number by studies on the more common basic Perovskites, however the number of publications regarding the two related structures have followed similar trends, as seen in figure 1-6. The first major structural study on a range of Aurivillius materials was published in 1959 by Smolenski et al. [7]. They tentatively suggested A-site cation disorder to explain the very broad phase transition observed in the seemingly centrosymmetric $BaBi_2Nb_2O_9$, and also observed that many Aurivillius structures were ferroelectric. Subbarao [8] and Newnham et al. [9] both continued the work into the Aurivillius phases, with Subbarao [8] disagreeing with Smolenski et al. [7] and their suggestion of cation disorder, asserting that only bismuth may occupy the metal fluorite site. Newnham et al. [9] studied the origin of ferroelectricity in these materials, using combined x-ray and neutron diffraction to do so. Their results showed that the major polar distortion in the Aurivillius phase was

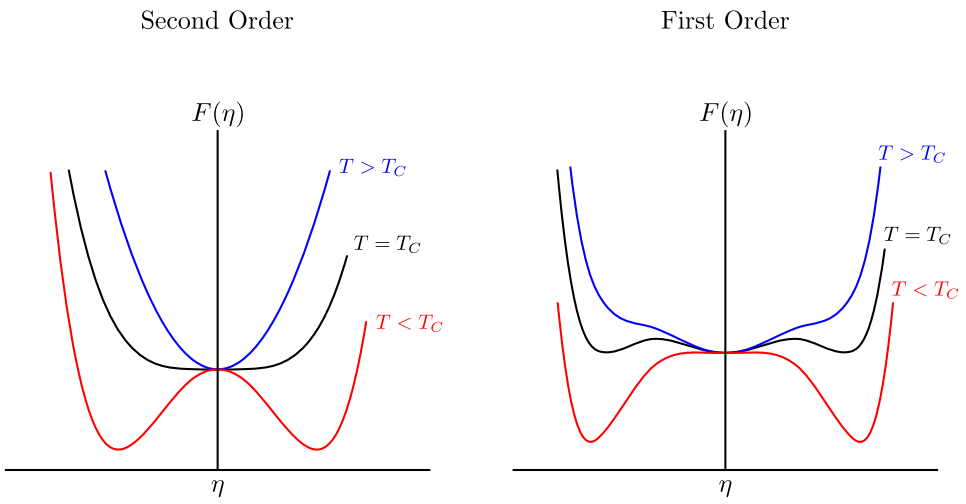

Figure 1-5: Free-energy potentials for first and second order phase transitions at temperatures below, at, and above the transition temperature T_c.

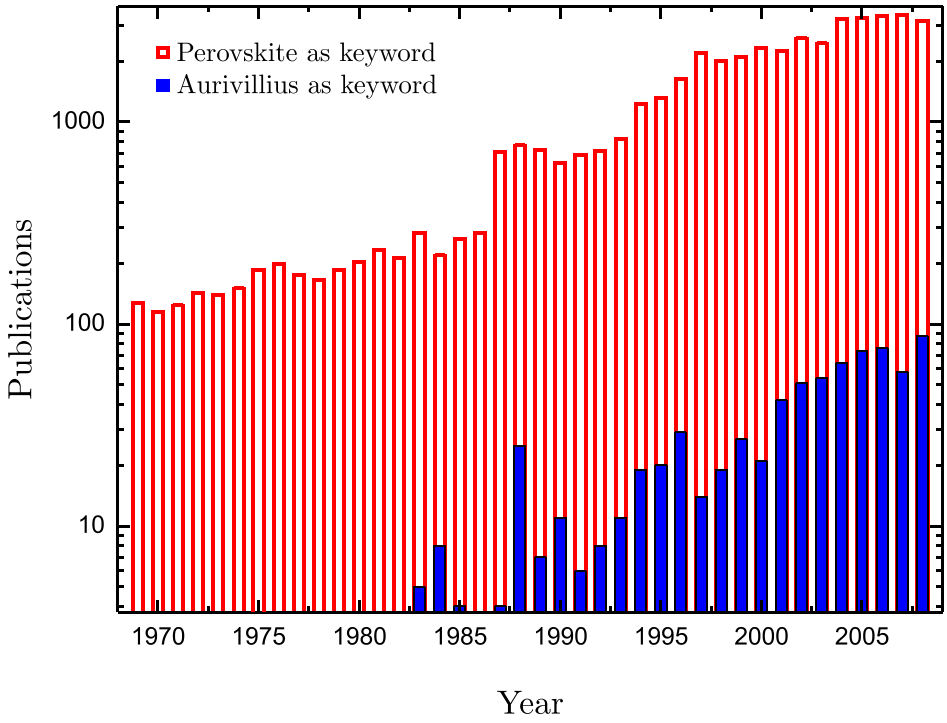

Figure 1-6: The number of publications per year with the keywords "perovskite" and "Aurivillius" from 1969 to 2008. *Source: Engineering Village*

a displacement of the octahedral cation, and that the oxygen octahedral tilting was of great significance. Upon further study of the octahedral tilts, Newnham et al. [9] also suggested that these were the reason odd- and even-order phases seem to exhibit different space groups, with the odd-order phases adopting space group $B2eb$ and the even-order $A2_1am$. They attributed the difference in the space groups to the loss of different symmetry operations from the high temperature $I4/mmm$ phase. Newnham et al. [9] also utilised birefringence microscopy to study the phase transition in $SrBi_2Ta_2O_9$, and suggested for the first time that some Aurivillius ferroelectric to paraelectric phase transitions went in two stages, *via* an "intermediate phase".

Perovskites and Aurivillius phases saw a rise in interest toward the end of the 1980s, and it was at this point that the current understanding of these materials started to form. In the early 1990s, Rae, Thompson, and Withers [10–13] performed extensive structural studies on several Aurivillius materials. They concluded that the main polar distortion in these phases was an A-site cation dis-

Table 1-1: Electron numbers and coherent bound neutron scattering lengths [16] for various elements used in this study.

Element	Z	Z/Z_{Bi}	b fm	b/b_{Bi}
Sr	38	45.8%	7.02	82.3%
Ba	56	67.5%	5.07	59.4%
Bi	83	100.0%	8.532	100.0%
Nb	41	49.4%	7.054	82.7%
Ta	73	88.0%	6.91	81.0%
O	8	9.6%	5.803	68.0%
F	9	10.84%	5.654	66.3%

placement, in disagreement with the previous suggestion of Newnham et al. [9], using a model of a modulated *Fmmm* structure for $Bi_4Ti_3O_{12}$ (n=3), Bi_3TiNbO_9 (n=2), and Bi_2WO_6 (n=1) [13]. Ismunandar et al. [14] performed neutron diffraction on $SrBi_2Nb_2O_9$ and $BaBi_2Nb_2O_9$, and refined the structure of $BaBi_2Nb_2O_9$ in $A2_1am$, seemingly solving the problem of its apparent centre of symmetry. In this work, very large atomic displacement parameters were refined on the bismuth site in the fluorite layer of $SrBi_2Nb_2O_9$, which was attributed to the "unusually open geometry of the bismuth site". In this study, Ismunandar et al. [14] did not allow disorder of the A-site cations on to the fluorite cation site. This model was rejected by Blake et al. [15], who used combined x-ray and neutron diffraction in their study of $ABi_2Nb_2O_9$. They also reported the observation of large atomic displacement parameters on the bismuth site, until they allowed the cations to disorder, whilst constraining the atomic displacement parameters of two different cations on the same site to be equal. They pointed out that the neutron scattering lengths of the atoms in these materials meant that a combined study would be more sensitive to the subtle changes in the structure factors caused by cation mixing. The atomic number and neutron scattering length of elements common in this study are shown in table 1-1.

Blake et al. [15] noted that the orthorhombicity of the $ABi_2Nb_2O_9$ materials increased with decreasing A-site cation size, with the Ba compound being tetragonal. In 1999, in response to Blake et al. [15], Ismunandar and Kennedy [17]

published another structural study of the cation disorder in the strontium and barium bismuth niobates, in contradiction to their previous work that had asserted that no cation disorder was present. They also acknowledged that $BaBi_2Nb_2O_9$ formed in a tetragonal space group, instead of the previously used $A2_1am$. Blake had suggested that the two sets of results may have yielded different results with respect to the cation disordering because of the sample preparation conditions, so this was investigated. A small dependence on the "quenching" temperature of the orthorhombicity, cell volume, and cation disorder were found. Also in this thermal structural study a small discontinuity was observed in the cell volume of $SrBi_2Nb_2O_9$ at T_c (between the measurements at 673 K and 723 K), however the data were too coarse in temperature to suggest anything meaningful about the transition. This study also notes that there is no noticeable discontinuity in the volume of $BaBi_2Nb_2O_9$. Blake et al. [15] had postulated that the cause behind the cation disorder was the need to overcome the relative overbonding of the A-site, and underbonding of the B-site, and whilst this is touched upon by Ismunandar and Kennedy [17], no comment is made on whether this is the driving force behind this disorder. However, what is observed is that for this type of cation disorder, *ca.* 20% disorder is feasible without any real distortion of the structure, a phenomenon which is believed to be due to the very open stereochemical environment occupied by the bismuth cation.

1.3.2 $SrBi_2Nb_2O_9$

The Curie temperature T_c of $SrBi_2Nb_2O_9$ has also been discussed at length in the literature. Estimates range from as little as 691 K [18] to as high as 723 K, [19], but most now agree that it is close to 713 K [20]. An isostructural analogue of $SrBi_2Nb_2O_9$ is $SrBi_2Ta_2O_9$ which is reported to undergo a two stage phase transition [21, 22], at 573 K - 593 K [20, 23–26], comprising of a ferroelastic and a ferroelectric transition. An intermediate phase of symmetry $Amam$ is postulated [27], leading to the hypothesis that the upper transition is improper ferroelastic, and the lower transition is proper ferroelectric. This intermediate phase corresponds to the "freezing out" of both a displacive mode and a tilt mode of the

low symmetry phase, leaving a single tilt mode present [28]. The addition of an intermediate phase to this transition allows it to be second order, whereas a direct transformation from the room temperature structure of $A2_1am$ to the high temperature space group $I4/mmm$ must be first order, since the space groups of the prototypic and low temperature phase are not group/subgroup related. In 2003, Snedden et al. [28] performed a powder neutron study of $SrBi_2Nb_2O_9$ to identify which of these two routes the phase transition takes, since previous studies had failed to differentiate between the two. Their study showed no evidence of a second order phase transition in $SrBi_2Nb_2O_9$, or an intermediate phase. However, the relatively coarse steps in temperature mean that a single-step phase transition can only be alluded to, and an intermediate phase cannot be precluded from this study. What is concluded though is that since T_c for $SrBi_2Nb_2O_9$ is 713 K, and a measurement at 723 K shows no diffraction peaks that cannot be assigned to the high symmetry $I4/mmm$ space group, there is only a 10 K window in which any intermediate phase could exist.

1.3.3 $CsBiNb_2O_7$

As mentioned above, the Aurivillius structure is just one of many layered perovskite structures. Another is the so-called Dion-Jacobson (DJ) phase, which has the general formula $A^+[A'_{n-1}B_nO_{3n+1}]^-$. As the formula suggests, this structure can be thought of as the Aurivillius phase with the fluorite layer replaced with a sheet of cations, typically alkali metal or hydrogen ions[29]. This also results in the loss of the "shearing" required between adjacent perovskite blocks, and so typical prototypic DJ phases have c-axis lengths close to half that of their Aurivillius phase counterparts. $CsBiNb_2O_7$ is an example of a DJ phase that is studied in this work. It was first synthesized by Subramanian et al. [30] in 1988, who used polychromatic powder x-ray diffraction to deduce an orthorhombic unit cell of volume 8 times that of the prototypic tetragonal cell, with lattice parameters $2a_T \times 2a_T \times 2c_T$. Their study also found that the alkali cations readily exchanged with protons, giving this material a relatively high proton conductivity. This property is common to the isomorphous $CsLaNb_2O_7$, the conductivity of which Gopalakrishnan et al. [31] had

demonstrated in 1987. They also concluded, however, that $CsLaNb_2O_7$ formed in the prototypic tetragonal cell, in contrast to $CsBiNb_2O_7$. In 2003, Snedden et al. [32] performed neutron diffraction on $CsBiNb_2O_7$ and concluded that the structure suggested by Subramanian et al. [30] was unnecessarily large, and instead suggest a smaller cell of $\sqrt{2}a_T \times \sqrt{2}a_T \times c_T$ in space group $P2_1am$. The point of their study was to look for potential ferroelectric behaviour so cation displacements and oxygen octahedra tilts were particularly scrutinized. Snedden et al. [32] found that there were significant displacements of both the A and B cations, however the significant displacement was in the z-direction and any polarization arising from this is cancelled by the mirror plane normal to this direction. They also observed significant tilting of the octahedra and some displacement in the polar directions, but impedance measurements showed a relatively low and temperature-independent dielectric constant and so they concluded that $CsBiNb_2O_7$ was not a ferroelectric. In 2006, Fennie and Rabe [33] performed density functional theory calculations on $CsBiNb_2O_7$ and agreed that of all the subgroups of the prototypic space group $P4/mmm$, $P2_1am$ was by far the most energetically favourable. However, from both first principles calculations (Berry phases) and empirical laws (Abrahams criteria [34]) Fennie and Rabe [33] concluded that $CsBiNb_2O_7$ was ferroelectric. This result seemed to contradict the previous observation of a temperature-independent dielectric constant, but Fennie and Rabe [33] correctly point out that this is not unheard of in ferroelectric materials far below T_c, for example $LiNbO_3$ demonstrates this behaviour. Further to this, a value of T_c of 810 K is predicted from the method of Abrahams [35].

1.3.4 $BaBi_2Nb_2O_9$

$BaBi_2Nb_2O_9$ is conspicuous among the Aurivillius phases because of its relaxor behaviour[36, 37]. Its ferroelectric behaviour was first predicted by Subbarao [38], who suggested a T_c of 473 K. Adamczyk et al. [39] showed that the phase transition in $BaBi_2Nb_2O_9$ was significantly more diffuse than the well-studied lead-containing perovskite relaxors, such as PMN, $Pb(Mg_{1/3}Nb_{2/3})O_3$; PLZT, $Pb_{0.83}La_{0.17}(Zr_{0.3}Ti_{0.7})_{0.9575}O_3$; and PBZT $(Pb_{0.75}Ba_{0.25})(Zr_{0.7}Ti_{0.3})O_3$. A mea-

sure of the diffuseness is also suggested, namely ΔT_m, which is defined as the difference in temperature between the dielectric maximum at 0.1 kHz and 20 kHz. ΔT_m would obviously equal zero for a classical ferroelectric, is 7.3 K for PBZT, and is measured as 92.6 K for $BaBi_2Nb_2O_9$. Adamczyk et al. [39] also noted the observation of Ismunandar and Kennedy [17] that there is apparent disordering of the A-site cation onto the bismuth site and *vice versa*, and that this could be the source of the relaxor behaviour in the absence of any significant structural distortion from the prototypic $I4/mmm$ space group. Previously, Ismunandar et al. [14] had asserted that $BaBi_2Nb_2O_9$ formed in the more common polar space group $A2_1am$, although large atomic displacement parameters on the bismuth site, also observed by Blake et al. [15], seemed to suggest that cation disorder was also present. These two studies used powder neutron diffraction and combined powder neutron and powder x-ray diffraction, respectively. Blake et al. [15] also observed that of the three analogous Aurivillius materials they studied, $BaBi_2Nb_2O_9$ contained the largest amount of cation mixing – something that is unexpected due to the relative size of the barium atom compared to the small size of the bismuth site. The conclusion of this flurry of publications was that if there is indeed an orthorhombic distortion, it is too small to measure, and the source of the relaxor behaviour in $BaBi_2Nb_2O_9$ is because of the disordering of the cations. In 2002, Macquart et al. [40] performed variable temperature synchrotron powder diffraction across the "phase transition". They observed discontinuities in the a and c lattice parameters, and concluded that the room-temperature space group of $BaBi_2Nb_2O_9$ was $I4mm$. This yields two independent bismuth sites, and two independent niobium sites, which they invoke to explain ferroelectricity, however they do not explain the relaxor behaviour observed by others. They also observe the relatively large atomic displacement parameters seen previously[14, 15], but only on one of the bismuth sites. However, they discerned only marginal improvements in the goodness of fits between the two different space groups.

1.4 Aim of the Present Work

The general aim of the present work is to improve our understanding of the relationship between structure and properties in complex ferroelectrics. To this end this thesis examines the less well understood stacked perovskites, such as the Aurivillius and Dion-Jacobsen phases, studying both their structures and physical properties. A secondary aim the discovery of new materials that show promising potential for industrial use as ferro- or piezoelectrics, and particularly lead free alternatives to the current industry standards such as $PbZr_{1-x}Ti_xO_3$, or PZT. Furthermore, the synthesis of new solid-solutions of known materials, as well as the synthesis of entirely new compositions, was attempted to expand our current knowledge of these families of materials. Until now, the majority of work on the stacked perovskites—and, to some extent, the perovskites—has been limited to polycrystalline samples, so to improve on this single-crystal measurements, both of structure and properties, are employed wherever possible. Optical measurements, such as birefringence, are very sensitive to distortion of structure and can detect one part in 10^7 variations in the optical anisotropy. It is the aim of this work to use this sensitivity to further our understanding of the dynamics of the structure of these materials through phase transitions. Since it also known that fluorine has a particularly low polarizability, certain materials are also fluorinated to observe the manner in which ferroelectricity varies when there is doping on the anion site, in contrast to the already large body of work concentrating on the doping of the cation sites. The chemistry of the fluorination of these materials is also of interest, since the valence of the two anions involved is different, and hence should provide a diving force for an extensive defect model. The combination of powder x-ray and single-crystal x-ray diffraction, and optical measurements mean that the role of structure can be investigated in a new and highly sensitive manner. Furthermore, this work forms part of a continuing interest in bismuth containing perovskites, because of the absence of lead in these ferroelectric materials. $Na_{0.5}Bi_{0.5}TiO_3$ (NBT) is a prime example of the Warwick group's recent work in this area [41–43].

This thesis is organized into four results chapters, with each chapter primarily

concerned with one particular experimental technique. The first two results chapters detail single-crystal measurements, with chapter 3 describing single-crystal diffraction, and chapter 4 detailing optical measurements. Chapters 5 and 6 concern polycrystalline materials, and detail powder diffraction and dielectric constant measurements respectively.

References

[1] H. D. Megaw, Proc. Phys. Soc. **58**, 133 (1946).

[2] C. A. Randall, A. S. Bhalla, T. R. Shrout, and L. E. Cross, J. Mater. Res. **5**, 829 (1990).

[3] G. O. Jones, Ph.D. thesis, University of Warwick (2001).

[4] M. T. Dove, *Structure and Dynamics, An Atomic View of Materials* (Oxford University Press, 2006).

[5] V. K. Wadhawan, *Introduction to Ferroic Materials* (Gordon and Breach, 2000).

[6] B. Aurivillius, Arki. Kemi. **1**, 463 (1949).

[7] G. A. Smolenski, V. A. Isupov, and Agranovskaya, Sov. Phys. Solid State (Translated) **3**, 665 (1962).

[8] E. C. Subbarao, J. Am. Ceram. Soc. **45**, 166 (1962).

[9] R. E. Newnham, R. W. Wolfe, and J. F. Dorrian, Materials Research Bulletin **6**, 1029 (1971).

[10] A. D. Rae, J. G. Thompson, and R. L. Withers, Acta Cryst. **B48**, 418 (1992).

[11] A. D. Rae, J. G. Thompson, R. L. Withers, and A. C. Willis, Acta Cryst. **B46**, 474 (1990).

[12] J. G. Thompson, A. D. Rae, R. L. Withers, and D. C. Craig, Acta Cryst. **B47**, 174 (1991).

[13] R. L. Withers, J. G. Thompson, and A. D. Rae, Journal of Solid State Chemistry **94**, 404 (1991).

[14] Ismunandar, B. J. Kennedy, Gunawan, and Marsongkohadi, Journal of Solid State Chemistry **126**, 135 (1996).

[15] S. M. Blake, M. J. Falconer, M. McCreedy, and P. Lightfoot, J. Mater. Chem. **7**, 1609 (1997).

[16] V. F. Sears, Neutron News **3**, 29 (1992).

[17] Ismunandar and B. J. Kennedy, J. Mater. Chem. **9**, 541 (1999).

[18] M. J. Forbess, S. Seraji, Y. Wu, C. P. Nguyen, and G. Z. Cao, Applied Physics Letters **76**, 2934 (2000).

[19] B. H. Venkataraman and K. B. R. Varma, Ferroelectrics **324**, 121 (2005).

[20] Y. Shimakawa, Y. Kubo, Y. Tauchi, T. Kamiyama, H. Asano, and F. Izumi, Applied Physics Letters **77**, 2749 (2000).

[21] S. Kamba, J. Pokorny, V. Porokhonskyy, J. Petzelt, M. P. Moret, A. Garg, Z. H. Barber, and R. Zallen, Applied Physics Letters **81**, 1056 (2002).

[22] R. Macquart, B. J. Kennedy, B. A. Hunter, C. J. Howard, and Y. Shimakawa, Integr. Ferroelectr. **44**, 101 (2002).

[23] A. K. Jha, I. Coondoo, and S. K. Agarwal, Ceram. Int. **33**, 41 (2007).

[24] Y.-F. Wei, C.-H. Kao, C.-F. Yang, H.-H. Huang, and C.-J. Huang, Mater. Lett. **61**, 4643 (2007).

[25] B. Sih, A. Jung, and Z. G. Ye, J. Appl. Phys. **92**, 3928 (2002).

[26] Y. Torii, K. Tato, A. Tsuzuki, H. J. Hwang, and S. K. Dey, J. Mater. Sci. Lett. **17**, 827 (1998).

[27] C. H. Hervoches, J. T. S. Irvine, and P. Lightfoot, Phys. Rev. B **64**, 100102 (2001).

[28] A. Snedden, C. H. Hervoches, and P. Lightfoot, Phys. Rev. B **67**, 092102 (2003).

[29] R. H. Mitchell, *Perovskites; Modern and Ancient* (Almaz Press, Ontario, 2002).

[30] M. A. Subramanian, J. Gopalakrishnan, and A. W. Sleight, Mater. Res. Bull. **23** (1988).

[31] J. Gopalakrishnan, V. Bhat, and B. Raveau, Materials Research Bulletin **22**, 413 (1987).

[32] A. Snedden, K. S. Knight, and P. Lightfoot, Journal of Solid State Chemistry **173**, 309 (2003).

[33] C. J. Fennie and K. M. Rabe, Appl. Phys. Lett. (USA) **88**, 262902 (2006).

[34] S. C. Abrahams, Acta. Cryst **B44**, 585 (1988).

[35] S. C. Abrahams, Acta Cryst. **B57**, 485 (2001).

[36] D. Nuzhnyy, S. Kamba, P. Kuzel, S. Veljko, V. Bovtun, M. Savinov, J. Petzelt, H. Amorin, M. E. V. Costa, A. L. Kholkin, et al., Phys. Rev., B, Condens, Matter Mater. Phys. **74**, 134105 (2006).

[37] P. Keburis, J. Banys, A. Brilingas, J. Prapuolenis, A. Kholkin, and M. E. V. Costa, J. Nanosci. Nanotechnol. **353**, 149 (2007).

[38] E. C. Subbarao, J. Phys. Chem. Solids **23**, 665 (1962).

[39] M. Adamczyk, Z. Ujma, and M. Pawelczyk, J. Mater. Sci. **41**, 5317 (2006).

[40] R. Macquart, B. J. Kennedy, T. Vogt, and C. J. Howard, Phys. Rev, B, Condens, Matter Mater. Phys. (USA) **66**, 212102 (2002).

[41] S. Trujillo, J. Kreisel, Q. Jiang, J. H. Smith, P. A. Thomas, P. Bouvier, and F. Weiss, J. Phys., Condens. Matter. **17**, 6587 (2005).

[42] G. O. Jones and P. A. Thomas, Acta Cryst. **B58**, 168 (2002).

[43] G. O. Jones, J. Kreisel, V. Jennings, M. A. Geday, P. A. Thomas, and A. M. Glazer, Ferroelectrics **270**, 191 (2002).

Chapter 2

Experimental Background & Theory

2.1 Powder Diffraction & Rietveld Refinement

The theory of diffraction is well-known amongst solid-state scientists and is not repeated here. For a thorough background to the subject, examples of good texts are Giacovazzo [1] and Hammond [2]. What is included here is the theory of some of the more advanced areas of diffraction, including the various structural refinement methods utilised.

2.1.1 The Rietveld Method

Powder diffraction is a versatile tool for the study of structure in a large range of materials. The simple diffraction geometry means that experiments can be easily performed and makes refinement a relatively simple process. The ease with which the temperature of the sample can be controlled means that the study of phase transitions and non-ambient behaviour is also considerably easier than for single-crystal samples. Powder diffraction also has the advantage that samples are often synthesised with relative ease compared to single crystals. In materials that contain heavy elements (such as those in the current study) powder diffraction also benefits from a low sensitivity to absorption, which can be problematic in single crystals. Given a close starting model, the refinement of powder data is also straightforward.

The Rietveld method [3, 4] is a mathematical algorithm for total pattern fitting that computes a model pattern from a simple set of crystallographic and profile parameters. The algorithm computes the peak positions from the lattice parame-

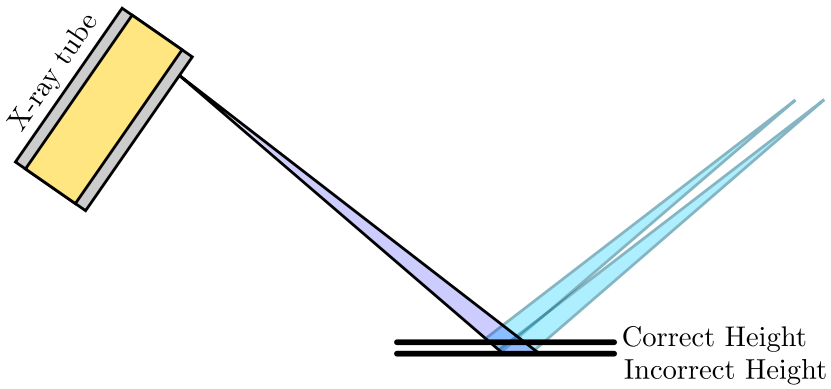

Figure 2-1: Schematic demonstrating the affect of sample height error on diffraction data collected in Bragg-Brentano geometry. The incorrect height also leads to a change in the beam path length and hence the focussing optics of the experiment. This leads to a combination of incorrect peak position, and intensity. This effect can, however, be modelled and accounted for.

ters and the peak intensities from the atomic coordinates, and this forms the basis of the model pattern. Also applied are a polynomial to describe the background function, atomic displacement parameters (ADPs), to describe the thermal motion of the atoms, and a phenomenological 2θ-dependent peak-shape function, which is applied to the peaks along with an emission profile describing the radiation. When other effects are also observed in the diffraction data, these can also be applied to the model; such effects include detector zero error, absorption, preferred orientation, and axial divergence of the beam, among others.

Diffraction data collected in Bragg-Brentano geometry is also sensitive to error in the sample-height. A schematic demonstrating this affect can be seen in figure 2-1. As well as changing the angle of diffraction—and hence yielding incorrect peak positions—height error changes the total path length of the beam and hence the focal position of the diffraction optics. This also yields a systematic reduction in peak intensity; however this, and the peak position error, can be modelled via simple geometric analysis, and this is implemented in most Rietveld packages.

In the Rietveld refinement process, the experimental powder pattern is broken into i increments, each of observed intensity y_i. When data are collected from a constant wavelength source, these increments are in diffraction angle 2θ. In the

first cycle of the refinement, the calculated and observed patterns are compared increment-wise, and a residual function is calculated[5]:

$$S_y = \sum_i w_i \left| y_i - y_{i(c)} \right|^2 \tag{2-1}$$

where $w_i = 1/y_i$ is the weighting factor of the ith observation, y_i is the observed intensity and $y_{i(c)}$ is the intensity calculated from the model. $y_{i(c)}$ is computed as the sum of a background term and contributions from local (in 2θ) Bragg reflections, modified by several scaling factors:

$$y_{i(c)} = s \sum_{\mathbf{h}} L_{\mathbf{h}} \left| F_{\mathbf{h}} \right|^2 \phi(2\theta_i - 2\theta_{\mathbf{h}}) A + y_{b,i} \tag{2-2}$$

where s is the whole pattern scale factor, $\mathbf{h}$ is the Miller indices for a Bragg reflection, $L_{\mathbf{h}}$ contains the Lorentz polarization and multiplicity factors, $\phi(2\theta_i - 2\theta_{\mathbf{h}})$ is the reflection profile function (detailed below), A is an absorption factor, $F_{\mathbf{h}}$ is the structure factor of the $\mathbf{h}$th reflection, and $y_{b,i}$ is the background contribution. The objective of the Rietveld method is to minimize the residual quantity, S_y, by refining the various model parameters. This process leads to a set of normal equations relating derivatives of all the calculated intensities $y_{i(c)}$ with respect to each adjustable parameter. These equations are solved by inversion of the normal matrix, defined as:

$$\mathbf{M}_{jk} = -\sum_i 2w_i \left[(y_i - y_{i(c)}) \frac{\partial^2 y_{i(c)}}{\partial x_j \partial x_k} - \left(\frac{\partial y_{i(c)}}{\partial x_j} \right) \left(\frac{\partial y_{i(c)}}{\partial x_k} \right) \right] \tag{2-3}$$

where $x_{j,k}$ are the set of m refining parameters, leading to the normal matrix being of dimensions $m \times m$. The change in any given parameter x_k is then defined as:

$$\Delta x_k = \sum M_{jk}^{-1} \frac{\partial S_y}{\partial x_k}. \tag{2-4}$$

These parameter shifts are then applied to the initial model, and the normal matrix is formed once more, and the process is repeated until $\frac{\partial S_y}{\partial x_k} \to 0$, meaning that S_y is minimized. This basic architecture is the algorithm as implemented in all Rietveld software, but the exact methods for performing these tasks are unique to each program package. In the current study, Topas Academic is the Rietveld package of choice, details of which can be found elsewhere[6].

Table 2-1: Reflection profile functions and peak shapes for powder diffraction. Γ is the full-width-at-half-maximum, η is the mixing parameter where Gaussian and Lorentzian elements are combined, C_n are various constants, and U, V, W, X, Y, Z are other refinable parameters.

Name	Function
Gaussian Profile Function	$\Gamma^2 = U\tan^2\theta + V\tan\theta + W$
Pseudo-Voigt Peak Shape	$\eta L + (1-\eta)G$
TCHZ Peak Shape	$\eta = C_1(\Gamma_L/\Gamma) - C_2(\Gamma_L/\Gamma)^2 + C_3(\Gamma_L/\Gamma)^3$
TCHZ Gaussian Profile Function	$\Gamma_G = (U\tan^2\theta + V\tan\theta + W + Z/\cos^2\theta)^{0.5}$
TCHZ Lorentzian Profile Function	$\Gamma_L = X\tan\theta + Y/\cos\theta$

The Reflection Profile Function

The reflection profile function describes the peak shape as a function of diffraction angle, and is sensitive to contributions from effects originating from both the instrument and the sample. These both yield different peak shapes, and have different dependence on diffraction angle, and so a function is needed to describe the reflection profile. For early work in the field of powder diffraction, when instruments were of low resolution by today's standards, the peak shape was dominated by instrumental effects and as such a purely Gaussian function was used, with an angular dependence of the full-width-at-half-maximum, Γ as suggested by Caglioti et al. [7] (table 2-1). As instrument resolution improved, however, sample effects such as strain and crystallite size became more apparent over the reduced instrument contribution, and so a new model was required. These sample effects are best described by a Lorentzian peak, and so a correct reflection profile function needs to describe a convolution of a Gaussian and a Lorentzian peak shape, with each of the independent peak widths $\Gamma_{G,L}$ having a different angular dependence. Since a pseudo-Voigt is a mixture of a Gaussian and a Lorentzian with a mixing parameter η, this forms the basis of one such reflection profile: the modified Thompson-Cox-Hastings pseudo-Voigt, or TCHZ reflection profile. This profile contains a mixing parameter, η that is dependent on the relative widths.

Table 2-2: Regularly used numerical criteria of fit in Rietveld refinement. $I_{h(o)}$ is an intensity ascribed to the **h**th peak based on the proportion of $I_{\mathbf{h}(c)}$ to the total peak area, when more than one Bragg reflection makes up a peak in the powder pattern. It should be more accurately referred to as $I_{\mathbf{h}(\text{“}o\text{”})}$. i and m are the number of increments in the data and the number of refinement parameters, respectively.

Name	Function
R-Profile factor	$R_p = \dfrac{\sum_i \lvert y_i - y_{i(c)} \rvert}{\sum_i y_i}$
Weighted R-Profile factor	$wR_p = \left[\dfrac{\sum_i w_i \lvert y_i - y_{i(c)} \rvert^2}{\sum_i w_i y_i^2} \right]^{\frac{1}{2}}$
R-Structure factor	$R_F = \dfrac{\sum_{\mathbf{h}} \lvert I_{\mathbf{h}(o)}^{1/2} - I_{\mathbf{h}(c)}^{1/2} \rvert}{\sum_{\mathbf{h}} I_{\mathbf{h}(o)}^{1/2}}$
R-Bragg factor	$R_{\text{Bragg}} = \dfrac{\sum_{\mathbf{h}} \lvert I_{\mathbf{h}(o)} - I_{\mathbf{h}(c)} \rvert}{\sum_{\mathbf{h}} I_{\mathbf{h}(o)}}$
Goodness of fit	$\chi^2 = \dfrac{S_y}{i - m}$
R-expected	$R_e = \left[\dfrac{i - m}{\sum_i w_i y_{i(o)}^2} \right]^{\frac{1}{2}}$

As well as the residual S_y, which is minimized by the algorithm, several other statistical measures of the quality of the fit to the observed data are regularly calculated, for inspection by the user. These measures help to identify if the refinement has found a false minimum, or an incorrect model, a summary of which are shown in table 2-2. R-expected is a statistical measure of the quality of the data, based on the maximum theoretical data held within the pattern, and the number of refinement parameters that are being refined from the data. It should be noted that $\chi^2 = wR_p/R_e$, and hence χ^2 should never fall below 1, as this means the more information has been extracted than is present in the data.

2.2 Single-Crystal Diffraction and Refinement

2.2.1 Data Collection and Integration

The single-crystal x-ray diffraction performed in this study involves the collection of the whole, or a sufficient proportion, of the Ewald sphere using a large, CCD based detector. A four circle, kappa-geometry goniometer moves the crystal, which is mounted on a glass fibre, to a particular orientation and the crystal is illuminated with x-rays. The detector collects a "frame", after which the goniometer moves to another orientation, to record the next frame. Typically, the data will be collected in runs of one varying angle with the other three being held constant, with the varying angle incrementing by some predefined step size. Generally speaking, the larger the unit cell, the smaller the required step size. In this study, all of the parameters that make up a run list are optimised for the individual crystal by performing a pre-experiment.

During data integration from the raw frames into a list of collected reflections, one has the option of performing outlier rejection by selecting a particular Laue group under which to perform the integration. This allows the software to discard any reflections which break the Laue symmetry. One may also select a cell centering and apply a Bravais lattice extinction to remove those reflections that should be systematically absent due to the centering. A measure of the quality of the integration is the internal R-factor:

$$R_{\text{int}} = \frac{\sum_{\mathbf{h}} \left| F^2_{\mathbf{h}(o)} - \left\langle F^2_{\mathbf{h}(o)} \right\rangle \right|}{\sum_{\mathbf{h}} F^2_{\mathbf{h}(o)}} \tag{2-5}$$

this relates the intensities of multiple instances of a single peak $\left(F^2_{\mathbf{h}(o)}\right)$ compared to the average intensity, $\left\langle F^2_{\mathbf{h}(o)} \right\rangle$. If the data are of good quality, every instance of a peak should have $F^2_{\mathbf{h}(o)} = \left\langle F^2_{\mathbf{h}(o)} \right\rangle$ and hence R_{int} would then be equal to 0 for perfect data. This measure of quality can be applied at many stages throughout the data collection, solution, and refinement. Two other measures used to describe a single-crystal data collection in this study are the completeness, and the redundancy. The completeness is the percentage of the Ewald sphere collected to a defined resolution. A hemisphere collection to 0.7 Å would therefore be described as having

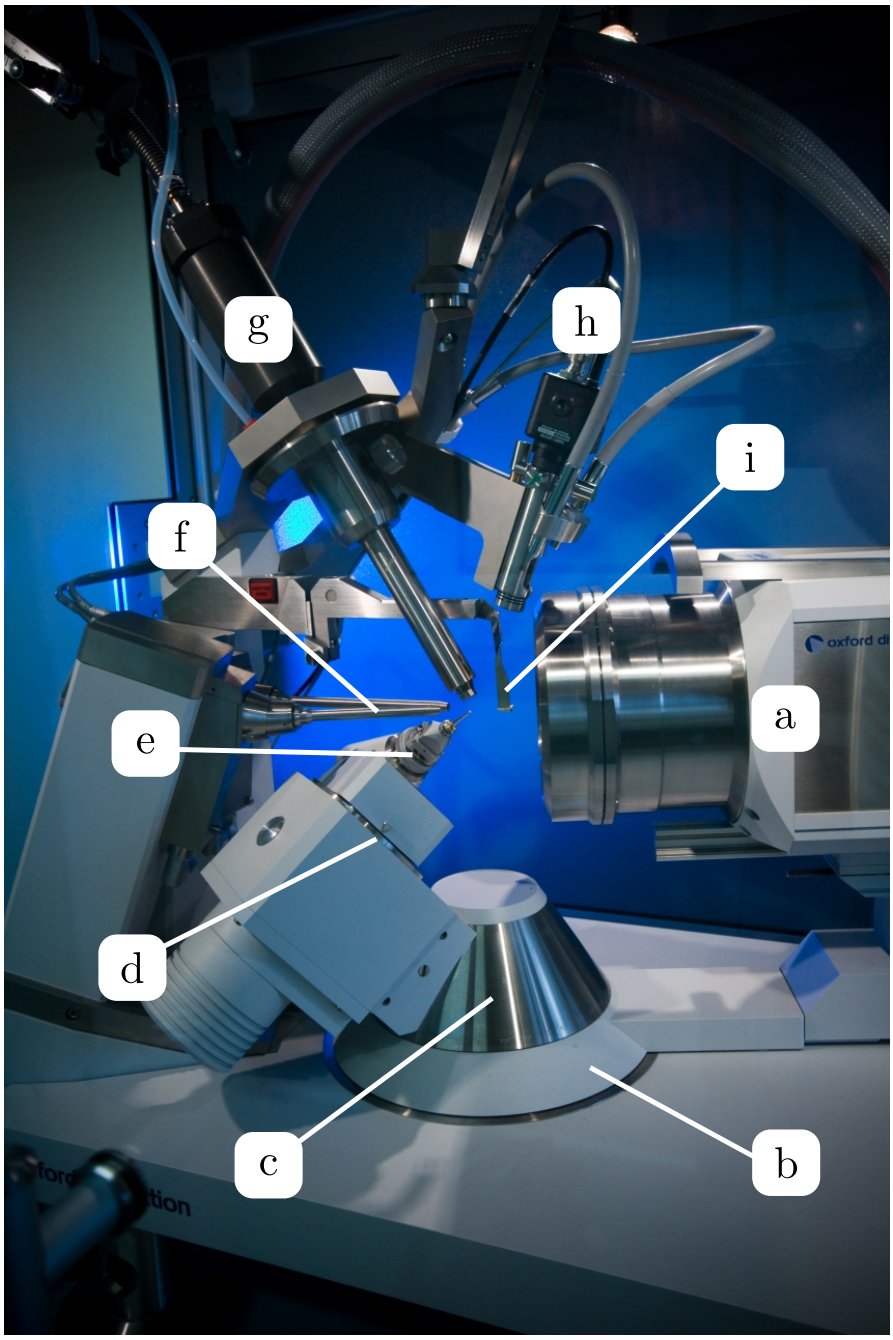

Figure 2-2: Annotated diagram of the Oxford Diffraction CCD diffractometer used in this study. Highlighted are the CCD detector (a); the θ circle on which the detector is mounted (b); the ω circle (c); the κ circle (d); the ϕ circle and goniometer head (e); the incident beam collimator (f); the cryo-jet for low temperature experiments (g); the video microscope and sample illumination for crystal alignment (h); and the beam stop (i). *Photograph courtesy of Nathan Barrow*

50% completeness to 0.7 Å. The redundancy of a collection is the mean number of times each individual peak is collected. Obviously, the higher the redundancy, the more accurate the data collection and subsequent refinement will be.

2.2.2 Absorption Correction

Considering that the intensity of a diffracted maximum from a crystal is proportional to the volume of the crystal, one may think that the larger the crystal the better. This would be true, if it were not for absorption, which is described by the equation applicable to many absorption processes:

$$\frac{I}{I_0} = \exp^{-\mu x} \tag{2-6}$$

where x is the total path length ($x = x_i + x_d$) and μ is the linear absorption coefficient. The absorption of the incident and diffracted beams mean that there exists an optimum crystal size, that depends on the absorption of the material and the wavelength. If one assumes that $I_0 \propto x^3$, and hence that $I \propto x^3 \exp^{-\mu x}$, then one can calculate an estimate of this optimum size by differentiating this:

$$\frac{\mathrm{d}I}{\mathrm{d}x} = 3x^2 \exp^{-\mu x} - x^3 \mu \exp -\mu x \tag{2-7}$$

$$= x^2 \exp^{-\mu x} (3 - \mu x), \tag{2-8}$$

and the maxima of $I(x)$ occurs when $\mathrm{d}I/\mathrm{d}x = 0$, or when $x = 3/\mu$. For a typical absorption coefficient in this study of $\mu \simeq 40\,\mathrm{mm}^{-1}$, this gives an ideal dimension of $x = 75\,\mu\mathrm{m}$. Even when crystals of this dimension are used for diffraction, if the crystal shape is not spherical then certain reflections will be recorded with a longer total path length than others, leading to a systematic reduction in intensity for some peaks. This is accounted for by calculating the transmission factor,

$$T = \frac{1}{V} \int_V \mathrm{d}\tau \exp\left[-\mu L(\mathbf{r})\right], \tag{2-9}$$

where $L(\mathbf{r})$ is the total path length for a ray that is diffracted at $\mathbf{r}$. Three main methods of calculating the transmission factor, and hence correcting the intensities for absorption are as follows.

Empirical Method - An empirical method uses the measured intensities to infer the crystal shape, using knowledge of the symmetry of the goniometer, and Friedel

pairs, to correct the intensities. This method is used rarely in this study, since most of the structures are non-centrosymmetric, and suffer from large absorption.

Gaussian Grid - The Gaussian grid method of Busing and Levy [8] uses a model of the crystal shape input by the user, and integrates over a grid of points using the method of Gauss. The improvement of this method over recent years is the increase in the number of grid points that can be integrated over because of increased computer power, yet it still yields incorrect intensities when dealing with crystals with large μ.

Analytical Method - The analytical method of Clark and Reid [9] is an exact solution which splits the input crystal shape into so-called Howells polyhedra, in such a way that in any given polyhedron, only one face is illuminated and the beam is either absorbed or diffracted out of another face. Historically, this method suffered from lengthy computational time required to locate the vertices of the Howells polyhedra: Clark [10], however, devised an efficient algorithm to achieve this.

2.2.3 Structure Solution

Several methods exist for the solution of structure from single-crystal diffraction data, with the aim of solving the phase problem. The two methods used in this study are outlined here.

The Patterson Function - In his seminal paper Patterson pointed out the crystallographic significance of performing a Fourier transform on the phaseless $|F|^2$. He successfully demonstrated that whilst performing Fourier analysis on the raw F's gave the distribution of atoms in the cell, performing it on $|F|^2$ yielded peaks representing the interatomic vectors. A peak in the resultant Patterson map at $\mathbf{p} = (u, v, w)$, therefore, corresponds to a pair of atoms at $\mathbf{r}_1 = (x_1, y_1, z_1)$ and $\mathbf{r}_2 = (x_2, y_2, z_2)$, such that $\mathbf{p} = \mathbf{r}_1 - \mathbf{r}_2$. In the Patterson map, the weight of a peak can be shown to be proportional to the square of the sum of the atomic numbers of the two atoms it describes, and hence vectors between heavy atoms are most clearly seen. For this reason, Patterson solving is most generally used to locate the heavy atoms in a structure.

The Representation Approach - The Patterson function showed that the phases

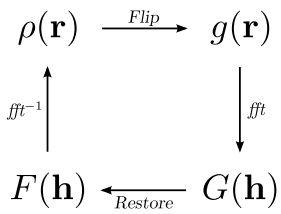

Figure 2-3: Schematic of the charge flipping algorithm, which uses Fourier recycling to determine the phases of the structure factors.

ϕ could be retrieved from the Fourier transform of the intensities, and so it was argued that the data should be retrievable from the intensities directly. Many techniques were developed to attempt this, and that discussed here is the representation approach [11] as implemented in *SIR-92*. The representation theory uses structure invariants and semi-invariants, such as $F_{-h}F_kF_{h-k}$ which has phase $\phi_{-h}+\phi_k+\phi_{h-k}$, known as a triplet invariant. Known sets of reflections are compared to retrieve the phases.

Charge Flipping - The charge flipping (CF) technique, as introduced in 2004 by Oszlányi and Sütő [12], is an *ab initio* method for structure solution from diffraction data. It utilises Fourier recycling to elucidate the real-space electron density. The basic charge flipping scheme is seen in figure 2-3. The central assumptions of CF are those of many of the direct methods[13]: namely that the electron density function exhibits Positivity and Atomicity. Positivity refers to the assumption that the charge density is positive everywhere ($\rho(\mathbf{r}) \geq 0$). Atomicity refers to the assumption that the majority of the charge exists in a small number of discrete areas, namely the atomic positions, or rather more importantly for CF, that most of space is *not* atoms.

The iteration begins with the observed structure factor amplitudes, $F_{obs}(\mathbf{h})$, combined with random phases consistent with Friedel's Law, $\phi(-h) = -\phi(h)$, inverse Fourier transformed into an electron density, $\rho(\mathbf{r})$. Any voxel of $\rho(\mathbf{r})$ with a density above a pre-defined limit δ is left unchanged, whilst every other voxel has its charge density inversed.

$$\rho(\mathbf{r}) = \begin{cases} g(\mathbf{r}) & \text{if } g(\mathbf{r}) \geq \delta, \\ -g(\mathbf{r}) & \text{if } g(\mathbf{r}) < \delta. \end{cases} \tag{2-10}$$

This new, "flipped" density, $g(\mathbf{r})$, from which the method gains it's name, is Fourier transformed into a new set of structure factors, $G(\mathbf{h})$. The phases of the $G(\mathbf{h})$ are recombined with the amplitudes of the observed structure factors $F_{obs}(\mathbf{h})$ to yield a new $F(\mathbf{h})$. These structure factors are inverse Fourier transformed, to form the next iteration of $\rho(\mathbf{r})$. The process converges to a limit cycle and continues indefinitely, until it is interrupted by the user, or a particular criterion reaches a user defined target.

2.2.4 Structure Refinement

The refinement of a structure from single-crystal data using the least-squares method follows a very similar routine to that used in Rietveld refinement (and, indeed, all least-squares algorithms). In single-crystal data, the full matrix of structure factors is refined, as opposed to the intensity of an increment of the powder pattern, as in the Rietveld method, and hence the unit-weighted residual to be minimized is

$$R_s = \sum_{\mathbf{h}} \left[F_{\mathbf{h}(o)} - F_{\mathbf{h}(c)} \right]^2, \tag{2-11}$$

where $F_{\mathbf{h}(c)}$ is the calculated structure factor for the peak with indices $\mathbf{h}$. Other indications of the quality of the fit can be seen in table 2-3. These include R_{obs}, the R value of data that is "observed" - that is to say that the intensity of the peak is higher than three times the standard deviation, $I > 3\sigma$.

2.2.4.1 Electron Density Maps

The origin of any individual x-ray diffraction datum is the 3-dimensional electron density of the sample. What is measured, however, is a representation of the reciprocal lattice, rather than the real lattice. Utilized in the process of charge flipping is the principle of the Fourier transform, which transforms data between real and reciprocal space. This method is used to calculate a visual representation of a model structure, by revealing the electron density which would lead to the model diffraction data. Since the model diffraction data are refined to equal the observed data, it stands to reason that the Fourier transform of the calculated data is a good representation of the observed electron density. Whilst it is not productive to calculate the electron density resulting from the calculated structure

Table 2-3: Various regularly used numerical criteria of fit in single-crystal refinement.

Name	Function
R-factor (All)	$R_{\text{obs}} = \dfrac{\sum_{\mathbf{h}} \left\| \lvert F_{\mathbf{h}(o)} \rvert - \lvert F_{\mathbf{h}(c)} \rvert \right\|}{\sum_{\mathbf{h}} \lvert F_{\mathbf{h}(o)} \rvert}$
R-factor (observed)	$R_{\text{obs}} = \dfrac{\sum_{\mathbf{h}(I>3\sigma)} \left\| \lvert F_{\mathbf{h}(o)} \rvert - \lvert F_{\mathbf{h}(c)} \rvert \right\|}{\sum_{\mathbf{h}(I>3\sigma)} \lvert F_{\mathbf{h}(o)} \rvert}$
Goodness of fit	$S = \left[\dfrac{\sum_{\mathbf{h}} w_{\mathbf{h}} \left(F^2_{\mathbf{h}(o)} - F^2_{\mathbf{h}(c)} \right)^2}{N_{\text{R}} - N_{\text{P}}} \right]^{\frac{1}{2}}$

factors combined with the calculated phases, Fourier analysis does play a role in verifying the model when elements of the calculated and observed data are combined.

Combining the calculated phases with the observed structure factors can reveal areas of real space that do not contain sufficient electron density, and hence indicate the location of atoms missing from the model. Perhaps the most powerful use of Fourier analysis is the combination of observed and calculated intensities, and the calculated phases. The resulting Fourier map, known as a Fourier difference map, contains peaks indicating insufficient density similar to the map resulting from the observed structure factors. Also present in a difference map, however, are troughs indicating areas of excessive density in the model.

Provided the model is close to correct, the use of the calculated phases means that the Fourier maps are accurate. However, if the model is grossly incorrect then the calculated phases will be similarly inaccurate, and the Fourier map will not be valid.

2.3 Birefringence

2.3.1 Optical Theory

The speed with which light passes through an optically transparent medium is related to the speed of light in a vacuum c by the refractive index of the material $n = \frac{c}{v}$. In an optically anisotropic material, two waves travelling in the same direction, with orthogonal polarizations, do not necessarily move at the same speed. When this is the case, one can assign each polarization its own refractive index (n_1 & n_2), and hence define a measure of the optical anisotropy called the linear birefringence:

$$\Delta n = n_1 - n_2 \tag{2-12}$$

The linear birefringence (or simply, birefringence) is inherent to the material and will manifest itself as a phase difference in the two polarizations, since they are travelling at different speeds. The retardation of the sample is thickness dependent, and is defined as $\Gamma = \Delta n L$, where L is the sample thickness. This can then be used to calculate the phase difference as:

$$\delta = \frac{2\pi}{\lambda}\Gamma = \frac{2\pi}{\lambda}\Delta n L, \tag{2-13}$$

where λ is the wavelength of the light. Inspection of the variation of refractive index with polarization direction for a wave of constant direction shows that it is described by an ellipse. For an optically isotropic direction—which may be any direction in an optically isotropic material, or a special optically isotropic direction (a so–called optic axis) in an anisotropic material—the radii of this ellipse will be equal, and the refractive index is described by a circle. An example of such an ellipse is shown in figure 2-4. In such an ellipse, the longer axis is known as the slow axis and the shorter axis as the fast axis. Of course, the refractive indices of a 3-dimensional crystal are described by a 3-dimensional surface which takes the form of a ellipsoid. The relationship between the ellipse as seen in figure 2-4 and the ellipsoid, called the indicatrix, is seen in figure 2-5. For certain materials, particularly those forming in tetragonal symmetry, a special case exists where the material is optically isotropic down one unique axis and anisotropic in all other directions. In a tetragonal crystal the unique axis, or the *optic axis*, is collinear

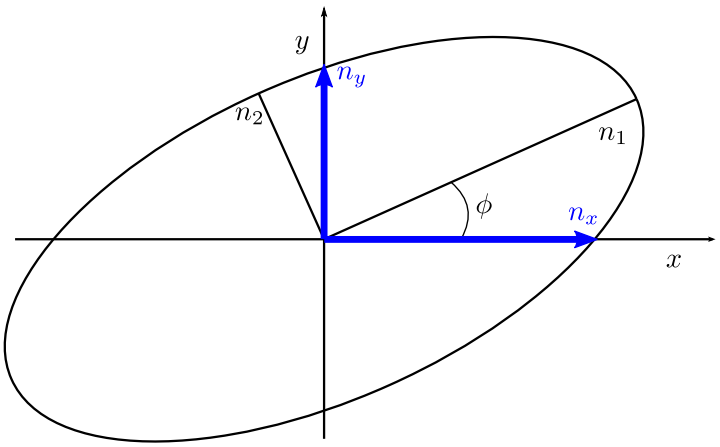

Figure 2-4: A 2D indicatrix for a material demonstrating optical anisotropy. For light polarized along the axes, where the angle between these axes and the optical axes is ϕ, the measured refractive indices are n_x and n_y.

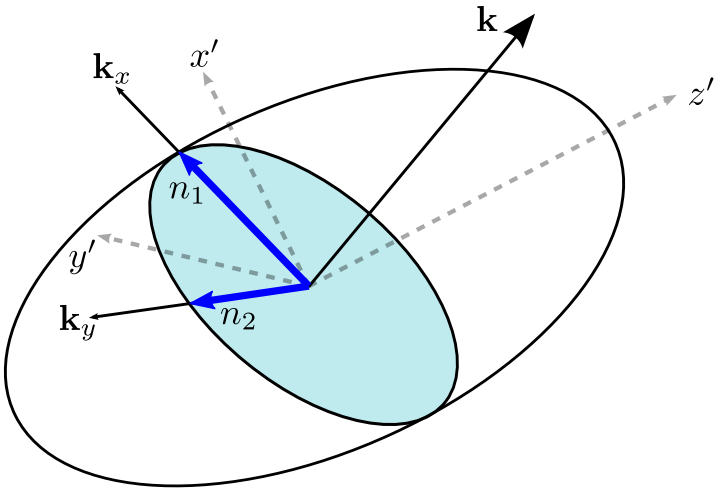

Figure 2-5: The 3D indicatrix for a material demonstrating optical anisotropy. Light with direction $\mathbf{k}$, and orthogonal polarizations $\mathbf{k}_x$ and $\mathbf{k}_y$, is incident on a material with indicatrix principle axes of (x', y', z'). The light blue ellipse is formed where the plane defined by $\mathbf{k}_x$ and $\mathbf{k}_y$ bisects the indicatrix, and the axes of this ellipse are the refractive indices.

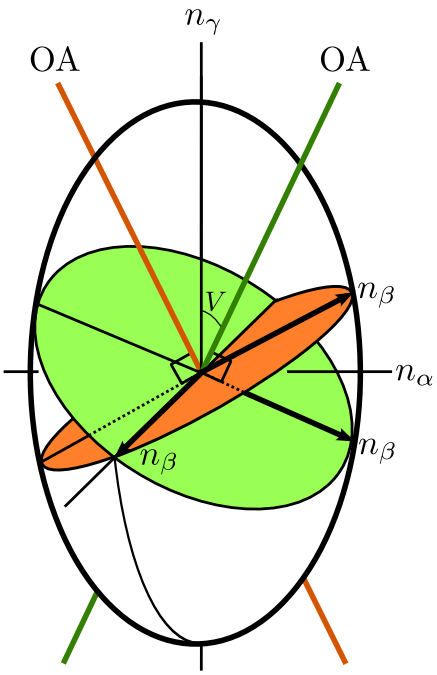

Figure 2-6: The optic axes in a biaxial material

with the 4-fold axis. In this case, the indicatrix is an ellipse with two axes of equal length, *i.e.*, it has a circular cross section perpendicular the optic axis. Such a crystal is described as being *uniaxial*. The most common form of indicatrix is that where the three axes are not of equal length. In this case, the three refractive indices are denoted $n_\alpha < n_\beta < n_\gamma$. These crystals are known as biaxial because of the existence of two unique "optic axes" down which the cross section of the indicatrix is a circle. This means that along these two axes, the material appears isotropic and as such has $\Delta n = 0$. The axes exist perpendicular to n_β, at an angle V from n_γ. In materials that are biaxial there are three values of birefringence, each one found by looking down one of the three axes of the indicatrix: $\Delta n_{\gamma\beta} = n_\gamma - n_\beta$, $\Delta n_{\beta\alpha} = n_\beta - n_\alpha$ and $\Delta n_{\gamma\alpha} = n_\gamma - n_\alpha$.

2.3.2 The Rotating Polarizer (Analyser) Method

An automated technique for the measurement of the birefringence and the orientation of the optical indicatrix was devised by Wood and Glazer [14]. Previously, a system known as polarizer-specimen-analyser was used, which essentially comprised of crossed polarizers. This technique meant that the sample had to be

Table 2-4: Shape and orientation of the optical indicatrices for the seven crystal systems

Crystal System	Indicatrix shape	Orientation
Cubic	Sphere	
Tetragonal	Uniaxial	OA along unique 4-fold axis
Trigonal	Uniaxial	OA along unique 3-fold axis
Hexagonal	Uniaxial	OA along unique 6-fold axis
Orthorhombic	Biaxial	Axes α, β, γ along 2-fold axes
Monoclinic	Biaxial	One of α, β, γ along 2-fold axis, others not fixed
Triclinic	Biaxial	No fixed Orientation

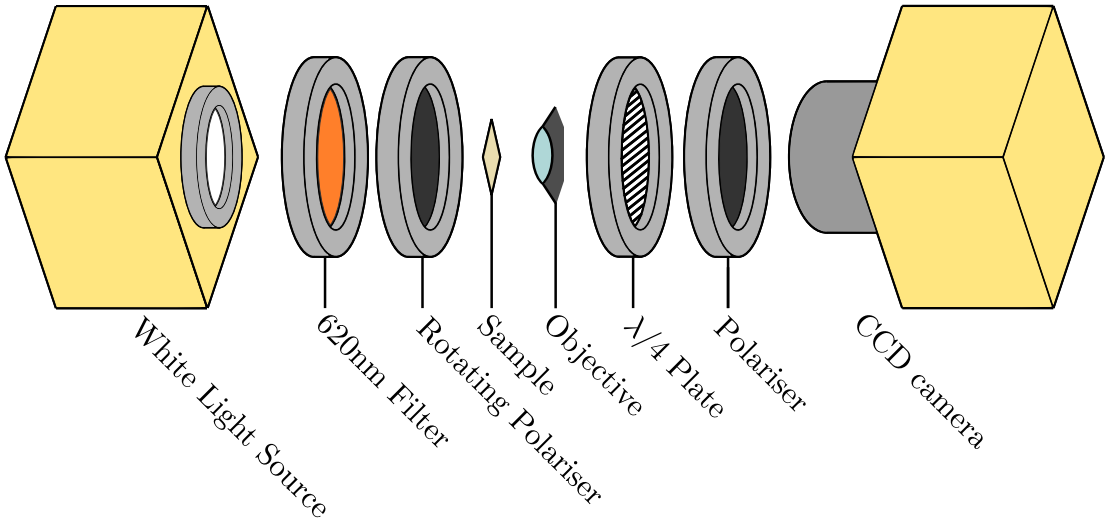

Figure 2-7: The basic experimental set-up of the rotating polarizer method. Monochromatic light is passed through a rotating polarizer before the sample. Then, the light passes through a circular analyser, comprising a quarter wave plate and a polarizer, before being detected by the camera.

orientated with respect to the apparatus which made the experiment difficult. In the rotating polarizer method, monochromatic light is passed through a rotating polarizer, then onto the sample, and through a circular analyser. This technique allows the sample to remain stationary, and can separate the effects of orientation and retardation. The basic experimental set-up is shown in figure 2-7. It was shown by Wood and Glazer [14] that, for a point detector, the measured intensity is given by

$$I = \frac{1}{2} I_0 \left[1 + \sin 2(\omega\tau - \phi) \sin \delta\right], \tag{2-14}$$

where ω is the angular frequency of the rotating polarizer, and τ is time, meaning that $\omega\tau$ is the angular position of the polarizer. It can be clearly seen from equation 2-14 that for a single point detector, a sinusoidal analogue signal will be observed as a function of polarizer angle, $\omega\tau$. This signal will have amplitude proportional to $\sin\delta$, and frequency and phase equal to 2ω and 2ϕ respectively. Mathematical analysis then reveals I_0, the *transmittance* of the sample, ϕ, the orientation of the indicatrix, usually measured anticlockwise from the slow direction, with $\phi = 0$ being horizontal, and $|\sin\delta|$, a measure of the magnitude of the birefringence. A natural progression of this technique was to replace the point photomultiplier with a CCD camera, which is effectively 640×480 point detectors allowing for a large area of crystal to be probed simultaneously, and for each pixel the above three quantities can be found, and plotted in the form of false colour images.

If one then places the sample in a cryofurnace, or pressure cell, or other environmental stage, then one can plot the above three quantities as a function of some environmental variable. In the current study, phase transitions that occur at high temperature are of interest, so a furnace is used, and these quantities can be assessed across a phase transition. If the change in the retardation is sufficient, and δ changes by more than π, then multiple $|\sin\delta|$ waveforms will be observed. When this is the case attributing a value of δ becomes trivial, since it must equal $\pi/2$ for the first peak, and $(2n-1)\pi/2$ for the nth peak. The same principle can be applied to the points of $|\sin\delta| = 0$. This is summarized for a continuous ferroelectric-paralectric phase transition that occurs at critical temperature T_C, in figure 2-8. Above T_C the sample demonstrates zero birefringence.

2.4 Dielectric Spectroscopy

An essential feature of materials that exhibit ferroelectricity is an electrical "softening" close to the critical temperature, T_c. This is often seen as a peak in the dielectric constant, which is a result of the susceptibility being maximized close to the phase transition. Measuring the capacitance and the conductance of the sample (assuming a simple equivalent circuit) means that the real and the imaginary

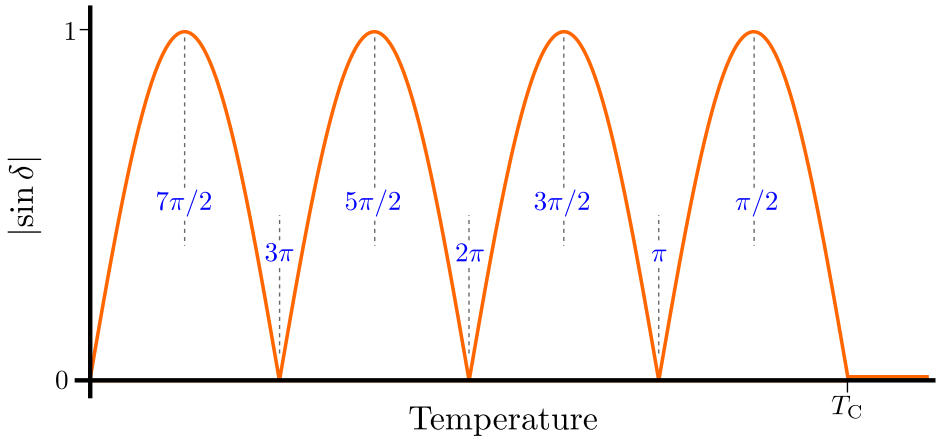

Figure 2-8: Demonstration of the calculation of δ from a plot of $|\sin\delta|$. A material is cooled from an optically isotropic, high temperature ($T > T_c$) phase to a low temperature phase with $\Delta n \neq 0$. Deduced values of δ are shown in blue.

parts of the dielectric constant can be calculated *via* the following relationships:

$$\epsilon' = \frac{Cd}{\epsilon_0 D} \tag{2-15}$$

$$\epsilon'' = \frac{Gd}{\omega\epsilon_0 D} \tag{2-16}$$

where D is the electrode area, d is the sample thickness, and C and G are the measured capacitance and conductance respectively.

References

[1] C. Giacovazzo, *Fundamentals of Crystallography* (Oxford University Press, 2002).

[2] C. Hammond, *The Basics of Crystallography and Diffraction* (Oxford University Press, 1997).

[3] H. M. Rietveld, Acta. Cryst. **20**, 508 (1967).

[4] H. M. Rietveld, J. Appl. Cryst **2**, 65 (1969).

[5] R. Young, *The Rietveld Method* (Oxford University Press, 2002).

[6] A. A. Coelho, J. Appl. Cryst. **38**, 455 (2005).

[7] G. Caglioti, A. Paoletti, and F. P. Ricci, Nucl. Instrum. Methods **35**, 223 (1958).

[8] W. H. Busing and A. Levy, Acta. Cryst. **38**, 455 (2005).

[9] R. C. Clark and J. S. Reid, Acta Cryst. **A51**, 887 (1995).

[10] R. C. Clark, Acta. Cryst. **A49**, 692 (1993).

[11] C. Giacovazzo, Acta Cryst. **A33**, 933 (1977).

[12] G. Oszlányi and A. Sütő, Acta Cryst. **A60**, 134 (2004).

[13] A. A. Coelho, Acta Cryst. **A63**, 400 (2007).

[14] I. G. Wood and A. M. Glazer, J. Appl. Cryst. **13**, 217 (1980).

Chapter 3

Single-Crystal Structural Studies

Preface

Where single crystals of suitable size and quality are obtainable single-crystal diffraction offers the possibility of high-accuracy structure solution. The technique complements powder work very well; where twinning, modulation and diffuse scattering can hinder a single-crystal solution, powder data can yield a very good starting approximation for a general sub-structure. A powerful diffraction facility will preferably incorporate both techniques and use them in tandem.

3.1 Single-Crystal Sample Preparation

Single crystals were grown from the ceramic powders using the bulk flux method. The powder was mixed with a suitable flux and placed in a sealed platinum crucible in a three-zone vertical tube furnace, encased in a bismuth-rich pyrophilite surround. After a long dwell to dissolve and homogenize the constituents, a slow accelerating cooling profile enabled nucleation and growth to proceed slowly enough to ensure the formation of large crystals suitable for optical measurements and single-crystal x-ray diffraction. The crystals were liberated from excess flux by soaking in warm dilute hydrochloric acid for several hours. A typical thermal profile for crystal growth using this method is shown in figure 3-1

$\mathbf{SrBi_2Nb_2O_9}$

The growth of $SrBi_2Nb_2O_9$ was based on the method of Amorin et al. [1]. The prepared $SrBi_2Nb_2O_9$ ceramic was mixed with a boron oxide and bismuth oxide flux in the molar ratio of 4:1:1. The furnace was then ramped to 1623 K, and held

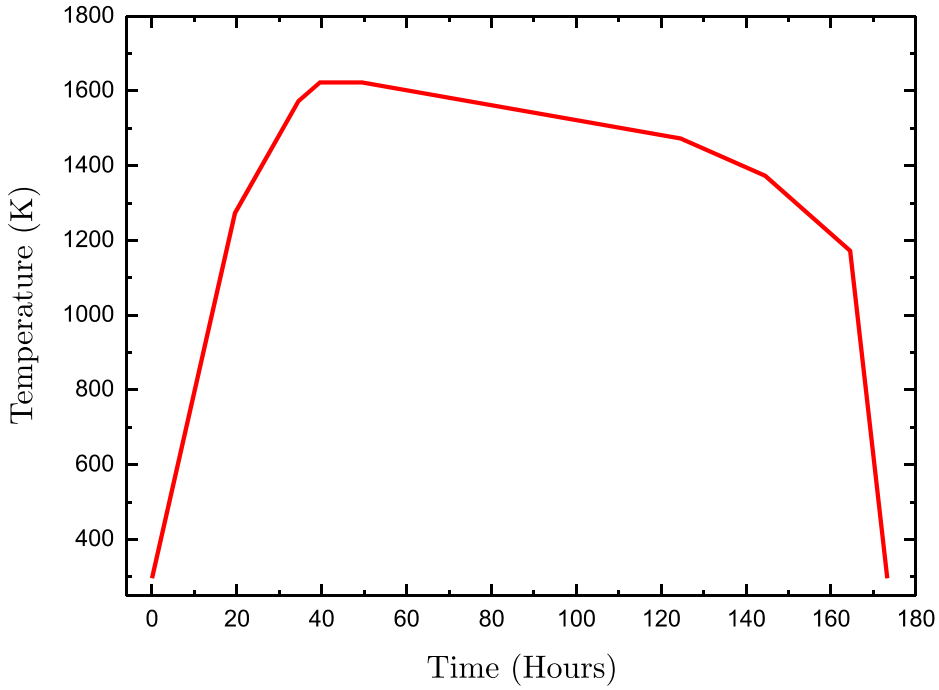

Figure 3-1: An example thermal profile for a crystal melt synthesis using the bulk flux method

there for a 10 hour dwell. Following the dwell, the furnace was cooled, initially at $2\,\mathrm{K\,h^{-1}}$ for 25 hours, then for 20 hours at $5\,\mathrm{K\,h^{-1}}$, 20 hours at $10\,\mathrm{K\,h^{-1}}$ and finally a rapid cooling section ($100\,\mathrm{K\,h^{-1}}$) down to room temperature. Small, platelet-like crystals were retrieved from the bulk by washing with acid.

$\mathbf{BaBi_2Nb_2O_9}$

Numerous attempts were made at growing barium-containing Aurivillius single crystals, which were all characterized by small crystals indicative of insufficient cooling time and Bi loss, and a loss of barium into the flux. To suppress this, $BaCO_3$ was added to the flux stoichiometrically with respect to the Bi_2O_3. The ratio of boron oxide was also doubled to suppress the number of nucleation sites and thus result in fewer, larger crystals. The $BaBi_2Nb_2O_9$:Bi_2O_3:B_2O_3:$BaCO_3$ ratios set to 1:3:1:1. A dwell of 10 hours at 1423 kelvin was followed by a 75 hour cool at $2\,\mathrm{K\,h^{-1}}$ down to 1273 K. The cooling rate was then increased to $4\,\mathrm{K\,h^{-1}}$ for 12.5 hours, then $10\,\mathrm{K\,h^{-1}}$ for 5 hours, then $20\,\mathrm{K\,h^{-1}}$ for 5 hours, followed finally by the rapid cooling at $100\,\mathrm{K\,h^{-1}}$ to room temperature.

$CsBiNb_2O_7$

Given that our attempts at ceramic synthesis using the instructions of Snedden et al. [2] yielded crystals, attempts were made at a straight melt of the pure ceramic, but the crystals formed in this manner were too small for optical studies. For this reason, an adapted version of our previously described bulk flux method for the analogous Aurivillius phases was used. However, attempts at varying the composition of the flux did not yield crystals of larger size - indeed, use of the flux seemed to suppress crystal growth completely. For this reason, the small crystals formed in the straight melt of the ceramic were used for structural work, and no optical experiments were possible.

3.2 Experimental Details

Single-Crystal diffraction was performed on an Oxford Diffraction Gemini system, with MoKα radiation monochromated with graphite. The x-ray generator was set with a tension of 33kV to remove the $\lambda/2$ transition x-rays which are emitted when the generator is set to more than 34kV. The diffractometer was fitted with an Oxford Diffraction Ruby detector, incorporating a 2k × 2k Kodak chip and a 135mm diameter active area. Crystal sizes were typically in the range $100\mu m$-$200\mu m$, and were cemented to a glass fibre with epoxy resin which in turn was fixed to a metal pin in a Huber XYZR goniometer head with wax. Except where stated otherwise, measurement strategies with a 0.3° scan width were used. After integration, the collected data were corrected for absorption via the analytical method of Clark and Reid[3]. Two methods of structure solution and refinement were utilized; in the first, the space group was ascertained via the *GRAL* applet of the Oxford Diffraction *CrysAlisPro* software. The outputted *.hkl* files were then solved using *SIR–92* and refined in *Shelx97*[4], both using the *WinGX32* package[5]. The second method used JANA2006[6], and employed charge flipping for structure solution using the applet *SUPERFLIP*[7]. The flipped charge density was then tested for symmetry before being refined in JANA2006.

3.3 $SrBi_2Nb_2O_9$

Small (100 μm – 100 μm), platelet-like single-crystals of $SrBi_2Nb_2O_9$ were retrieved from the melt and these were used for single-crystal diffraction. Once a suitable piece of crystal was found, comprising of a single domain with no visible cracks, a strategy employing a mixture of ϕ and ω scans was used, to collect data from the whole Ewald sphere to a resolution of 0.5 Å. The counting time per frame was 8+8 s (correlated), and a scan width of 0.3° was used, to increase redundancy and resolution.

The data were integrated under the constraint of *mmm* Laue symmetry, yielding internal consistency values of R_{int}=0.017 on data to 0.8 Å and 0.064 on data to 0.51 Å. An analytical absorption correction was applied, based on the crystal shape and the data was refinalized with A-centering. The outputted hkl file was charge-flipped with Superflip, with the input file prepared by JANA2006. The cation assignment from Superflip was adjusted to match that from the powder refinement, and a normal refinement ensued. This yielded an R_{obs} of 11.24. Owing to the fact that the space group is non-centrosymmetric, and metrically tetragonal, merohedral twinning was anticipated. For this reason, during the refinement, inversion and rotation twinning were introduced. This gave an R_{obs} of 8.75, and twin volumes of 26.9% for the inversion twin, 28.7% for a 90° rotation twin, and 15.04% for the inverted 90° rotation twin (29.36% original component). The introduction of the mixing of the Bi and Sr on both sites reduced the R_{obs} further to 5.91. A summary of the refinement is given in table 3-1, and the refined structure is shown in figure 3-2. The cations were refined with harmonic anisotropic thermal parameters, and when two atoms shared a site (because of Bi and Sr mixing) the thermal parameters were constrained to be equal. The occupancies were constrained to sum to unity but the overall occupancies were not constrained to stoichiometry and so a refined composition of $Sr_{1.009}Bi_{1.991}Nb_2O_9$ was found.

Table 3-1: Refinement details for single-crystal diffraction of $SrBi_2Nb_2O_9$, $BaBi_2Nb_2O_9$, and $CsBiNb_2O_7$ at ambient temperature

Refined Composition	$Sr_{1.009}Bi_{1.991}Nb_2O_9$	$CsBiNb_2O_7$	$Ba_{1.014}Bi_{1.986}Nb_2O_9$
Formula Weight	834.32	639.69	884.13
Crystal System	Orthorhombic	Orthorhombic	Tetragonal
Temperature	298 K	298 K	298 K
Space Group	$A2_1am$	$P2_1am$	$I4/mmm$
$\boldsymbol{a}$	5.5275(7)	5.5118(5)	3.94935(9)
$\boldsymbol{b}$	5.5270(7)	5.4372(5)	$=\boldsymbol{a}$
$\boldsymbol{c}$	25.2157(16)	11.4032(11)	25.71347(17)
Volume	761.68(1)	341.73(1)	401.05(1)
Density	$7.1914\,\mathrm{Mg\,m^{-3}}$	$6.214\,\mathrm{Mg\,m^{-3}}$	$7.3191\,\mathrm{Mg\,m^{-3}}$
Absorption coefficient	$58.289\,\mathrm{mm^{-1}}$	$35.97\,\mathrm{mm^{-1}}$	$54.107\,\mathrm{mm^{-1}}$
F(000)	1430	552	725
Crystal size	Cuboidal, 100 –200 μm^3	Platelet, 200 μm^2×20 μm	75×110×160 μm^3
Index Ranges	$-8 \le h \le 8$ $-8 \le k \le 8$ $-42 \le l \le 40$	$-10 \le h \le 10$ $-10 \le k \le 9$ $-18 \le l \le 22$	$-7 \le h \le 7$ $-7 \le k \le 7$ $-29 \le l \le 50$
Radiation	MoKα	MoKα	MoKα
Reflections collected	25853	11276	11510
Unique Reflections	5895	2624	1268
Completeness	94.4% to 0.51 Å	95.0% to 0.51 Å	73.8% to 0.51 Å
Absorption correction	yes	yes	yes
Refinement method	Full-Matrix Least-Squares on $\lvert\mathbf{F}\rvert^2$	Full-Matrix Least-Squares on $\lvert\mathbf{F}\rvert^2$	Full-Matrix Least-Squares on $\lvert\mathbf{F}\rvert^2$
Parameters	47	37	15
R_{obs}	5.91	6.54	17.72

This refinement is in good agreement both with the structure as proposed in previous studies [8, 9] and the powder diffraction performed in this work.

Table 3-2: Refined atomic co-ordinates and atomic displacement parameters for $SrBi_2Nb_2O_9$ at room temperature, from single-crystal diffraction data

Atom	x	y	z	SOF	U_{11}(Å^2)	U_{22}(Å^2)	U_{33}(Å^2)	U_{12}(Å^2)	U_{13}(Å^2)	U_{23}(Å^2)
Sr1	0	0.7630(4)	0.2567(5)	0.725	0.0075(3)	0.0294(14)	0.0328(15)	0	0	-0.0198(11)
Bi1	0	0.7630(4)	0.2567(5)	0.275	0.0075(3)	0.0294(14)	0.0328(15)	0	0	-0.0198(11)
Bi2	0.202125(18)	0.7341(2)	0.256825	0.858	0.01542(16)	0.0163(4)	0.0170(4)	0.0043(3)	0.0045(3)	-0.0009(5)
Sr2	0.202125(18)	0.7341(2)	0.256825	0.142	0.01542(16)	0.0163(4)	0.0170(4)	0.0043(3)	0.0045(3)	-0.0009(5)
Nb1	0.08651(3)	0.2516(2)	0.2785(4)		0.0076(3)	0.0062(13)	0.0050(12)	0.0003(4)	0.0008(4)	-0.0017(6)
O1	0.2492(4)	0.997(3)	0.021(2)		0.0115(12)	0.0115(12)	0.0115(12)	–	–	–
O2	0.1603(4)	0.2895(19)	0.301(2)		0.018(2)	0.018(2)	0.018(2)	–	–	–
O3	0	0.212(3)	0.304(3)		0.014(2)	0.014(2)	0.014(2)	–	–	–
O4	0.0837(4)	-0.033(2)	0.080(2)		0.015(2)	0.015(2)	0.015(2)	–	–	–
O5	0.0711(3)	0.480(2)	0.021(3)		0.0163(18)	0.0163(18)	0.0163(18)	–	–	–

Table 3-3: Refined atomic co-ordinates and atomic displacement parameters for $BaBi_2Nb_2O_9$ at room temperature, from single-crystal diffraction data

Atom	x	y	z	SOF	$\mathbf{U}_{11}$(Å^2)	$\mathbf{U}_{22}$(Å^2)	$\mathbf{U}_{33}$(Å^2)	$\mathbf{U}_{12}$(Å^2)	$\mathbf{U}_{13}$(Å^2)	$\mathbf{U}_{23}$(Å^2)
Ba1	0.5	0.5	0	0.535	0.055(3)	0.055(3)	0.0052(13)	0	0	0
Bi1	0.5	0.5	0	0.465	0.055(3)	0.055(3)	0.0052(13)	0	0	0
Bi2	0.5	0.5	0.20004(9)	0.737	0.0233(4)	0.0233(4)	0.0515(10)	0	0	0
Ba2	0.5	0.5	0.20004(9)	0.263	0.0233(4)	0.0233(4)	0.0515(10)	0	0	0
Nb1	0	0	0.08871(7)		0.0113(4)	0.0113(4)	0.0116(7)	0	0	0
O1	0.5	0	0.25		0.018(3)	0.018(3)	0.018(3)	–	–	–
O2	-0.5	0	0.0784(6)		0.023(2)	0.023(2)	0.023(2)	–	–	–
O3	0	0	0.1596(8)		0.022(3)	0.022(3)	0.022(3)	–	–	–
O4	0	0	0		0.030(6)	0.030(6)	0.030(6)	–	–	–

	$\mathbf{d}_{1111}$	$\mathbf{d}_{1122}$	$\mathbf{d}_{1133}$	$\mathbf{d}_{2222}$	$\mathbf{d}_{2233}$	$\mathbf{d}_{3333}$
			$\times 10^{-3}$			
Ba1	0.0464512	-0.196873	-0.000633	0.464512	-0.000633	-0.000007
		$\times 10^{-4}$				
Bi1	-0.003704	-0.003074	-0.001696			

Table 3-4: Internal R values for the data collected from $BaBi_2Nb_2O_9$ merged in different Laue classes

Crystal System	Laue Group	$R_{int}(I > 3\sigma)$	R_{int}(All)
Triclinic	-1	3.64	3.79
Monoclinic ***b*** (1^{st})	$2/m$	4.17	4.36
Monoclinic ***c*** (2^{nd})	$2/m$	4.11	4.30
Monoclinic ***a*** (3^{rd})	$2/m$	4.15	4.33
Orthorhombic	mmm	4.46	4.65
Tetragonal	$4/m$	4.88	5.08
Tetragonal	$4/mmm$	4.97	5.16

3.4 $BaBi_2Nb_2O_9$

Recently, the structure of $BaBi_2Nb_2O_9$ has been the subject of much debate in the literature. Ismunandar et al. [10] asserted that $BaBi_2Nb_2O_9$ formed in the same space group as $SrBi_2Nb_2O_9$, namely $A2_1am$. This was refuted by Blake et al. [8], who could not measure any significant distortion from the prototypic, tetragonal $I4/mmm$ structure. Since both these studies (and all others to date) employed powder diffraction it was hoped that single-crystal diffraction could both lend credence to one of these hypotheses, and finally elucidate the true structure. The crystal used in this experiment was of approximate dimensions $76 \times 111 \times 164\,\mu m^3$. The collection combined 60 s exposures and a 0.3° step width to maximize the quality of the data. Exposures were taken to a resolution of 0.5 Å, and assuming the tetragonal cell suggested by Ismunandar et al. [10], the completeness to this resolution was 99.75%, with a redundancy of 3.8. The total time for the run was 72 hours. Initially, the frames were integrated in a tetragonal I-centred lattice with the aim of performing a refinement in the highest suggested symmetry, $I4/mmm$. The structure solution from charge flipping using SUPERFLIP, the Patterson routine of SHELXS, and the SIR-92 routine in WinGX were all unsatisfactory. All three methods of solution suffered from incorrect cation assignment and failure to locate correctly the oxygen sites. Despite this, a converging refinement was obtained, albeit with substantial manual assignments, and a summary of this can be seen in table 3-1.

To allow for cation mixing as is standard for the Aurivillius materials, this model includes a refined occupation of the bismuth and barium sites, yielding a

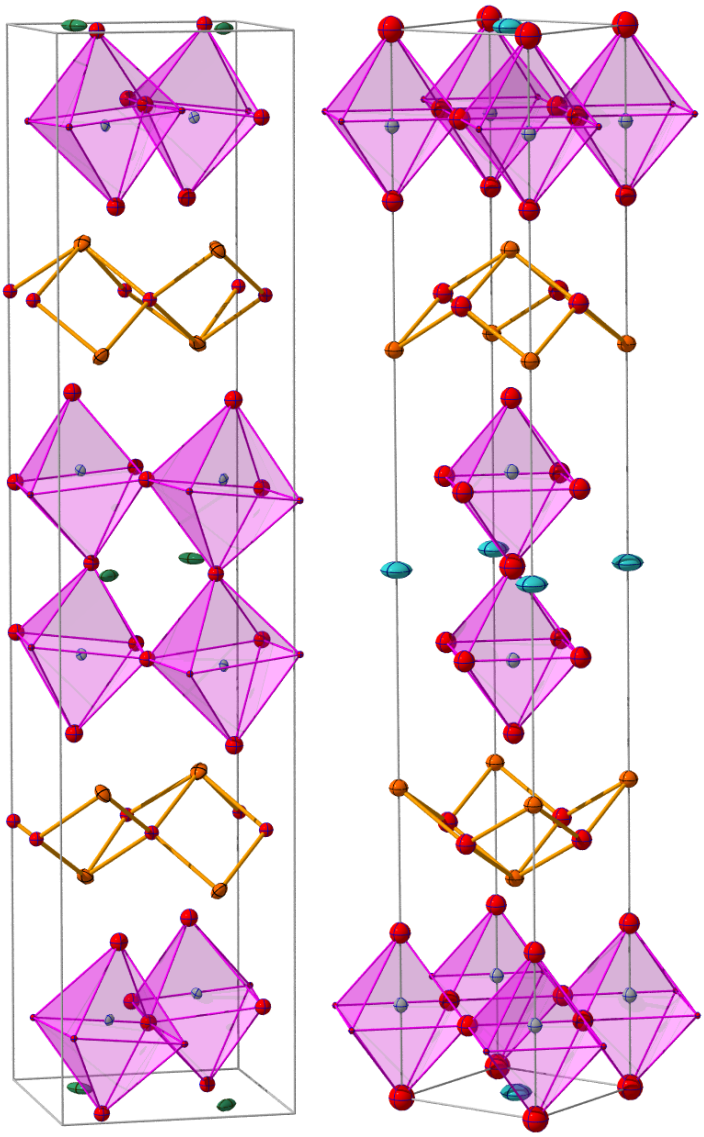

(a) $SrBi_2Nb_2O_9$ (b) $BaBi_2Nb_2O_9$

Figure 3-2: Refined structures of $SrBi_2Nb_2O_9$ (a) and $BaBi_2Nb_2O_9$ (b) from single-crystal x-ray diffraction data, with the structures rotated to aid visual comparison. $SrBi_2Nb_2O_9$ is refined in the polar space group $A2_1am$ whereas $BaBi_2Nb_2O_9$ is fitted in the centrosymmetric $I4/mmm$. The refinement of $BaBi_2Nb_2O_9$ in this space group is unsatisfactory. Full details of these refinements can be seen in table 3-1.

refined composition that is also included in table 3-1.

The unsatisfactory R value (17.72) of this refinement, however, suggests that there is something fundamentally wrong with this model. A comparison of the internal R values of the data merged under different Laue classes is shown in table 3-4. These values of internal consistency suggest that the Laue group of $4/mmm$

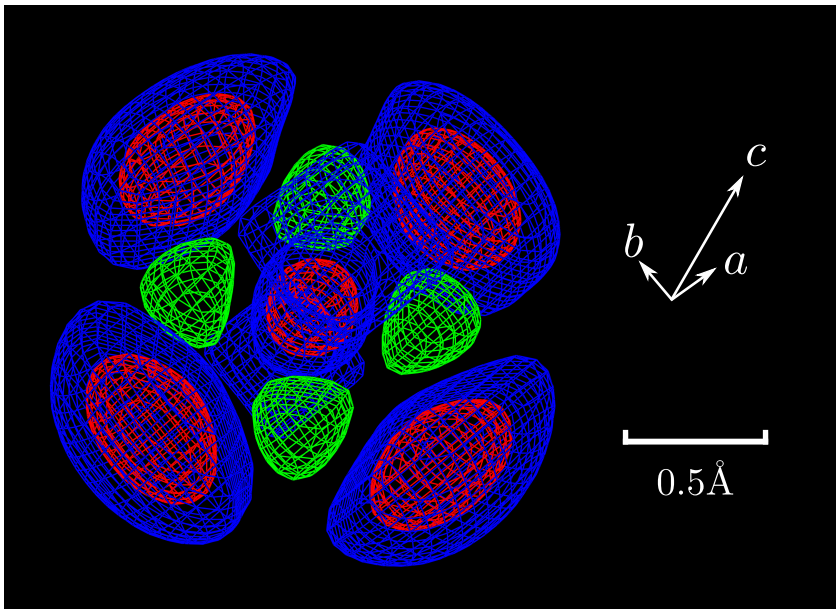

Figure 3-3: Difference Fourier maps of the barium site in $BaBi_2Nb_2O_9$. The surfaces represent electron densities of $-15.6\,e\,Å^{-3}$ (green); $2.28\,e\,Å^{-3}$ (blue); and $14.453\,e\,Å^{-3}$ (red). The density maxima are $35.5\,e\,Å^{-3}$ in the central area, $34.4\,e\,Å^{-3}$ in the four "lobes", and the minima is $-28.3\,e\,Å^{-3}$ in the areas of negative density.

is correct, as no substantial improvement is found by reducing the symmetry.

Since the largest residual Fourier peaks in this refinement appear close to the Ba site, a Fourier difference map is calculated for a 3×3×3 Å volume around the Ba site, a contour map of which is shown in figure 3-3. The model clearly underestimates the density at the site itself, whilst simultaneously overestimating the density at a region 0.4 Å from the site in the [110] direction.

To ensure the symmetry of these areas of negative density are not a result of merging in tetragonal symmetry, the same model was applied to unmerged data; *i.e.* data still in $P1$. The atom was then removed from the model, the Fourier map taken, and the resulting contour map is seen in figure 3-4. This shows that the unusual shape of the density at the Ba site is inherent to the data, and not due to the merging or the refinement. To attempt to account for the unusual shape of the density around the barium and bismuth sites, anharmonic ADPs were applied, using JANA2006. These higher-order terms, in the form of higher-rank tensors, can reflect real distortions of the thermal ellipsoid to form shapes that require a more complicated description than a tensor of rank 2. The

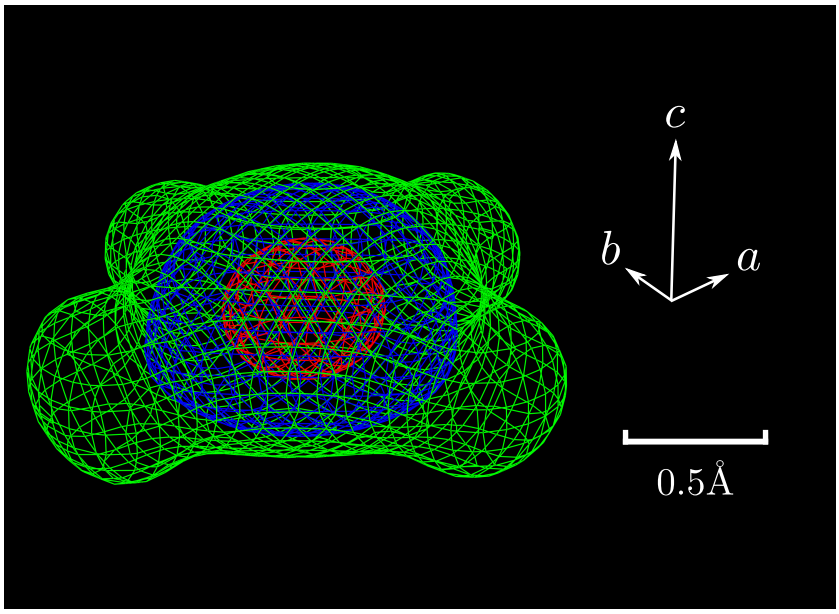

Figure 3-4: Fourier plot of Ba site, in space group $P1$, with the barium atom removed from the model, to reveal the observed density. The surfaces represent electron densities of 28.7 e Å^{-3} (green); 58.5 e Å^{-3} (blue); and 169.6 e Å^{-3} (red).

order of the anharmonicity is the highest rank of tensor used to describe the displacements, and tests of the order required to describe the anisotropic density are shown in table 3-5. The effect of using different orders of anharmonicity on the barium and bismuth site is also shown in this table, as well as a comparison with refinement using just harmonic ADPs, $\mathbf{U}_{ij}$. It was soon discovered that upon applying anharmonic terms to the ADPs the occupancy of both the bismuth and barium sites returned to stoichiometry, *i.e.* the site occupancy factor for bismuth on the barium site refined to zero. This model was adopted for all the refinements in table 3-5, hence the R_{obs} of the harmonic refinement is higher than quoted earlier (20.96 cf. 17.72).

Further analysis of the probability distribution functions (PDFs) of both these sites, coupled with these values of R_{obs} leads to the conclusion that the best, most realistic fit, is to use third-order corrections on the bismuth site and fourth-order on the barium site. This leads to the PDF surfaces shown in figure 3-5. Applying higher-order corrections to the bismuth site make only marginal differences to the PDFs, and applying higher-order terms to the barium site result in unrealistic probability densities.

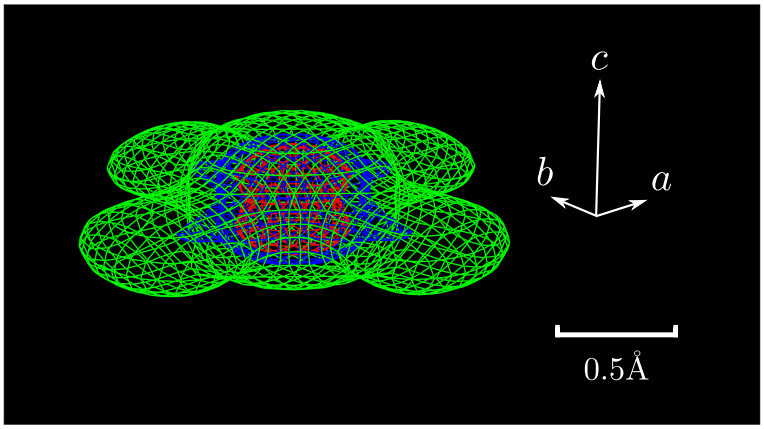

(a) Ba site PDF. Green = 0.44 $Å^{-3}$, Blue = 2.88 $Å^{-3}$, Red = 7.23 $Å^{-3}$

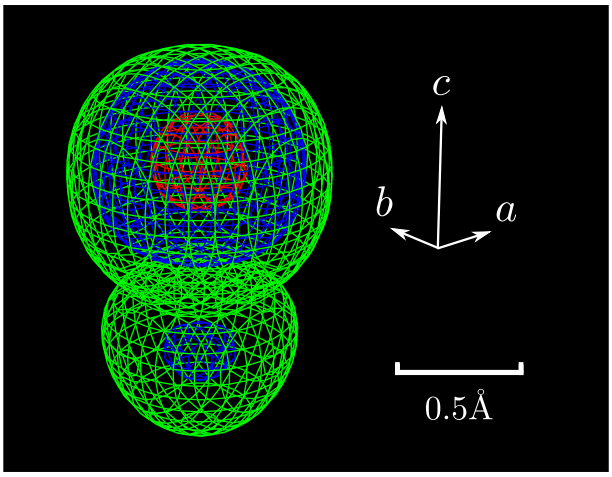

(b) Bi site PDF. Green = 0.52 $Å^{-3}$, Blue = 2.97 $Å^{-3}$, Red = 11.07 $Å^{-3}$

Figure 3-5: Probability distribution contour plots of the bismuth and barium sites in $BaBi_2Nb_2O_9$ after refinement with anharmonic thermal parameters. The barium site is refined with fourth-rank coefficients, and the bismuth with third-rank.

Table 3-5: Effect on R_{obs} of introducing, and increasing the rank, of anharmonic ADPs on both the barium and the bismuth sites, in $BaBi_2Nb_2O_9$. Here, $\mathbf{d}_{jklm}$ means that the relevant components of a fourth rank tensor have been used in the refinement. The odd-rank terms for the barium site are zero by definition due to the inversion symmetry of the point group. $\mathbf{U}_{ij}$ signifies standard harmonic ADPs.

Ba	**Bi**				
	$\mathbf{U}_{ij}$	$\ldots+\mathbf{c}_{jkl}$	$\ldots+\mathbf{d}_{jklm}$	$\ldots+\mathbf{e}_{jklmn}$	$\ldots+\mathbf{f}_{jklmnp}$
$\mathbf{U}_{ij}$	20.96	12.3	11.84	11.73	11.34
$\ldots+\mathbf{d}_{jklm}$	17.93	8.97	8.13	8.01	8.14
$\ldots+\mathbf{f}_{jklmnp}$	14.52	7.06	5.53	5.19	4.90

It has been well documented in the literature [11–13] that $BaBi_2Nb_2O_9$ displays dielectric behaviour characteristic of a relaxor ferroelectric. Studies on the archetypal relaxor, $Pb(Mg_{1/3}Nb_{2/3})O_3$, conclude that although the structure is macroscopically cubic, it contains polar nano-regions that have differing values of T_c [14]. This model is invoked to account for the dielectric behaviour seen in this and other metrically centrosymmetric structures.

In $BaBi_2Nb_2O_9$, the bismuth anisotropy can be attributed to the existence of the $6s^2$ lone pair inherent to bismuth. The highly anisotropic ADPs have also been noticed in previous work on the isostructural analogue $SrBi_2Ta_2O_9$ [15], and on $BaBi_2Nb_2O_9$ itself [10] (albeit in the incorrect space group $A2_1am$). These studies both measured a grossly inflated isotropic ADP, which was attributed to displacement of the bismuth from the high symmetry site, and used to explain the physical properties. Since both of these studies were based on powder neutron diffraction, however, even harmonic ADP refinement yielded physically unrealistic results.

In the comprehensive study by Macquart et al. [16], using both x-rays and neutrons, a large isotropic ADP is also measured; this is not commented on by the authors. Using a cryofurnace, however, they show evidence for a tetragonal-tetragonal phase transition between 300K and 350K, and assign the lower temperature phase the space group of $I4mm$. Their arguments for this are twofold; it helps to explain the physical properties, and explains the continuity of the phase transition they observe. However, the removal of the mirror plane from the z-

direction implies that any spontaneous polarization would exist parallel to z, and this is not observed in any of the Aurivillius phases. Attempts to refine the present data in $I4mm$ had only marginal effects on the quality of the refinement and the bismuth positions (R_{obs}=8.97; Bi_{1z}=0.2000(2); Bi_{2z}=0.7999(2); and R_{obs}=8.92; Bi_{1z}=0.2000(2); Bi_{2z}=0.7991(2) for $I4/mmm$ and $I4mm$ respectively). There was a marginal overall displacement of the niobium atoms (Nb_{1z}=0.0879(2); Nb_{2z}=-0.0900(2)) but the insignificant change in R_{obs} meant that refinements in $I4mm$ were rejected.

In the work by Blake et al. [8], cation mixing is allowed to occur, with bismuth and barium jointly refining on the two sites. With stoichiometry maintained by constraint, they account for the relaxor nature of $BaBi_2Nb_2O_9$ using a cation disorder model. Whilst this model yields good refinements for the current single-crystal work on $SrBi_2Nb_2O_9$, without the need to constrain the occupancies to maintain stoichiometry, a significant improvement is found by allowing anharmonic ADPs, at which point the disorder (that is, the amount of barium on the bismuth site) refines to zero.

The barium anisotropy is unusual, however, and may be due to displacements of the atom from the prototypic site, as suggested for bismuth by Ismunandar et al. [10] and Shimakawa et al. [15]. The direction of the distortion of the probability density suggests that if this is an indication of polar nano-domains, the polarization would occur in the $a-b$ plane. Attempts at refinement of the data using a slight distortion of the structure from $I4/mmm$ were unsuccessful.

3.5 $CsBiNb_2O_7$

$CsBiNb_2O_7$ belongs to a family of structures closely related to the Aurivillius family, known as the DionJacobson (DJ) series. The similarity lies in the stacked perovskite portion of the structure, but the families differ in the interstices and the valency of the non-bismuth cation, which in the DJ case is an alkaline metal. The crystal morphology for the $CsBiNb_2O_7$ was thin platelets, with the c-axis normal to the plate. Whilst the Aurivillius materials tended to grow in platelets 100 µm thick, the $CsBiNb_2O_7$ grew to be an order of magnitude thinner. The total

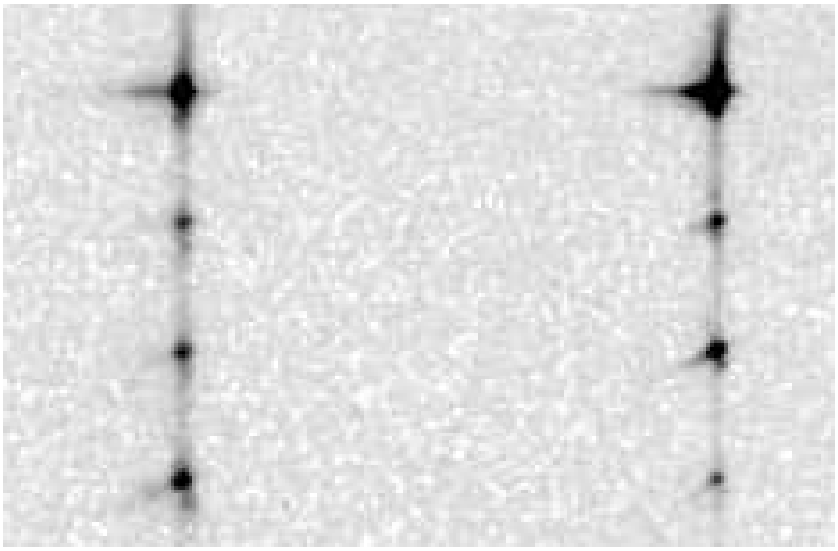

(a) Diffuse scattering in the $h0l$ plane

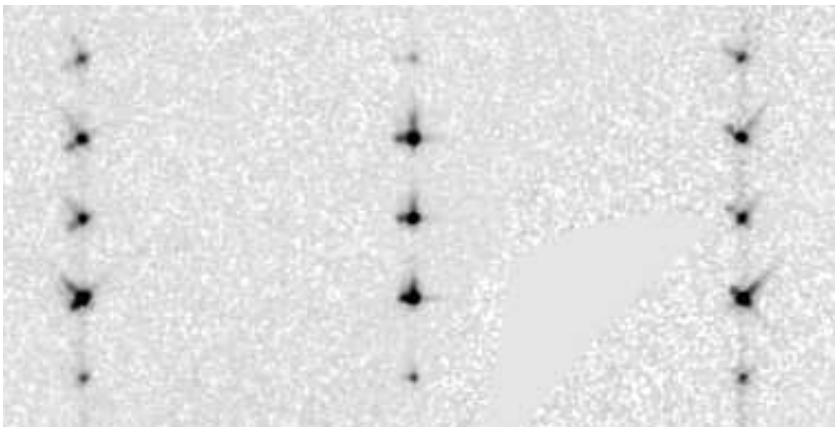

(b) Twinning in the $h0l$ plane

Figure 3-6: $h0l$ precession images of $CsBiNb_2O_7$, showing apparent diffuse scattering, (a) and twinning (b)

collection time for this experiment was 21 hours, which involved 8+8 s (correlated) exposures and a 0.3° step size. Upon collection of the data it became clear that this crystal exhibited diffuse scattering, as seen in figure 3-6. This can help to explain the unusually high internal agreement factor of R_{int} = 0.133 to a resolution of 0.51 Å in this collection. The diffuse scattering implies that there exists one or more degrees of disorder from the ideal, ordered cell, and that this disorder will serve to reduce the accuracy of any refinement. This crystal also seems to exhibit twinning, as seen in figure 3-6.

In figure 3-6b there is also evidence for a twin component in this crystal. However, due to the very small peak separation and relatively low intensity of the

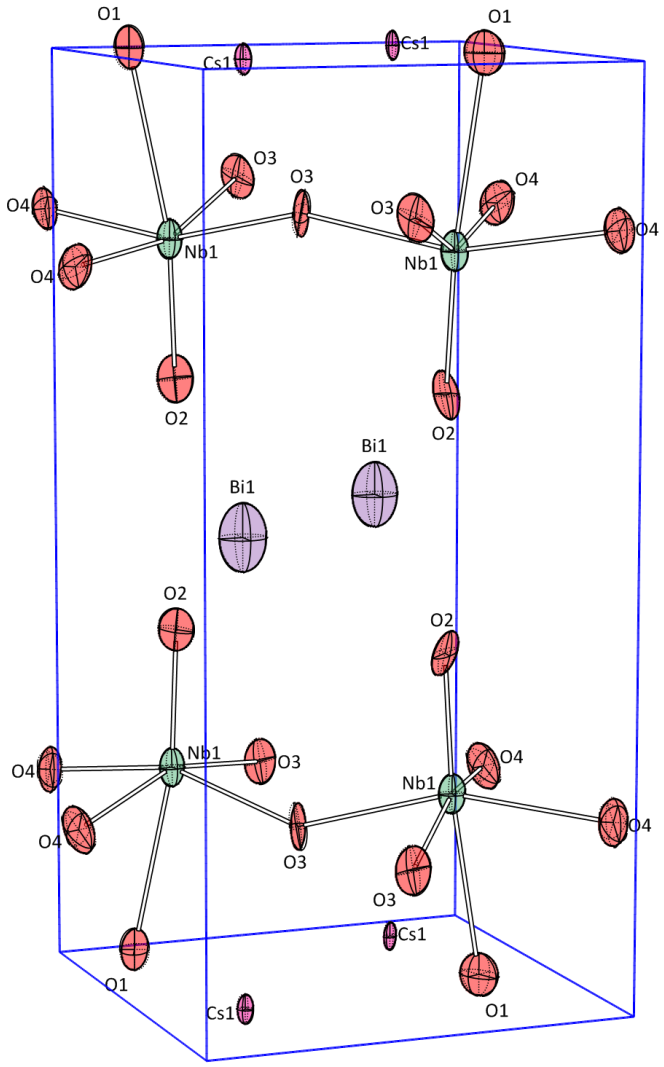

Figure 3-7: Atom labels used in the discussion of $CsBiNb_2O_7$. O1 is the linking apical site, O2 is the outer apical site, and O3 and O4 are the equatorial sites.

smaller component, it was not possible to resolve enough peaks for a refinement. Indeed, many of the peaks were so close to their "partner" that the intensity of both peaks was included under the integration mask.

A summary of the refinement parameters for the average structure appear in table 3-1. Whilst the R_{obs} value of 7.04 is acceptable for a final structure solution, it was decided to study the Fourier difference maps to elucidate further the structural element or elements responsible for the diffuse scattering. The atom naming nomenclature used in the following discussion is shown in figure 3-7.

To ensure the correct phasing of the observed data, Fourier difference maps

were taken of the refined model with the relevant atom removed, to leave just the observed data. The contour maps for the cations are shown in figure 3-8. These show that all three of the cations present in the structure seem to occupy more than one site, with these sites all appearing in the $x - y$ plane, particularly with a splitting in the polar a-direction. Also worthy of note is the difference in the relative intensities of the two peaks from each cation site: whilst the bismuth sites have a ratio of 0.92:1, the cesium and niobium sites have ratios of 0.44:1 and and 0.74:1 respectively. Analysis of the oxygen sites (figure 3-9) reveals a slightly different trend: the apical oxygen sites split similarly to the cations, whereas the equatorial sites split to a larger degree.

This seems to indicate that the solved structure is not an "average" structure as is the norm for disordered materials; rather, it is the solution to one of two unit cells (denoted hereafter as A and B, for the modelled and unmodelled structures respectively) that appear disordered in the bulk. The displacements of the apical oxygens by a small distance (0.86 Å and 0.56 Å) compared to the equatorial oxygens (1.6 Å and 2.18 Å) suggests that the B cell involves a twisting of the oxygen octahedra around the z-axis. This is coupled with a displacement of some or all three of the cations, since the Bi splitting may simply be a result of the lone pair effect on the measured electron density. Since the disorder appears in the z-direction (figure 3-6), the overall structure appears to be sheets of unit cell "A" or "B", with no ordering of this in the z-direction. It is also a possibility however, that these splittings are due to the "twin" component not being being fully measured, although taking the density maps using only the high angle data (those reflections where the peaks from the B lattice are less covered by the integration mask) suggest that this is not the case.

3.6 The tetragonality of $BaTiO_3$

Barium Titanate, $BaTiO_3$, is a well-known, and well-studied ferroelectric, forming in the archetypal perovskite phase. The room-temperature structure of $BaTiO_3$ has long been acknowledged as tetragonal with lattice parameters as ascertained by Clarke [17] of 3.9935(5) Å and 4.0385(5) Å. This structure is the basis upon

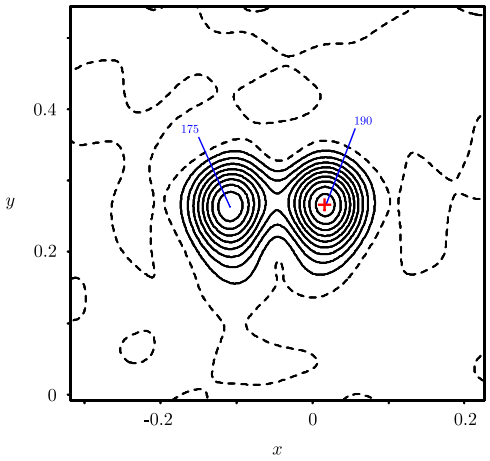

(a) Bi, xy plane, $z = 0.5$

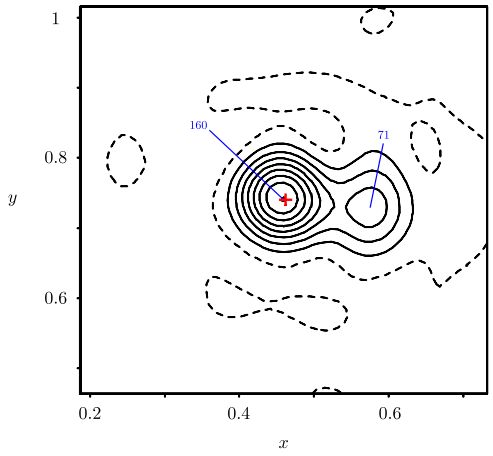

(b) Cs, xy plane, $z = 0.0$

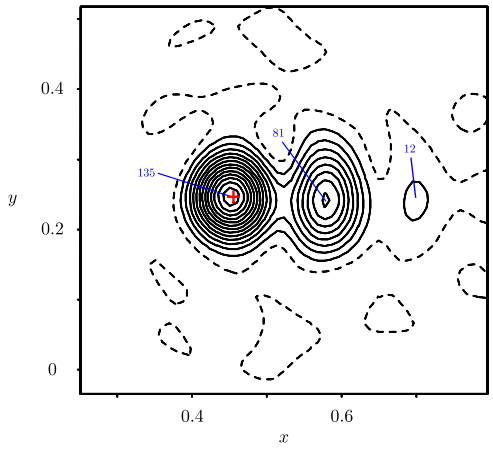

(c) Nb, xy plane, $z = 0.293$

Figure 3-8: Fourier difference plots of cations in $CsBiNb_2O_7$, 0.05 Å thick, with the atom removed from the model to show observed data; Bismuth, (a); Cesium, (b); Niobium, (c). The maxima of electron density are shown in blue. In each case the red cross indicates the refined position of the atom in question.

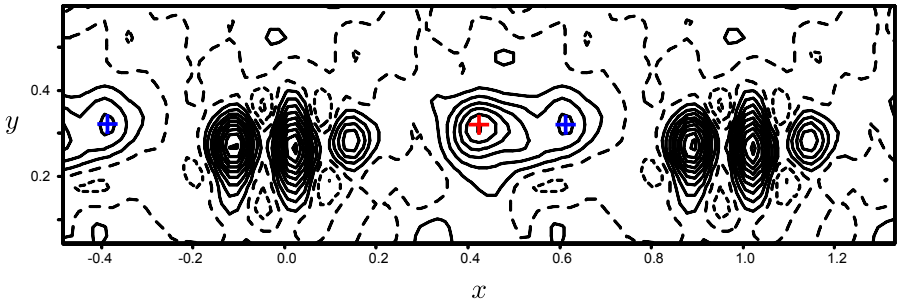

(a) O_1 (apical), xy plane, $z = 0.5$, including the bismuth site

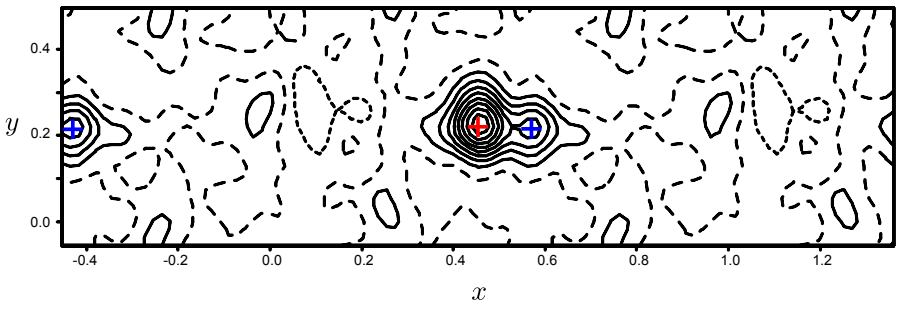

(b) O_2 (apical), xy plane, $z = 0.140$

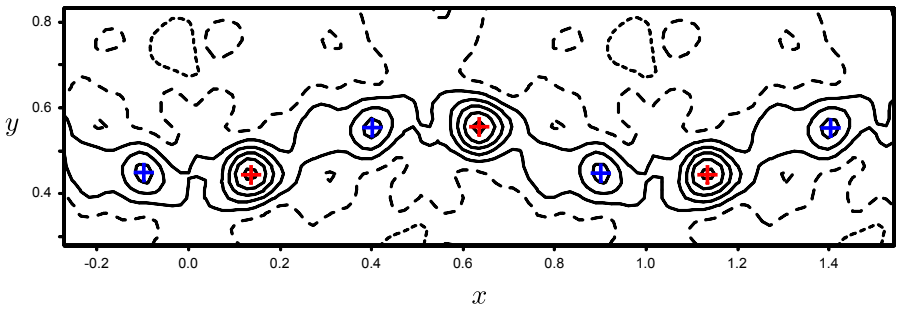

(c) O_3 (equatorial), xy plane, $z = 0.314$

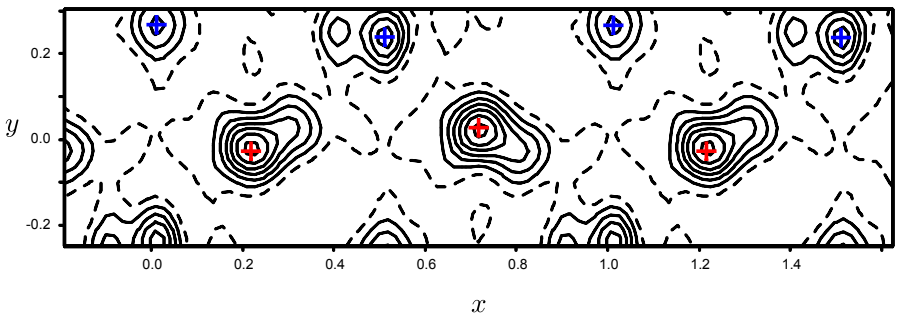

(d) O_4 (equatorial), xy plane, $z = 0.340$

Figure 3-9: Fourier difference plots of oxygen sites in $CsBiNb_2O_7$, 0.05 Å thick, with the atom removed from the model to show observed data; Apical, (a) and (b); and Equatorial, (c) and (d). In each case the red cross indicates the refined position of the atom in question, and the blue cross shows the peaks of electron density unaccounted for by the model.

which all measurements since have been interpreted, and was fully accepted in the literature. Recently, some studies on top-seeded single-crystals by Yoshimura and co workers[18–20] led them to conclude that in fact $BaTiO_3$ forms at room temperature as a tetragonal-monoclinic coherent hybrid structure; a co-crystal of two distinguishable lattices. The crystallographic basis for this was unclear, but their experimental evidence - x-ray precession images of major reciprocal lattice planes demonstrating extra Bragg spots - was easily explained by this model. In another recent publication[21] $BaTiO_3$ crystals were formed wholly in a monoclinic structure by the application of a field during cooling from the melt. Considering this, and with data of not high enough quality in the publication of Yoshimura et al. [19] to comment on their analysis, it seemed a matter of urgency to repeat these experiments to reinvestigate the room-temperature structure of $BaTiO_3$ with modern methods[22].

A 50×65×105 μm piece of top-seeded $BaTiO_3$ was mounted on a glass fibre with epoxy resin. This was, in turn, held into a metal pin in a Huber XYZR goniometer head with wax. The experiment was performed on an Oxford Diffraction Gemini CCD diffractometer, with MoKα (λ=0.710 69 Å) radiation. The detector was withdrawn to its maximum operating distance of 120 mm from the sample, to maximise resolution. Reflections from the full Ewald sphere were then collected, to a resolution of 0.4 Å. Precession images of the three principal lattice planes in reciprocal space were then formed, to ascertain whether the extra Bragg spots, as seen in previous work, were observed in the present study. Whilst no splitting was seen in the $hk0$ or $0kl$ planes, splitting very similar in nature to that of Yoshimura et al. [20] was seen in the $h0l$ plane. The $h0l$ precession image is shown in figure 3-10, and images of the $hk0$ and $0kl$ planes in Appendix A.

Closer study of the $h0l$ precession image shows a splitting of Bragg peaks into a main and satellite peak, with this occurring in the upper right, and lower left quadrants (h,l positive, and h,l negative respectively). The satellite peaks' distribution follows 2 fold rotational symmetry about $\mathbf{b}^*$, *i.e.* $\Delta\mathbf{H}^*(h0l) = -\Delta\mathbf{H}^*(\bar{h}0\bar{l})$ where $\Delta\mathbf{H}^*$ is the vector describing the displacement of the satellite from the corresponding main peak, $h0l$. This pattern of splitting into major and minor peaks is also seen in planes of higher order, in the hnk planes, and no splitting is seen

Table 3-6: The lattice parameters of the major and minor twin components in $BaTiO_3$

Lattice	a (Å)	c (Å)	Reflections indexed (total reflections)	Percentage indexed
Major	3.9993(1)	4.0425(2)	9477 (9478)	99.99%
Minor	3.996(3)	4.040(2)	718 (777)	92.4%
Clarke [17]	3.9935(5)	4.0385(5)		

in the *hkn* or *nkl* planes.

In order to analyse the origin of this splitting, the peaks were divided into two distinct lattices, henceforth known as the "major" (main reflections) and "minor" (satellite reflections) lattices, as also shown in figure 3-10. The major and minor lattices were indexed separately using the twinning subroutine of *CrysAlis*. Both lattices indexed in a tetragonal cell, the lattice parameters of which, along with the number of peaks and indexing success percentage are seen in table 3-6. The twinning subroutine of *CrysAlis* also supplied us with relative orientation matrices of the two lattices with respect to the diffractometer, and hence the transformation matrix between the two lattices:

$$\begin{pmatrix} 0.009 & 1.0018 & 0.0006 \\ -0.0098 & -0.0003 & -0.9892 \\ -1.0125 & 0.0006 & 0.0084 \end{pmatrix}$$

which equates to a 119.7(3)° rotation around the $[11\bar{1}]$ direction in real space. Our analysis suggests, therefore, that the extra Bragg reflections are present in $BaTiO_3$ due to the existence of a twin, rotated close to 120° around the $[11\bar{1}]$, which equates to an exchange of the **a** and **c** axes. This threefold rotation, however, is almost certainly not the true twin operator, and has been suggested by the software just as a possibility by symmetry. Assuming the rotation is exactly 120°, the transformation matrix becomes that of $3\,[11\bar{1}]$;

$$\begin{pmatrix} 0 & 1 & 0 \\ 0 & 0 & -1 \\ -1 & 0 & 0 \end{pmatrix}$$

which can simply be formed as the product of two mirror planes, $m[1\bar{1}0]$ and

Table 3-7: Comparison of the major and minor twin lattice peaks in $BaTiO_3$

Reflection	hkl_{major} (measured)			hkl_{minor} (measured)			Displacement $\Delta\mathbf{H}^* = \Delta h\mathbf{a}^* + \Delta l\mathbf{c}^*$	Δd_{obs} (Å)	Δd_{calc} (Å)
300	3.007	0	0	2.978	0	0.03	-0.029$\mathbf{a}^*$+0.03$\mathbf{c}^*$	-0.013	-0.014
003	0.001	0	3.008	-0.028	0	3.038	-0.029$\mathbf{a}^*$+0.03$\mathbf{c}^*$	0.013	0.014
400	4.003	0	0	3.964	0	0.039	-0.039$\mathbf{a}^*$+0.039$\mathbf{c}^*$	-0.010	-0.011
201	2.012	0	0.996	1.973	0	1.036	-0.039$\mathbf{a}^*$+0.04$\mathbf{c}^*$	-0.014	-0.012
301	3.008	0	0.996	2.969	0	1.045	-0.039$\mathbf{a}^*$+0.039$\mathbf{c}^*$	-0.010	-0.011
103	1.007	0	3.008	0.968	0	3.047	-0.039$\mathbf{a}^*$+0.049$\mathbf{c}^*$	0.014	0.011
401	4.004	0	0.996	3.955	0	1.045	-0.049$\mathbf{a}^*$+0.049$\mathbf{c}^*$	-0.008	-0.009
104	1.007	0	3.994	0.949	0	4.053	-0.058$\mathbf{a}^*$+0.059$\mathbf{c}^*$	0.010	0.009
202	2.012	0	2.002	1.973	0	2.051	-0.039$\mathbf{a}^*$+0.049$\mathbf{c}^*$	0.004	0
302	3.008	0	2.002	2.959	0	2.051	-0.049$\mathbf{a}^*$+0.049$\mathbf{c}^*$	-0.004	-0.005
203	2.013	0	3.008	1.954	0	3.057	-0.059$\mathbf{a}^*$+0.049$\mathbf{c}^*$	0.003	0.005
303	2.95	0	3.067	3.018	0	2.998	-0.068$\mathbf{a}^*$+0.069$\mathbf{c}^*$	0.0002	0
402	4.004	0	1.992	3.946	0	2.061	-0.049$\mathbf{a}^*$+0.049$\mathbf{c}^*$	-0.004	-0.006
204	2.003	0	3.994	1.935	0	4.063	-0.068$\mathbf{a}^*$+0.069$\mathbf{c}^*$	0.006	0.006
403	4.005	0	2.998	3.927	0	3.077	-0.078$\mathbf{a}^*$+0.079$\mathbf{c}^*$	-0.002	-0.002
404	4.005	0	3.994	3.917	0	4.083	-0.088$\mathbf{a}^*$+0.089$\mathbf{c}^*$	$<10^{-5}$	0

$m[101]$;

$$\begin{pmatrix} 0 & 1 & 0 \\ 1 & 0 & 0 \\ 0 & 0 & 1 \end{pmatrix}\begin{pmatrix} 0 & 0 & -1 \\ 0 & 1 & 0 \\ -1 & 0 & 0 \end{pmatrix} = \begin{pmatrix} 0 & 1 & 0 \\ 0 & 0 & -1 \\ -1 & 0 & 0 \end{pmatrix}$$

Since the space group of $BaTiO_3$ is $P4mm$, and the first operator, $m[1\bar{1}0]$ is one of the symmetry elements of this space group, the $3\,[11\bar{1}]$ operation is crystallographically equivalent to the $m[101]$ operation, which is ubiquitous in the description of 90° twinning in tetragonal systems.

3.7 Single Crystal Structural Conclusions

The single-crystal study of $SrBi_2Nb_2O_9$ showed that the flux growth method employed was successful in growing the desired phase, and that the single-crystal structure was very close to that based on powder diffraction published previously. The slight discrepancy in the degree of cation mixing between this sample and the previous (and current) powder diffraction data could be a result of the growth process, or the inherent increased resolution in a single crystal measurement, particularly one utilizing MoKα radiation (λ =0.707 Å), when compared to CuKα (λ =1.540 Å).

The single-crystal experiments on $BaBi_2Nb_2O_9$ also confirmed the success of

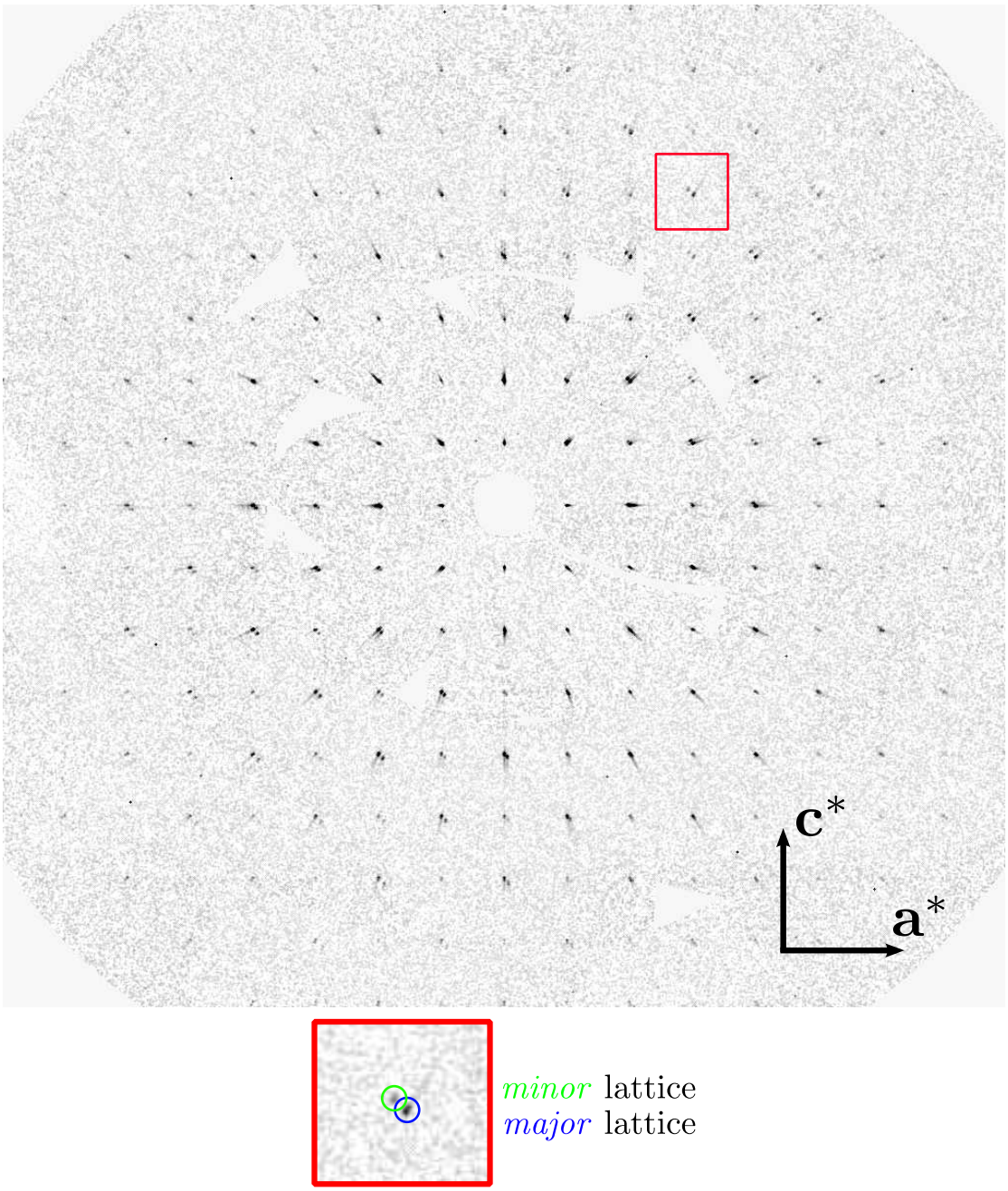

Figure 3-10: Precession image of the $h0l$ reciprocal lattice plane in $BaTiO_3$

the attempted growth of this material. The aim of finally settling the lengthy debate regarding the symmetry of $BaBi_2Nb_2O_9$ was not fully realised, although this work does represent the first single crystal structural study of this material. It was shown that the electron density around the barium site in particular showed some degree of non-ellipsoidal structure, and this was accounted for with anharmonic thermal displacement parameters, despite the fact that the more favoured model was actually one involving a convolution of four polarized, 90° rotated twin components. Attempts at refining this structure using this model were unsuccessful; the substantial overlap of density from the four twin components meant that the refinement process failed. These observations are in keeping with those made on archetypal relaxor ferroelectrics, such as $Pb(Mg_{1/3}Nb_{2/3})O_3$, which describe a difference in the micro- and macroscopic symmetries of the lattice. Critically, no peak splitting that would be indicative of distortion of the crystal from tetragonal lattice symmetry was observed.

The single-crystal experiment on $CsBiNb_2O_7$ showed, for the first time, evidence of diffuse scattering in this material. This disorder, combined with obvious twinning, meant that a conclusive structure solution was very difficult. However, extensive study of Fourier difference maps led to the conclusion that the crystal forms in two enantiomorphs, disordered in the $\boldsymbol{c}$ direction.

The validity of previous assertions that $BaTiO_3$ forms in a monoclinic phase were tested using single-crystal measurements. Unexpected peaks were observed, displaced from a tetragonal lattice, consistent with those used to prove the existence of a monoclinic co-crystal in the literature. However, in the current analysis, it was demonstrated that these peaks were evidence not of a monoclinic phase, but simply of rotational twinning.

References

[1] H. Amorin, R. S. Martins, K. L. Kholkin, and M. E. V. Costa, Ferroelectrics **320**, 45 (2005).

[2] A. Snedden, K. S. Knight, and P. Lightfoot, Journal of Solid State Chemistry **173**, 309 (2003).

[3] R. C. Clark and J. S. Reid, Acta Cryst. **A51**, 887 (1995).

[4] G. Sheldrick, Acta. Cryst. **A64**, 112 (2008).

[5] L. J. Farrugia, J. Appl. Cryst. **32**, 837 (1999).

[6] V. Petricek, M. Dusek, and L. Palatinus, *Jana2006. The crystallographic computing system* (Institute of Physics, Praha, Czech Republic., 2006).

[7] L. Palatinus and G. Chapuis, Journal of Applied Crystallography **40**, 32 (2007).

[8] S. M. Blake, M. J. Falconer, M. McCreedy, and P. Lightfoot, J. Mater. Chem. **7**, 1609 (1997).

[9] A. Snedden, C. H. Hervoches, and P. Lightfoot, Phys. Rev. B **67**, 092102 (2003).

[10] Ismunandar, B. J. Kennedy, Gunawan, and Marsongkohadi, Journal of Solid State Chemistry **126**, 135 (1996).

[11] D. Nuzhnyy, S. Kamba, P. Kuzel, S. Veljko, V. Bovtun, M. Savinov, J. Petzelt, H. Amorin, M. E. V. Costa, A. L. Kholkin, et al., Phys. Rev., B, Condens, Matter Mater. Phys. **74**, 134105 (2006).

[12] R. Z. Hou, X. M. Chen, and Y. W. Zeng, J. Am. Ceram. Soc. **89**, 2839 (2006).

[13] P. Keburis, J. Banys, A. Brilingas, J. Prapuolenis, A. Kholkin, and M. E. V. Costa, J. Nanosci. Nanotechnol. **353**, 149 (2007).

[14] N. de Mathan, E. Husson, G. Calvarn, J. R. Gavarri, A. W. Hewat, and A. Morell, J. Phys., Condens. Matter. **3**, 8159 (1991).

[15] Y. Shimakawa, Y. Kubo, Y. Nakagawa, S. Goto, T. Kamiyama, H. Asano, and F. Izumi, Phys. Rev. B **61**, 6559 (2000).

[16] R. Macquart, B. J. Kennedy, T. Vogt, and C. J. Howard, Phys. Rev, B, Condens, Matter Mater. Phys. (USA) **66**, 212102 (2002).

[17] R. Clarke, J. Appl. Crystallogr. **9**, 335 (1976).

[18] A. Kojima, H. Sasou, K. Tozaki, T. Okazaki, Y. Yoshimura, N. Tokunaga, and H. Iwasaki, Int. J. Thermophys. **26**, 1963 (2005).

[19] Y. Yoshimura, A. Kojima, N. Tokunaga, K. Tozaki, and T. Koganezawa, Phys. Lett. A **353**, 250 (2006).

[20] Y. Yoshimura, M. Morioka, A. Kojima, N. Tokunaga, T. Koganezawa, and K. Tozaki, Phys. Lett. A (Netherlands) **367**, 394 (2007).

[21] H. Cao, C. P. Devreugd, W. Ge, J. Li, D. Viehland, H. Luo, and X. Zhao, Appl. Phys. Lett. **94**, 032901 (2009).

[22] D. S. Keeble and P. A. Thomas, J. Appl. Cryst. **42**, 480 (2009).

Chapter 4

Birefringence Studies

Preface

This chapter deals with optical experiments performed on single crystals, particularly studying the birefringence of materials as a function of temperature. Such measurements allow the plotting of the value of the birefringence in a given sample across any phase transitions that may occur, allowing the nature of that phase transition to be probed.

4.1 Experimental Details

Birefringence microscopy was performed on single-crystal samples using an Oxford Cryosystems "Metripol" birefringence imaging system. This was linked to a Nikon Eclipse E400 Pol microscope, with a x4 objective and a working distance of 30 mm. For the measurements themselves 10 steps of the rotating polariser were used. A 550 nm filter was chosen for all the experiments, to match best the colour of the crystal in order to optimise the transmitted intensity. For measurements at non-ambient temperatures, the sample was placed in a Linkam 600 furnace in air. Initially, a series of measurements at varying temperatures were taken without a sample to ensure the furnace windows contributed no birefringence to the overall signal. For all experiments, to ensure thermal equilibrium within the sample, a relatively slow heating rate of $1\,\mathrm{K\,min^{-1}}$ was utilised.

4.2 $SrBi_2Ta_2O_9$

As discussed in the literature review (§1.3), $SrBi_2Ta_2O_9$ undergoes two phase transitions; one ferroelastic and one ferroelectric. As the two effects of strain

and polarization that make up this two-stage transition both have a resulting contribution to the birefringence, it should be possible to confirm or refute such a hypothesis using birefringence imaging. Birefringence studies of $SrBi_2Ta_2O_9$ were performed on a small, as-grown single crystal retrieved directly from the melt. The crystal dimensions were $500\,\mu m^2 \times 20\,\mu m$. False colour images of the birefringence of the crystal of $SrBi_2Ta_2O_9$ can be seen in figure 4-1. It is apparent from these images that there are no striations associated with ferroelastic (or ferroelectric) domains present in this sample, which contradicts the observations of Kamba et al. [1]. The fringes that do occur are consistent with those arising from a slight deviation in the thickness of the sample, an observation that is in keeping with the use of "as-grown" crystals that have not been polished to ensure parallelism of the faces.

A distinct slowing of the rate of movement of the fringes is noticed as the crystal approaches the zero-birefringence high-temperature phase. This is also demonstrated in the plot of $|\sin\delta|$, which is shown in figure 4-2. This figure also shows the birefringence that would be "expected" from a single phase transition, *i.e.*, a phase transition with a regular increase in the rate of the fringes with temperature. Following the method laid out in figure 2-8, values of δ were manually assigned to the individual fringes in this graph. The relevant mathematical formulae were then applied to the data, to yield a graph of the birefringence, Δn. This graph is shown in figure 4-3. This shows categorically two distinct phase transitions. Going down in temperature, the first, at temperature T_{c1}, is from a region of zero birefringence to a region wherein the birefringence is roughly linear with decreasing temperature. The second, at T_{c2} is from this region to one wherein the relationship becomes non-linear. To find the exact relationship between temperature and Δn in these regions, the critical exponents must be found. It is a well-known mathematical device to reveal a power law relationship by taking the natural logarithm of both the x and y axes, and the exponent is revealed in the gradient. If the resulting line is not straight, then the relationship is not a power law of single exponent. To this end a plot of the natural log of the birefringence against the natural log of the temperature difference from T_c is graphed (a $\ln - \ln$ plot). The gradient of such a graph will give the critical exponent in that area.

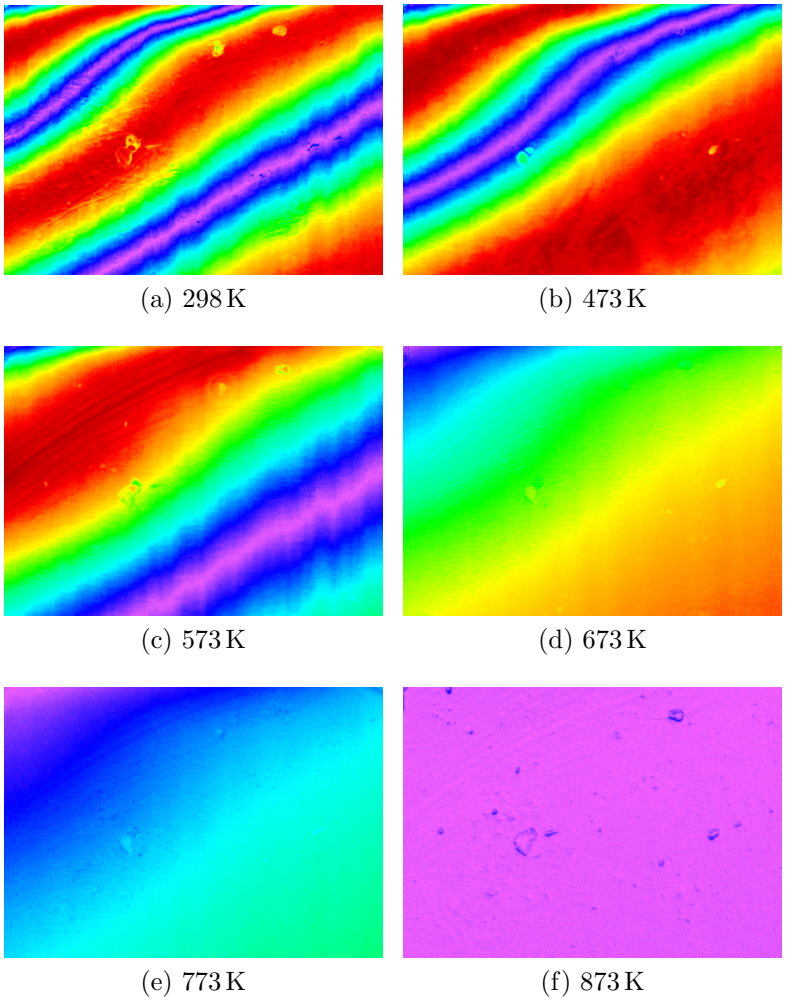

(a) 298 K (b) 473 K

(c) 573 K (d) 673 K

(e) 773 K (f) 873 K

Figure 4-1: False colour images of the birefringence of $SrBi_2Ta_2O_9$ through the phase transition, at temperatures of: 298 K (a); 473 K (b); 573 K (c); 673 K (d); 773 K (e); and, 873 K (f).

Firstly, the behaviour between T_{c1} and T_{c2} is analysed, and the ln – ln plot for this region is shown in figure 4-4. Since the critical exponent and the transition temperature are interdependent, the choice of temperature for T_{c1} effects the results of the linear fitting procedure. For this reason, the method adapted by Geday and Glazer [2] was followed. The coefficient of determination (R^2) for the linear regression was plotted for a range of T_{c1}. The value of T_{c1} which yielded the highest R^2 was deemed to be correct, and it was from this that the value of β' was measured. The data from this procedure is shown in figure 4-5. The gradient of the line, and hence the critical exponent in this region, is 1.054±0.03 for the T_{c1} with the highest R^2, 848K, indicating an almost perfect linear relationship. This is consistent with the prediction that the transition at T_{c1} is ferroelastic.

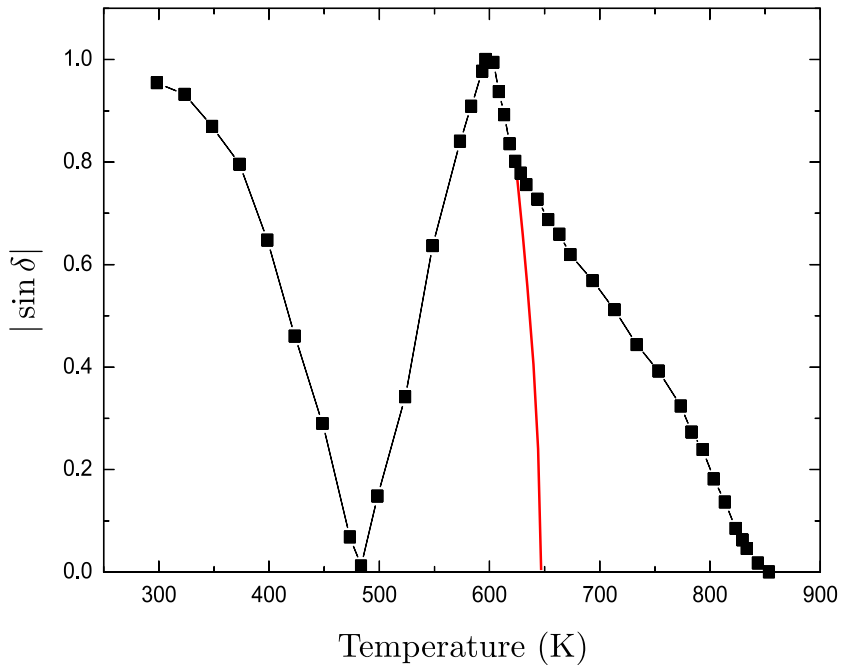

Figure 4-2: The variation of $|\sin\delta|$ in $SrBi_2Ta_2O_9$ with temperature. The red line demonstrates what would be expected from a single, second order phase transition.

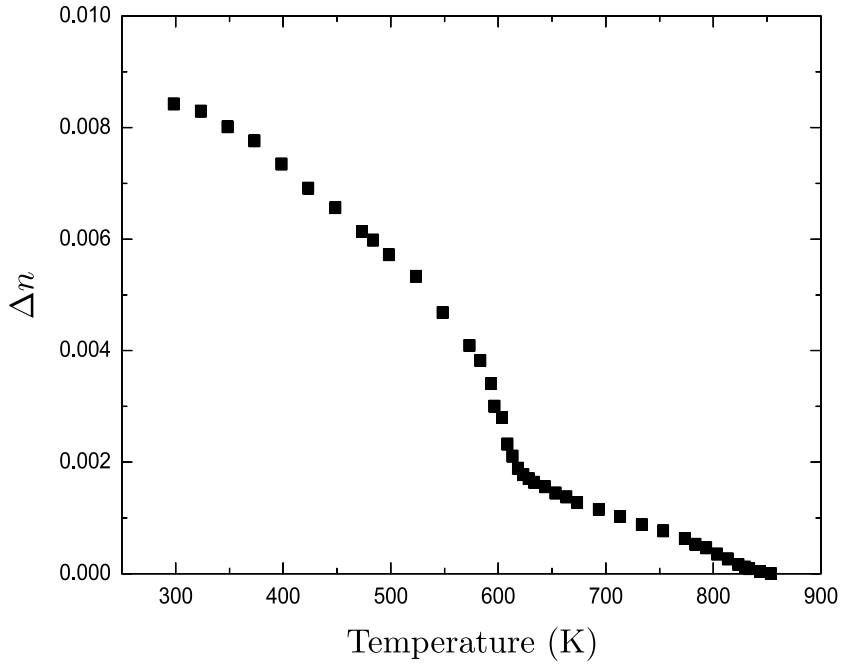

Figure 4-3: The variation of Δn, the birefringence, with temperature in $SrBi_2Ta_2O_9$.

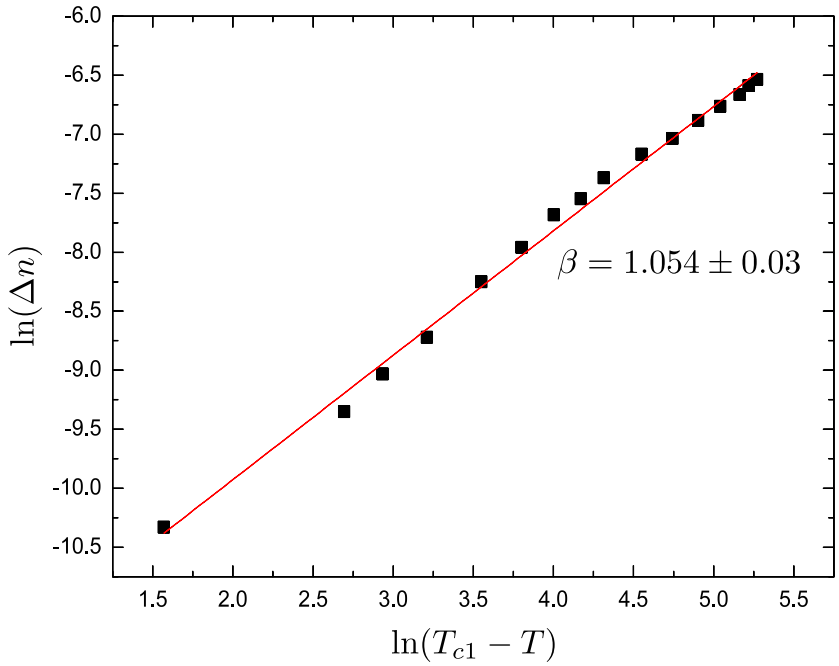

Figure 4-4: Plot of $\ln(T_{c1} - T)$ against $\ln(\Delta n)$ for $SrBi_2Ta_2O_9$ in the intermediate region, with T_{c1} =848 K.

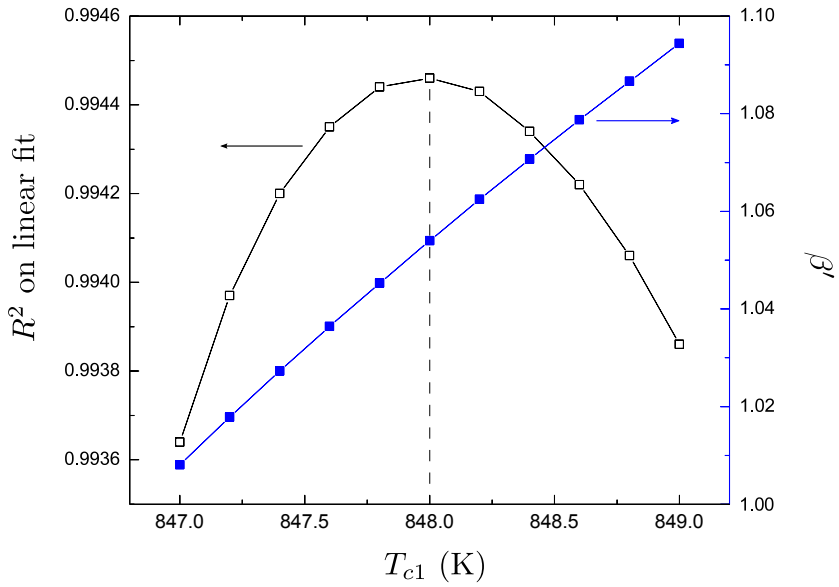

Figure 4-5: R^2 of linear fit of $\ln(T_{c1} - T)$ against $\ln(\Delta n)$ as a function of T_{c1} for $SrBi_2Ta_2O_9$.

Treatment of the second transition (from the intermediate to the low temperature region) is more complex, however. The deconvolution of the already present strain contribution from the contribution from the second transition is very dependent on the choice of transition temperature. In contrast to the higher temperature, however, a simple application of a coefficient of determination test is not conclusive in this instance as there exists data above T_{c2}. In a ln – ln plot, these data points are complex, and hence the choice of T_{c2} affects not only the critical exponent, but the number of data points that contribute to the fitting procedure. The equation used for this analysis, as implemented in the linear regression feature of Microsoft Excel, is a normalised sum of differences, and is dependent on the number of data points used. For this reason, a modified standard deviation was used as a quality of fit measure for this transition. However, since this strain, and hence the resulting birefringence, are still present below T_{c2}, a correction needs to be made to the values of Δn in this region. Two different corrections were tested on the second transition to accommodate this residual birefringence. For the first correction, the birefringence was assumed to continue to rise linearly with decreasing temperature. In the second case, the residual birefringence is assumed to remain at the level shown at T_{c2}. The plots of the birefringence over the total temperature range with these corrections is shown in figure 4-6. These three data sets demonstrate clearly the dramatic effect the choice of correction has on the temperature dependence of the birefringence below T_{c2}. However, both the linear and constant corrections do achieve the goal of reducing the birefringence to zero at the lower transition, thus eliminating the already-present strain contribution.

The linear correction involved fitting the birefringence between T_{c1} and T_{c2} with a linear trend line, extrapolating the line to lower temperatures, and subtracting from the measured birefringence. A range of possible T_{c2} were applied to the data, yielding a range of ln – ln plots. Following the method from above, the gradients and figure of merits for these linear fits were graphed, in figure 4-7, to reveal the values of T_{c2} and β'. Inspection of these results reveals a T_{c2} of 608 K±1 K, and a β' of 0.38±0.08. The constant correction was applied by fitting a high order polynomial to the data around T_{c2}, which was then used to interpolate a value of Δn for any specific temperature. This meant that for any choice of T_{c2}, the

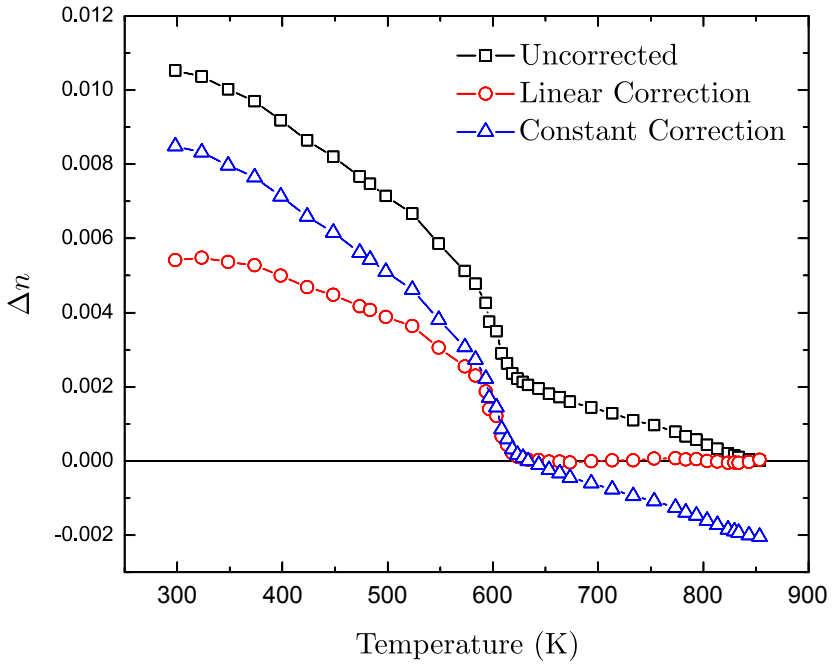

Figure 4-6: Three plots of the birefringence as a function of temperature in $SrBi_2Ta_2O_9$, the uncorrected data, data corrected linearly, and data corrected with a constant.

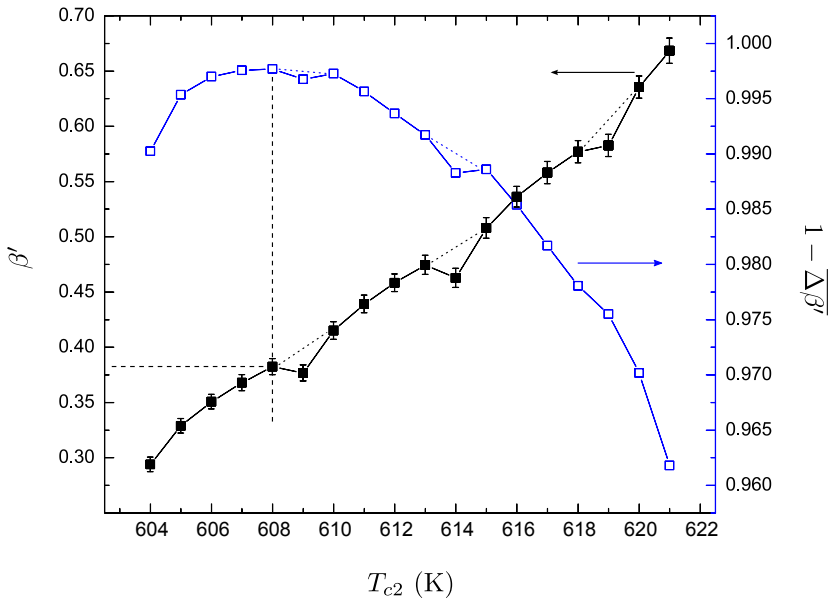

Figure 4-7: Graph showing the testing of various transition temperatures T_{c2} for $SrBi_2Ta_2O_9$.

corresponding value of Δn could be calculated, and then subtracted from all values of the birefringence. The figure of merits for the linear fits of the range of ln – ln plots yielded a T_{c2} of 605 K±1 K and a β' of 0.64±0.02.

This result shows that the choice of correction applied to the data does not affect the observed transition temperature, to within error, as both methods suggest a T_{c2} of 608 K±1 K. The value of β', however, does differ; 0.38±0.08 using the linear correction and 0.64±0.02 using the constant correction. This suggests that, in fact, the birefringence resulting from the strain, and hence, the strain, continue to rise as the crystal is cooled below T_{c2}, through the ferroelectric phase.

4.3 $SrBi_2Nb_2O_9$

The room-temperature false-colour image of the birefringence of $SrBi_2Nb_2O_9$ can be seen in figure 4-8. In the piece of crystal in this figure there are areas of differing crystal quality. The area on the left (area A) is of poor quality for the purposes of birefringence microscopy, due the superposition of the main piece of the crystal and a second piece, of a different crystal orientation, that has grown on the main piece. There is also strain in this area that is associated with this effect. The area on the right (area B) of the crystal is demonstrative of a good piece of crystal for use in birefringence microscopy, with the exception of areas at the crystal edges, as here local strain appears to dominate the birefringence. Like the piece of crystal used for the investigation of $SrBi_2Ta_2O_9$, this piece shows fringes suggestive of an inhomogeneous thickness across the sample, with some significant thickness effect occurring along line C in figure 4-8. The direction of movement of the fringes suggests that C is a line of maximum thickness in the sample. Figure 4-9 shows the false-colour birefringence of $SrBi_2Nb_2O_9$ as a function of temperature.

It has recently been reported by Shimakawa et al. [3] that the Curie temperature, T_c, of $SrBi_2Nb_2O_9$ is 713 K. The analysis software allows for the variation in phase retardation, δ, with temperature, to be derived. Some manual manipulation of the raw output is needed, however, as this method of birefringence microscopy is capable of measuring $|\sin\delta|$ only. The order of the fringes needs to be assigned by hand, so that the value of the phase retardation, δ, can be obtained. The

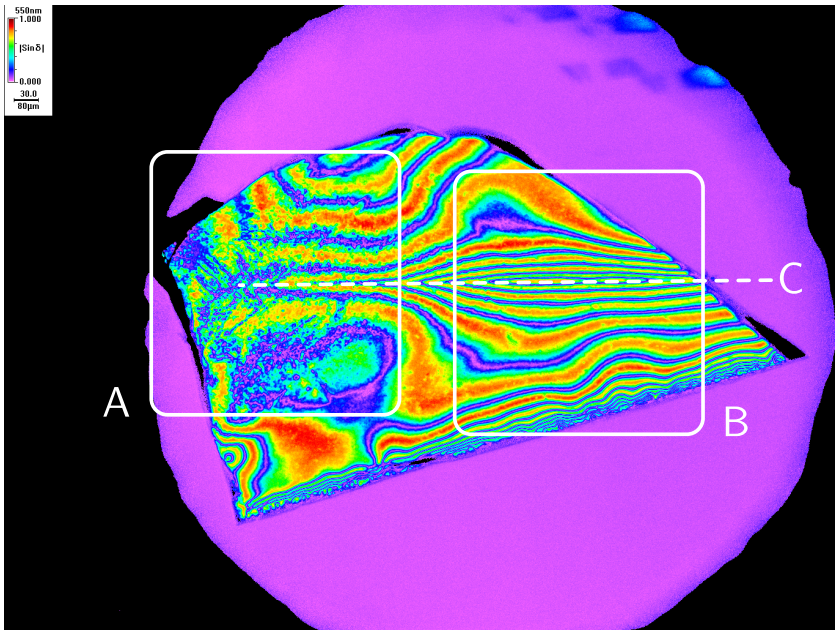

Figure 4-8: Room temperature false colour birefringence image of $SrBi_2Nb_2O_9$.

automated output of $|\sin\delta|$ for $SrBi_2Nb_2O_9$ can be seen in figure 4-10. To remove the modulus and the sin the maxima of the plot can be assigned values, in order from high to low temperature, of $\pi/2$, $3\pi/2$, $5\pi/2$, $\ldots(2n-1)\pi/2$, and similarly the minima 0, π, 2π, 3π, $\ldots(n-1)\pi$. This assignment allows the plotting of the phase retardation, δ, versus temperature, and from this a plot of Δn, the birefringence, can be plotted. The graph of Δn for $SrBi_2Nb_2O_9$ is shown in figure 4-11. As discussed in §1.2, Landau theory provides a model of phase transitions that can relate an order parameter to the group-subgroup relations of the transition. Under the assumption that all of the birefringence measured is due to a spontaneous polarization that appears at the critical temperature T_c, then one can denote the phase retardation as a Landau order parameter. This allows for the critical exponent, β, of the transition to be established. Figure 4-12 shows the $\ln-\ln$ relationship, which curiously does not show a uniform gradient that would indicate a single critical exponent. This suggests, therefore, that there is also a contribution to the birefringence from another effect, the most likely source being strain. As an otherwise isotropic structure or unit cell is strained, optical anisotropy is introduced. It is possible to discern birefringence arising from these two differing effects, however, as birefringence is linear in strain and quadratic in

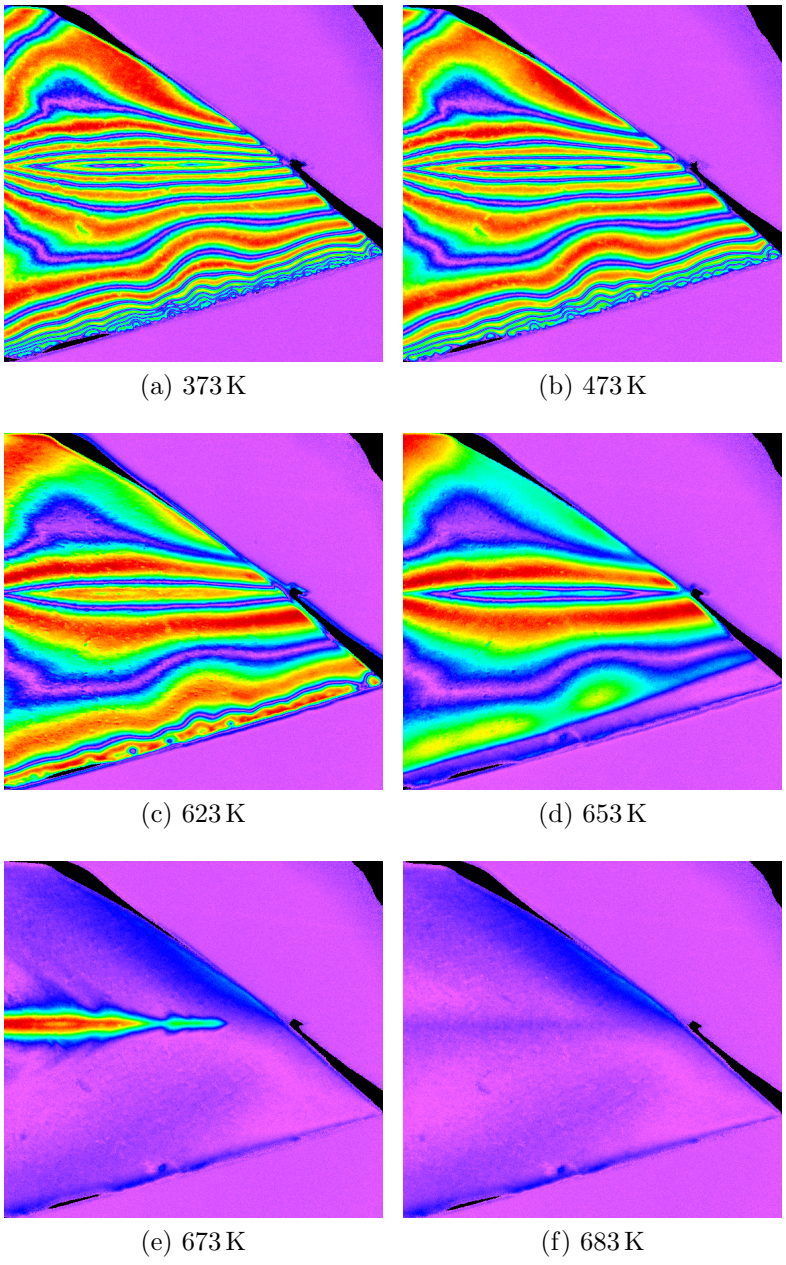

(a) 373 K (b) 473 K

(c) 623 K (d) 653 K

(e) 673 K (f) 683 K

Figure 4-9: False colour images of the birefringence of $SrBi_2Nb_2O_9$ through the phase transition, at temperatures of: 373 K (a); 473 K (b); 623 K (c); 653 K (d); 673 K (e); and, 683 K (f).

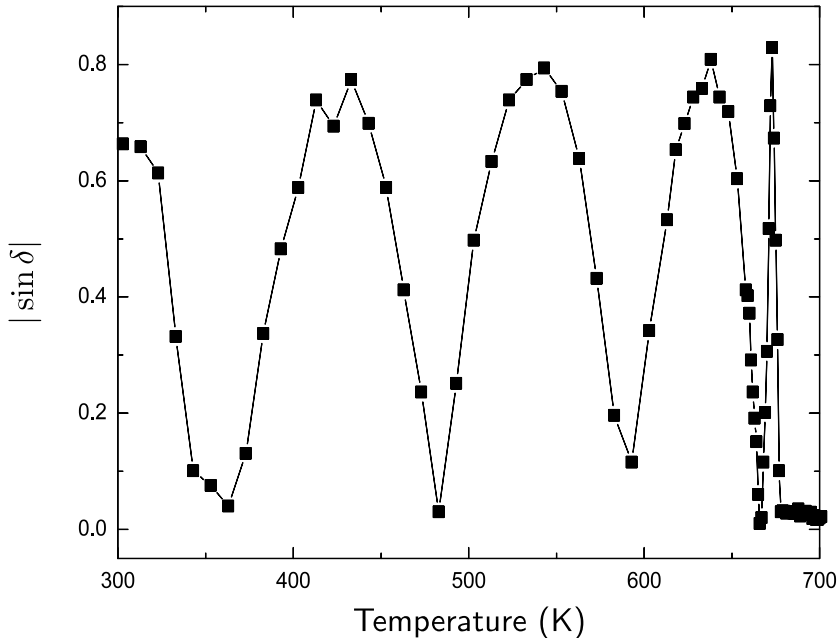

Figure 4-10: The variation of $|\sin\delta|$ in $SrBi_2Nb_2O_9$with temperature.

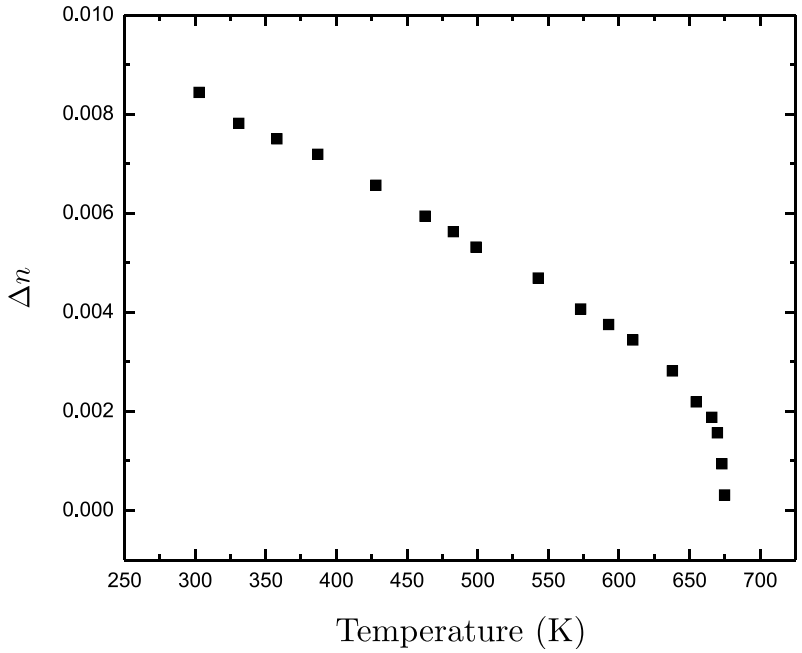

Figure 4-11: The variation of the birefringence, Δn, with temperature in $SrBi_2Nb_2O_9$

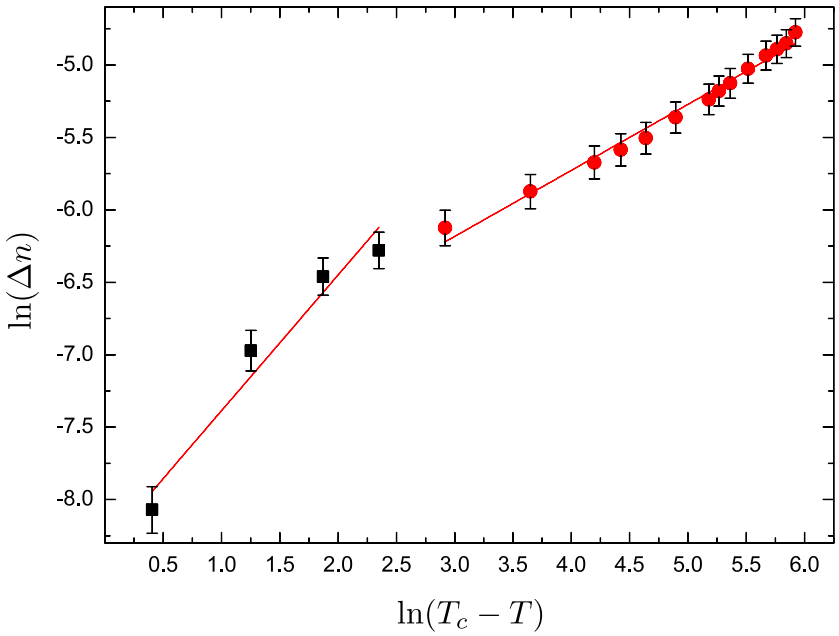

Figure 4-12: Plot of $\ln(T_c - T)$ against $\ln(\Delta n)$ for $SrBi_2Nb_2O_9$. The plot is divided into two distinct regions of gradient.

polarization (see §1.2). Separating figure 4-12 into two distinct regions, that near the transition (low $\ln(T_c - T)$), and that far from it (high $\ln(T_c - T)$) gives two areas that are roughly linear, and hence of a constant critical exponent β. This suggests that there are, in fact, two distinct phase transitions occurring at differing temperatures in this region. A more in depth study of the critical exponents for these regions was performed to analyse the transitions further. The two distinct regions can be seen in figure 4-12, and the critical exponents elucidated for the two regions are:

$$\beta = \begin{cases} 0.9372 & \text{For } \ln(T_c - T) < 2.5, \\ 0.4262 & \text{Otherwise.} \end{cases} \tag{4-1}$$

Although it can be said that each of these regions is dominated by one of the two effects, the other is still present and this serves to move the plot away from two distinct straight lines and toward a curve. From the known dependence of δ on strain and polarization (see §2.3), we can assign one of each of these origins of birefringence to be dominant in each of the two areas. From §2.3 we know that, for a crystal exhibiting birefringence as a combined result of polarization and strain;

$$\Delta n = n_e - n_o = k_1 P_s^2 + k_2 \epsilon \tag{4-2}$$

and so the critical exponent of an area dominated by polarization will be half of that directly measured. In the case of $SrBi_2Nb_2O_9$ it can therefore be deduced that the region close to the phase transition ($\ln(T_c - T) < 2.5$) is dominated by the contribution of the spontaneous polarization in the ferroelectric phase.

4.4 $BaBi_2Nb_2O_9$

Birefringence microscopy was performed on an as grown, small, thin, platelet shaped crystal of $BaBi_2Nb_2O_9$. The false colour image of $|\sin\delta|$ can be seen in figure 4-13. This image shows zero birefringence across the whole sample, and this value is maintained throughout the temperature range across T_c.

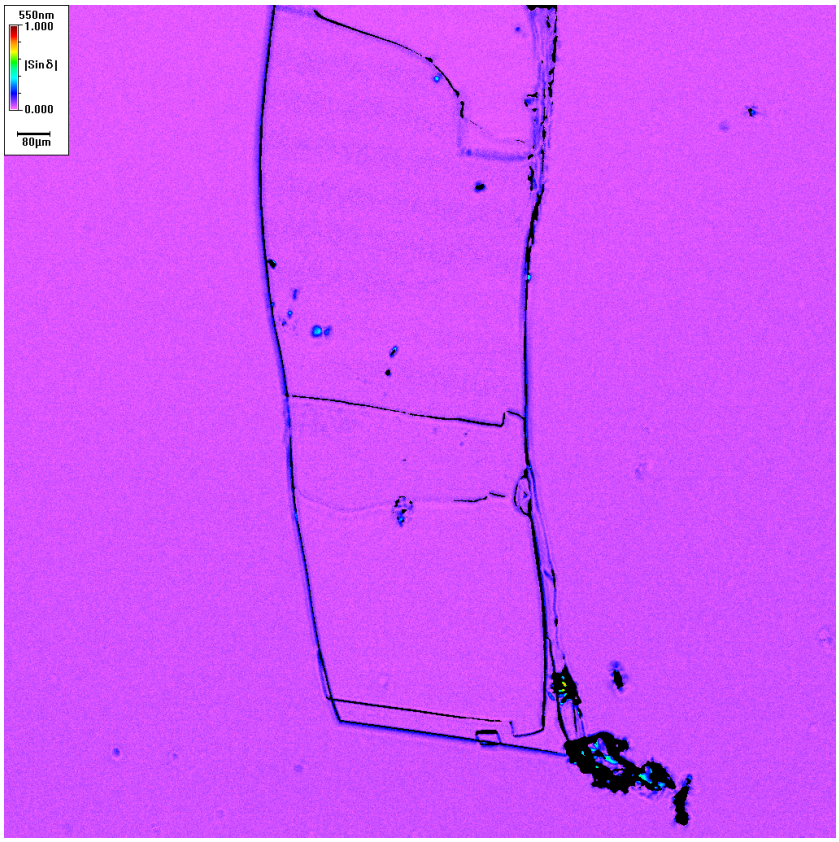

Figure 4-13: False colour image of $|\sin\delta|$ in $BaBi_2Nb_2O_9$ at room temperature

4.5 $SrBi_2Nb_{1.5}Ta_{0.5}O_9$

$SrBi_2Nb_{1.5}Ta_{0.5}O_9$ exhibits very similar behaviour to $SrBi_2Ta_2O_9$ in that there exists a high temperature region where the birefringence falls at a relatively slow, linear rate. Figure 4-14 shows the birefringence for this material as a function of temperature.

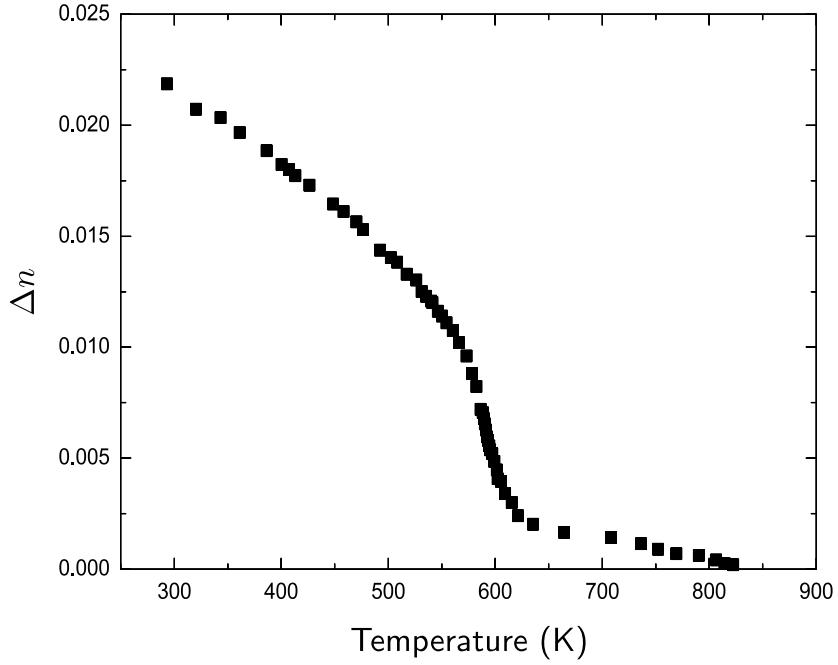

Figure 4-14: Plot of Δn, the birefringence, for $SrBi_2Nb_{1.5}Ta_{0.5}O_9$

Inspection of this graph shows us that the substitution of tantalum into the structure of $SrBi_2Nb_2O_9$ introduces the ferroelastic transition at a higher temperature as seen in the end member $SrBi_2Ta_2O_9$. Also observed is a higher room-temperature value of the birefringence than that which is seen in either of the end members, although this may be a result of incorrect sample thickness determination. If we treat this data in a fashion identical to that which was used for $SrBi_2Ta_2O_9$, a T_{c1} of 570 K, and a T_{c2} of 328 K are observed. These temperatures are 5 K and 20 K lower than those seen in $SrBi_2Ta_2O_9$, and the measured critical exponents are 1.03(4) for the transition at higher temperature, and 0.46(5) (constant-corrected) and 0.40(3) (linearly-corrected).

4.6 Birefringence Conclusions

The optical study of single crystals has been used to complement structural measurements, and, in certain cases, improve the understanding of diffraction experiments. The birefringence of $SrBi_2Ta_2O_9$ showed that two phase transitions can easily be observed, and that the nature of the phase transition can also be ascertained from the birefringence data. Several different methods of treating the data were employed to best fit the known structural transitions that occur, and it was found that fitting the birefringence above the lower T_c with a linear function, and subtracting the extrapolation to lower temperatures, resulted in the best fit of the lower temperature data. However, it was also noted that it appeared that the strain did not rise at this rate over the whole region, rather at some unknown, lower rate.

The experiments on $SrBi_2Nb_2O_9$ appear to show a pseudo-first order phase transition. Of course, the actual measurement of data points in the vertical region (at ~675 K) is not possible, so instead this is treated as a pseudo-double transition, as seen in $SrBi_2Ta_2O_9$. However, rather than being two distinct transitions, a single, "two-step" transition is observed, with there being an area dominated by one effect very close to T_c, and another region taking dominance as the temperature is lowered further. Additional analysis reveals that it appears the temperature region very close to T_c is dominated by polarization, and the region far from T_c is dominated by changes in strain. The implication of this is that there is a very sharp distortion of the prototypic structure near to T_c, which leads to the macroscopic polarization, and then this polarization remains relatively unchanged over the remainder of the temperature region studied.

Birefringence measurements on a single crystal of $BaBi_2Nb_2O_9$ confirm that the structure is macroscopically, and metrically, tetragonal, as no birefringence resulting from isotropy in the plane of the crystal can be observed. Therefore, the optical indicatrix is uniaxial to within 1 part in 10^7.

The substitution of Ta onto the Nb site in $SrBi_2Nb_2O_9$ introduces the distinct two-stage phase transition, as observed in $SrBi_2Ta_2O_9$. The temperature dependant birefringence behaviour is very similar, although the phase transition temperatures are slightly lower than in the tantalate end-member. An interesting

further investigation would be to look at very small Ta dopant levels, to reveal the compositionally driven introduction of the high temperature ferroelastic phase transition.

References

[1] S. Kamba, J. Pokorny, V. Porokhonskyy, J. Petzelt, M. P. Moret, A. Garg, Z. H. Barber, and R. Zallen, Applied Physics Letters **81**, 1056 (2002).

[2] M. A. Geday and A. M. Glazer, J. Phys., Condens. Matter **16**, 3303 (2004).

[3] Y. Shimakawa, Y. Kubo, Y. Tauchi, T. Kamiyama, H. Asano, and F. Izumi, Applied Physics Letters **77**, 2749 (2000).

Chapter 5

Structural Studies of Powder Aurivillius Phases

Preface

Knowledge of the crystal structure of a material is fundamental in the understanding of the properties it exhibits. The point group symmetry determines the allowed physical properties, whereas the atomic arrangement within the structure directly influences the magnitude of such properties, so ascertaining structure is of paramount importance. This chapter describes the determination of the structure of some Aurivillius phases, ascertained by x-ray diffraction. Both powder and single-crystal diffraction is used in this study, as each has its own advantages. Powder diffraction is particularly suited to non-ambient measurements, and for solving the structures of sub–cells in materials which have a long range super–structure. Single-crystal diffraction, however, has the advantage that orientation data is not lost, and so superstructures and twins can be observed and solved. Single-crystal diffraction also yields more accurate estimations of the symmetry because it gives 3-dimensional data without the problem of peak overlap, and of the crystal structure. It is, however, much more dependent on sample quality so good preparation is of the highest importance.

5.1 Ceramic Sample Preparation

Ceramic samples were all synthesized *via* the solid state reaction method from mixed oxides and carbonates. Stoichiometric quantities of the desired materials were weighed, and then mixed together in isopropanol. Sialon milling media were then added to the oxide suspension, and the cylindrical milling vessel was left

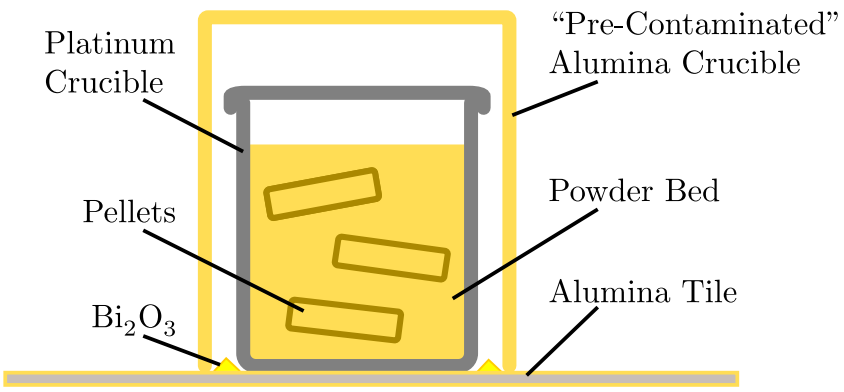

Figure 5-1: Schematic of the double crucible arrangement used in calcination and sintering of ceramic samples

to rotate at approximately 1 Hz for 24 hours, to ensure thorough mixing of the constituents. The suspension was then transferred to a crystallisation dish and left to settle. The excess isopropanol was then removed *via* syringe, ensuring that all the powder remained in the dish. The dish was then left in a drying oven at 60°C, until all the remaining isopropanol had evaporated. A proportion of the mixed powder was pressed into 5 mm thick cylindrical pellets of 12 mm diameter in an isostatic uniaxial press. The remaining loose powder was then used as a powder bed into which the pressed pellets were buried, in a platinum crucible. It was found that a typical 25 ml crucible held no more than three of these pellets. The crucibles were sealed with platinum lids, and placed inside a secondary, upturned alumina crucible, and placed on an alumina tile. Both alumina components were pre-impregnated with bismuth by heating to 900°C in air in the presence of Bi_2O_3. This *double crucible* method was employed to reduce bismuth loss during the sample heating processes. A diagram showing the crucible arrangement can be seen in figure 5-1. Once calcined, the pellets were ground with an agate pestle and mortar and checked for phase purity using x-ray diffraction, using a PANalytical MPD diffractometer. The powder was then repressed into pellets, reburied in the powder bed, and sintered to increase density. The sintered powders were again checked for phase purity *via* x-ray diffraction, and the composition was confirmed using energy dispersive x-ray spectroscopy in a variable pressure Zeiss Supra 55VP scanning electron microscope. The use of variable pressure EDX in this case removed the need to sputter coat the sample

Table 5-1: The calcination and sintering temperatures for the ceramics used in this study.

Composition	Calcination (°C)	Sintering (°C)	Melting Point
$SrBi_2Nb_2O_9$[1]	700	900/1000	1335
$BaBi_2Nb_2O_9$[1]	700	1000/1000	1142
$CsBiNb_2O_7$[2]	1000	–	<1000

and hence any ambiguity from the analysis resulting from the emission lines of the coating material overlapping with those of the sample *i.e.* Nb $L\alpha_1$ = 2.165 keV cf. Au $M\alpha_1$ = 2.122 keV. The calcination and sintering temperatures for the various materials synthesized in this study are given in table 5-1.

All of the powders synthesized using this method formed as mustard-coloured powder of high density which were relatively difficult to grind in a standard pestle and mortar. To reduce the volume of sample lost from under the pestle due to the high hardness of the sample, an adapted mortar with a sample confinement membrane was used. A thorough grinding typically took 30 minutes.

Fluorinated Aurivillius Structures

The fluorinated samples were synthesised by Dr. Richard Goff at the University of St. Andrews. The $Bi_2W_{1-x}Nb_xO_{6-x}F_x$ solid solution was prepared at 900°C in air using the appropriate stoichiometric ratio of Bi_2O_3, BiF_3, WO_3 and Nb_2O_5. The mixture was heated for 2 days, reground, then heated for another 3 days. $Sr_{1+x}Bi_{2-x}Nb_2O_{9-x}F_x$ and $Ba_{1+x}Bi_{2-x}Nb_2O_{9-x}F_x$ were prepared using a stoichiometric mixture of $SrCO_3$ or $BaCO_3$, BiF_3, Bi_2O_3 and Nb_2O_5. The strontium based phases were heated at 900°C for 2 days, reground, then heated for another 3 days. The barium based phases were heated at 1000°C for two days, then reground and heated for another 3 days twice.

5.2 Experimental Details

X-ray powder diffraction was performed in-house on a PANalytical X'Pert Pro MPD diffractometer, in θ–2θ Bragg-Brantano geometry. Monochromatic CuKα_1

from a germanium curved-Johansson focussing monochromator was used in all cases to remove the inherent loss of resolution associated with the use of CuK$\alpha_{1,2}$. For measurements at non ambient temperature an Anton Paar HTK1200N furnace was used with an atmosphere of air. An automatic stage height adjustment system was employed to reduce the effect of thermal expansion of the furnace on the diffraction pattern. A PANalytical PIXcel detector, with an active length of 3.47° (at a detector distance of 120 mm), split into 255 channels was used in all measurements. The PIXcel detector has excellent combined linearity and sensitivity, leading to relatively quick scans being of sufficient quality for reliable Rietveld analysis.

Rietveld analysis was performed using the software package Topas Academic. For all powder refinements isotropic thermal parameters were used for the oxygen and anisotropic thermal parameters were used on the cations, except where explicitly expressed in the text. Detector zero error and sample height error corrections were always allowed to refine, and the LP-factor and axial divergence corrections were applied but constrained to theoretical values. The peak shape function used in all refinements was the modified Thompson–Cox–Hastings pseudo–Voigt (TCHZ), as described in §2.1.

5.3 Powder diffraction of $SrBi_2Nb_2O_9$

Powder x-ray diffraction was performed on $SrBi_2Nb_2O_9$, and the collected pattern and the final Rietveld refinement are shown in figure 5-2. The powder was packed into a stainless steel sample holder, containing a 16 mm diameter and 2.33 mm deep circular disc of powder. The sample was spun throughout the data collection with a revolution time of 8 s, significantly less that the counting time per step of 1500 s, so that orientations were effectively averaged. A 10 mm beam mask was used in conjunction with a 1/2° divergence slit, and 0.02 radian Soller slits were used in the diffracted beam optics.

The details of the Rietveld refinement represented in figure 5-2 are summarised in table 5-2. A Pawley refinement on the 20 peaks of highest d-spacing, performed in Topas Academic, revealed the most likely space group to be $Cmc2_1$. Blake et al.

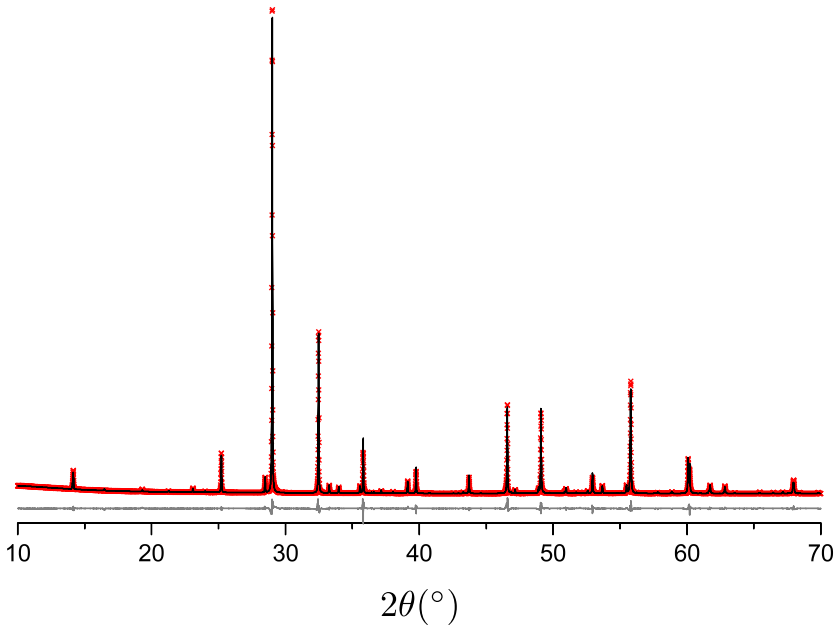

Figure 5-2: Powder diffraction pattern (×), final Rietveld refinement (—), and difference plot (—) for $SrBi_2Nb_2O_9$at room temperature

[1] had previously asserted that the space group was $A2_1am$, a non standard setting of $Cmc2_1$. This setting is used when studying this family of Aurivillius materials to maintain the ***c***-axis as the long, stacking direction of the cell, rather than the ***b***-axis as is the case in the standard setting. In this study, to maintain consistency with the literature, the "traditional" setting of $A2_1am$ is used. It was also noted by Blake et al. [1] that there was substantial ($\sim 25\%$) cation mixing between the Sr and Bi sites. This was added to the present refinement, but constrained to maintain charge balance and stoichiometry.

A representation of the unit cell as refined from the powder data is shown below, and compared to the high temperature data. It shows how the oxygen octahedra are tilted and distorted, and shows the off-centrality of the niobium from the centre of the octahedra.

Variable Temperature Powder Diffraction

Powder diffraction was performed at a range of temperatures around and above the orthorhombic to tetragonal phase transition at around 713 K [3]. In the work by Snedden et al. [4] a variable temperature neutron diffraction study was performed,

Table 5-2: Rietveld refinement details for powder diffraction of $SrBi_2Nb_2O_9$at ambient temperature

Crystal System	Orthorhombic
Temperature	298 K
Space Group	$A2_1am$
a	5.51417(7)
b	5.51275(7)
c	25.06960(15)
Volume	762.10(1)
Measurement Range	$10^\circ - 70^\circ$ 2θ
Radiation	CuKα_1
Parameters	47
R_p	6.459
wR_p	10.471
gof	4.923
r_{bragg}	3.376

with a temperature step of 50 K between measurements. In this study, powder diffraction patterns were taken every 2 K over the phase transition to gain as much information as possible about the structure and symmetry changes in this region. These data collections were supplemented by longer, higher resolution scans (termed here as *major* scans) at some significant temperatures to ensure the continued validity of the refinements.

For variable-temperature runs the sample was packed into a 16mm inner diameter, 0.8 mm deep alumina sample holder. This was placed in an Anton Paar HTK1200N sample oven on the above-mentioned PANalytical MPD. For all experiments at non-ambient temperatures, a heating rate of $1\,K\,min^{-1}$ was employed, and once the desired temperature was achieved the chamber was left for a 30 minute equilibriation period to ensure a homogeneous temperature distribution. The same optics were used as in the room temperature measurements. The *major* scans used a longer counting time per step, and went to 2θ =107°. These measurements were taken with the aim of being easily soluable, the results of which would be used as the basis for the refinement of shorter patterns taken at similar temperatures. The *major* patterns are shown in figure 5-3, with the region of 36° - 39° 2θ enlarged in figure 5-4. These figures demonstrate the subtlety of the changes to the powder diffraction pattern through the phase transition. The

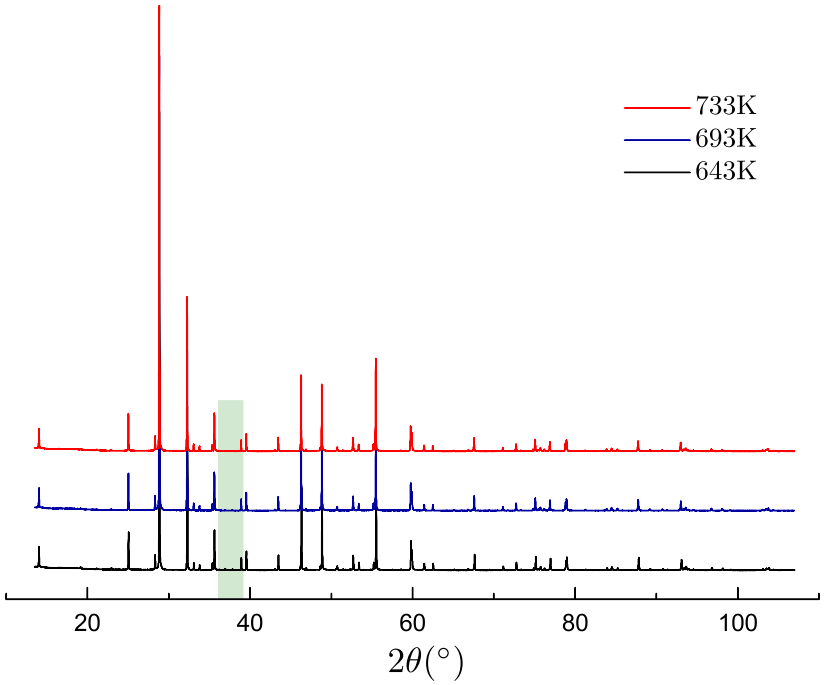

Figure 5-3: Comparison of the powder diffraction pattern of $SrBi_2Nb_2O_9$at 643 K, 693 K and 733 K. The area in green is enlarged in figure 5-4.

subtlety of the phase transition is made clear by these patterns — the difference is almost negligible. This increases the difficulty of the refinement, since the symmetry breaking peaks are so small the failure to model them results in a very small change in the wR_p. For example, refining the *major* 703 K pattern, in which the symmetry breaking peaks are visible (albeit less than 0.1% of the intensity of the strongest peak) in $I4/mmm$ yields a wR_p of 11.594, which is actually less than the corresponding wR_p of 11.609 for $A2_1am$. The Rietveld refinement was perfomed on the *major* patterns initially, the results of which are given in tables 5-3 and 5-4. It should be noted that the cell is metrically tetragonal at these temperatures, and attempts to refine the orthorhombicity, even on the data taken to 107° 2θ, were in vain. For this reason the cell was constrained to be tetragonal (*i.e.* $\boldsymbol{a}$=$\boldsymbol{b}$) for patterns collected above 370 K but the orthorhombic space group was still applied.

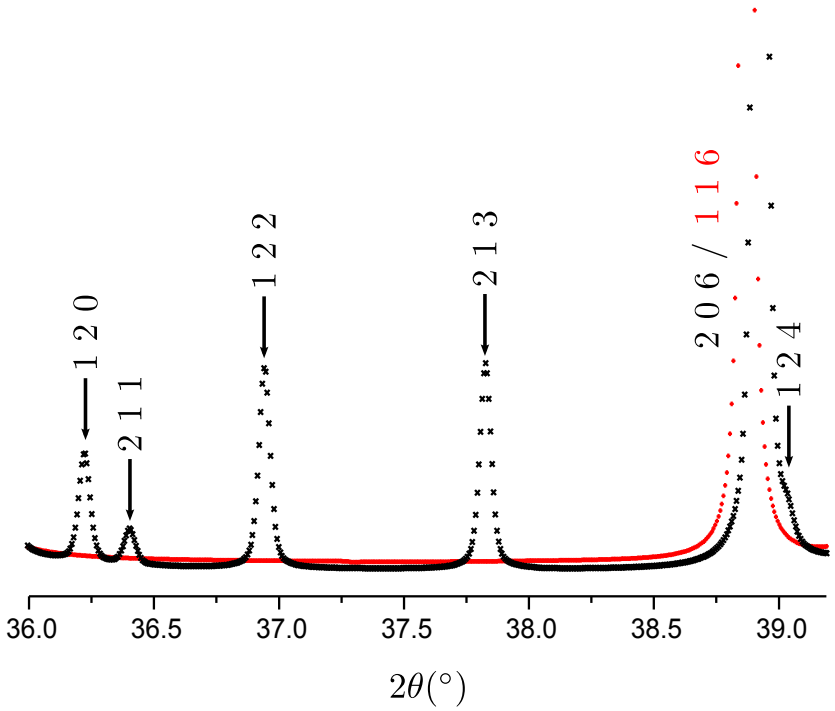

Figure 5-4: Comparison of a small region of the powder diffraction pattern of $SrBi_2Nb_2O_9$ at 643 K (black) and 733 K (red).

Table 5-3: Refinement parameters, lattice parameters, metal atomic positions and thermal parameters refined from variable temperature powder x-ray diffraction. For the refinement details of the 733 K structure (in $I4/mmm$) the atomic positions are displayed here in the pseudo-orthorhombic setting. All strontium and bismuth sites are fully occupied, where the SOF is less than one the remainder of the occupancy is accounted for by another atom, on exactly the same site, of the other species.

	293 K	413 K	528 K	643 K	693 K	703 K	733 K
Space Group	$A2_1am$	$A2_1am$	$A2_1am$	$A2_1am$	$A2_1am$	$A2_1am$	$I4/mmm$
a	5.51417(7)	5.51996(6)	5.52604(13)	5.53139(2)	5.53510(2)	5.53711(2)	5.5443(27)
b	5.51275(7)	5.51887(6)	5.52587(13)	5.53139(2)	5.53510(2)	5.53711(2)	5.5443(27)
c	25.07065(15)	25.09669(11)	25.12285(15)	25.14089(10)	25.14855(11)	25.15076(12)	25.17642(29)
R_p	6.104	9.337	10.841	8.641	8.462	8.493	9.522
wR_p	9.952	12.848	14.808	12.096	11.779	11.654	13.386
χ^2	4.679	3.468	4.020	3.517	3.419	3.366	2.245
Sr x	0	0	0	0	0	0	0
Sr y	0.24080(60)	0.24039(56)	0.24180(68)	0.23984(73)	0.24136(94)	0.2412(10)	0.25
Sr z	0	0	0	0	0	0	0
Sr SOF	0.764(3)	0.774(2)	0.773(3)	0.767(2)	0.769(2)	0.769(2)	0.76(2)
Sr B_{ij}	0.803(39)	1.514(21)	1.626(26)	2.252(23)	2.403(24)	2.642(24)	2.78(6)
Bi x	0.5085(12)	0.5049(8)	0.5025(11)	0.4988(12)	0.4967(17)	0.4944(25)	0.5
Bi y	0.73260(20)	0.73302(18)	0.73428(23)	0.73714(23)	0.73990(30)	0.74372(37)	0.75
Bi z	0.20060(4)	0.20104(4)	0.20085(4)	0.20108(4)	0.20107(4)	0.20107(4)	0.20067(5)
Bi SOF	0.8823(16)	0.8874(15)	0.8866(17)	0.8835(14)	0.8849(13)	0.8846(13)	0.88(2)
Bi B_{ij}	0.80(3)	1.51(2)	1.62(2)	2.25(2)	2.40(2)	2.64(2)	2.17(4)
Nb x	0.481(1)	0.4784(7)	0.4787(9)	0.483(1)	0.486(1)	0.488(2)	0.5
Nb y	0.7510(5)	0.7519(4)	0.7524(5)	0.7501(6)	0.7494(8)	0.7469(8)	0.75
Nb z	0.41363(6)	0.41361(5)	0.41345(6)	0.41336(5)	0.41332(5)	0.41323(5)	0.41371(8)
Nb B_{ij}	0.40(7)	0.35(4)	0.41(5)	0.57(4)	0.59(4)	0.74(4)	0.95(5)

Table 5-4: Anions atomic positions and thermal parameters refined from variable temperature powder x-ray diffraction. For the refinement details of the 733 K structure (in $I4/mmm$) the atomic positions are displayed here in the pseudo-orthorhombic setting, and O5 is not present in this structure.

	293 K	413 K	528 K	643 K	693 K	703 K	733 K
O1 x	0.437(4)	0.444(3)	0.445(4)	0.450(4)	0.460(6)	0.46(1)	0.5
O1 y	0.205(4)	0.216(4)	0.225(4)	0.220(4)	0.214(5)	0.203(6)	0.25
O1 z	0	0	0	0	0	0	0
O1 B_{ij}	0.5(2)	1.6(1)	2.0(1)	1.7(1)	1.8(1)	2.1(1)	3.54(4)
O2 x	0.466(3)	0.485(4)	0.507(7)	0.543(4)	0.542(4)	0.541(4)	0.5
O2 y	0.787(2)	0.796(2)	0.785(3)	0.784(3)	0.769(3)	0.755(3)	0.75
O2 z	0.3500(4)	0.3465(3)	0.3483(4)	0.3456(3)	0.3461(3)	0.3459(3)	0.3484(5)
O2 B_{ij}	0.5(2)	1.6(1)	2.0(1)	1.7(1)	1.8(1)	2.1(1)	3.2(3)
O3 x	0.719(4)	0.738(4)	0.735(5)	0.744(6)	0.744(9)	0.73(1)	0.75
O3 y	-0.013(6)	0.00(1)	0.00(2)	0.00(1)	0.00(1)	-0.003(9)	0
O3 z	0.25	0.25	0.25	0.25	0.25	0.25	0.25
O3 B_{ij}	0.5(2)	1.6(4)	2.0(1)	1.7(1)	1.8(1)	2.1(1)	2.3(3)
O4 x	0.660(3)	0.675(3)	0.677(3)	0.703(4)	0.711(5)	0.717(8)	0.75
O4 y	0.983(3)	1.002(4)	1.013(5)	0.987(4)	1.022(6)	1.033(7)	1
O4 z	0.0875(4)	0.0864(4)	0.0912(5)	0.0842(4)	0.0830(4)	0.0834(5)	0.0764(2)
O4 B_{ij}	0.5(2)	1.6(1)	2.0(1)	1.7(1)	1.8(1)	2.1(2)	2.4(2)
O5 x	0.721(5)	0.739(4)	0.743(5)	0.757(5)	0.749(7)	0.75(1)	—
O5 y	0.981(4)	0.997(6)	0.997(7)	0.984(6)	1.006(9)	1.00(1)	—
O5 z	0.5713(4)	0.5734(4)	0.5761(5)	0.5721(4)	0.5725(4)	0.5734(5)	—
O5 B_{ij}	0.5(2)	1.6(1)	2.0(1)	1.7(1)	1.8(1)	2.1(1)	—

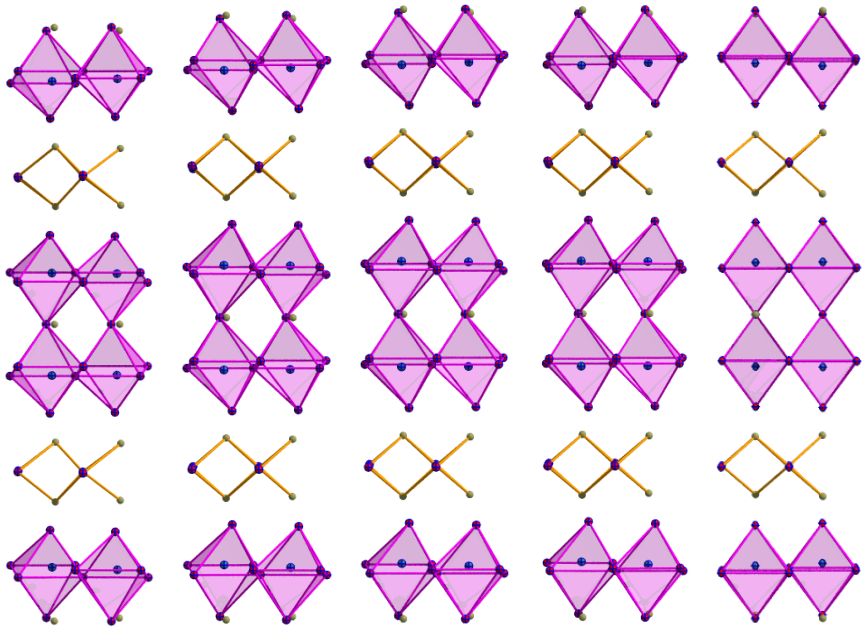

(a) 298 K (b) 643 K (c) 693 K (d) 703 K (e) 753 K

Figure 5-5: Rietveld refined structures of $SrBi_2Nb_2O_9$ from powder XRD data through the phase transition; at 298 K, (a); at 643 K, (b); at 693 K, (c); at 703 K, (d); and at 753 K, (e). The refinement of the 753 K data was performed in $I4/mmm$, whereas the remainder were performed in $A2_1am$.

Images of the structure of $SrBi_2Nb_2O_9$ at various temperatures around the phase transition are shown in figure 5-5. The change in the octahedral tilts and the niobium displacement can clearly be seen, as can the elongation of the $\boldsymbol{c}$ lattice parameter.

One of the aims of this experiment is to identify a structural order parameter, some quantity such as a bond length or atom position, which defines the loss of symmetry from the high temperature phase. Newnham et al. [5] proposed that in the bismuth titanate family, one of the principal structural changes at the phase transition was in fact the displacement of the apical oxygen of the octahedron. Their experiment utilized neutrons, however, whereas the current study used x-rays exclusively. Upon inspection of the data it became obvious that neutrons were necessary to refine this parameter accurately, and so another measure of the apical oxygen displacement was sought. The nearest cation to this oxygen is the bismuth site in the fluorite layer, and so its displacements from the prototypic position are plotted in figure 5-6.

A plot of the orthorhombicity, $o = 2(\boldsymbol{a}-\boldsymbol{b})/(\boldsymbol{a}+\boldsymbol{b})$, resulted in a graph that

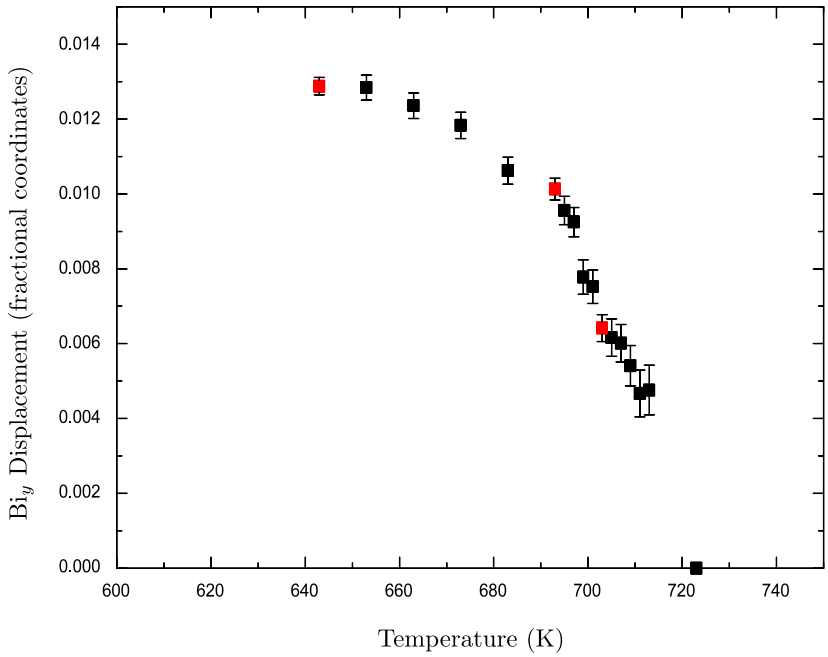

Figure 5-6: Bismuth displacements as a function of temperature in $SrBi_2Nb_2O_9$. The red data are from refinements of *major* experiments.

shows little, because of the relatively large error bars, and is not included here. This is because of the very similar values of the ***a*** and ***b*** lattice parameters (figure 5-7), and so a more direct measure of the difference was sought. To this end, the full width at half maximum (FWHM) peak width was measured for a peak that would be a singlet at high temperatures, and a doublet at low temperatures. The FWHM of the 315/135 peak is plotted in figure 5-9, with the bismuth displacements included for comparison. An initial assumption would be that the ***a*** and ***b*** lattice parameters would be different at low temperature, and then gradually converge to a common value at the phase transition. What is observed, however, is a contraction of the 315/135 peak up to 640 K, and then an expansion as the temperature is further increased. To characterise this behaviour further, and to discover the (very) high temperature behaviour, a variable temperature powder diffraction run was implemented, wherein only the 315 peak was studied. This allowed for a much larger range of temperatures to be observed. The peak positions and FWHM determined from this detailed experiment are shown in figure 5-10.

The ***c*** lattice parameter and the cell volume were also plotted to find any indication of the nature of the phase transition (these can both be seen in figure 5-8).

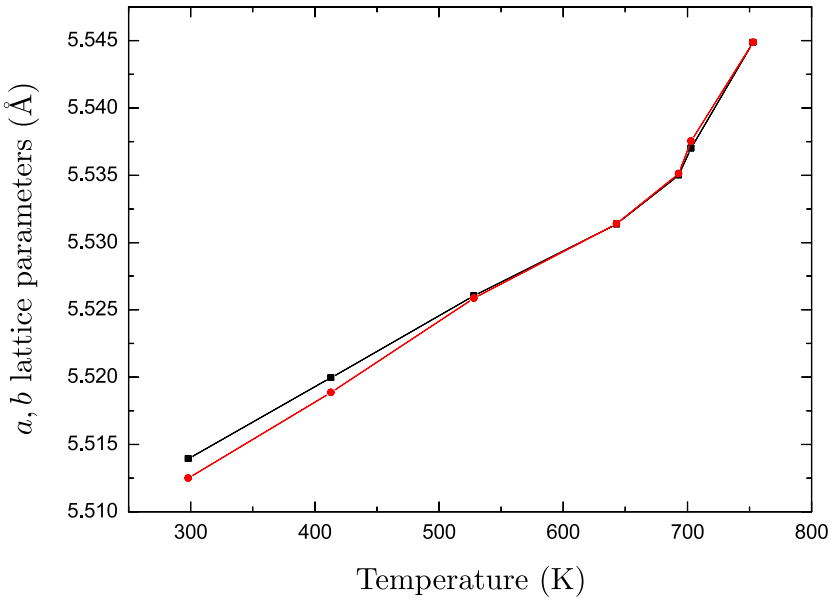

Figure 5-7: The ***a*** and ***b*** lattice parameters as a function of temperature in $SrBi_2Nb_2O_9$. The error bars are omitted for clarity.

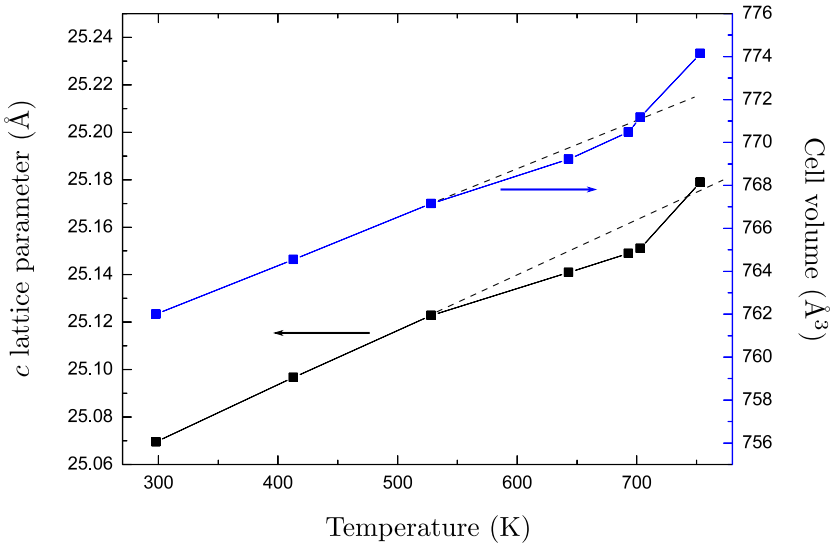

Figure 5-8: The ***c*** lattice parameter and cell volume as a function of temperature in $SrBi_2Nb_2O_9$.

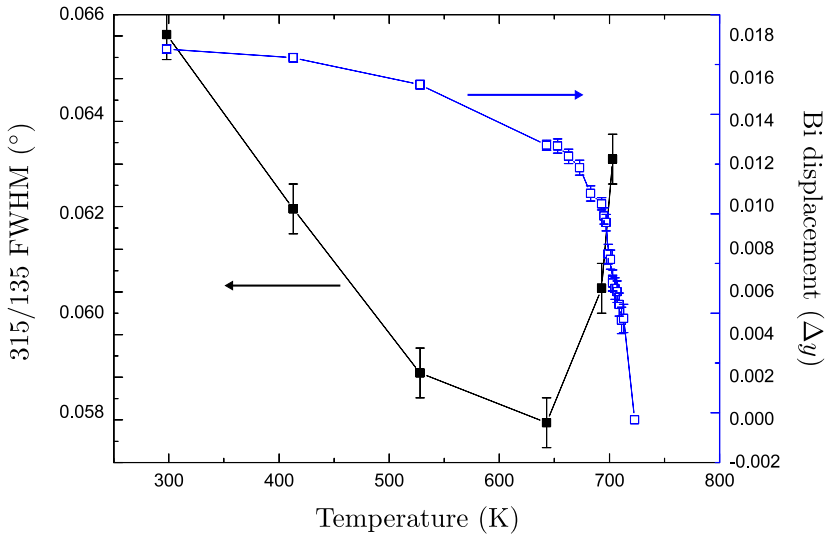

Figure 5-9: FWHM of 315/135 peak/s and bismuth displacements as a function of temperature in $SrBi_2Nb_2O_9$.

Considering the structural mechanisms which lead to the orthorhombicity in this material yields some insight into the chemistry of the phase transition. To a good approximation cation displacement in the polar direction lengthens the lattice parameter in this direction. This is an effect which works to oppose that of the tilting of the oxygen octahedra, which leads to a contraction of the lattice parameter in the direction of the tilting. Since the tilting in $SrBi_2Nb_2O_9$ is not the same in the ***a*** and ***b*** directions, octahedral tilting will also lead to a net orthorhombic distortion. There could then, theoretically, be a temperature where the distortion in the ***a*** direction from cation displacement combined with the distortion in the ***a*** direction due to the octahedral tilting equalled the distortion in the ***b*** direction from the tilting alone. This would give a metrically tetragonal structure that would become orthorhombic upon heating or cooling. Another alternative is the role that domains play in the transition. As the orthorhombicity reduces and the difference in ***a*** and ***b*** becomes smaller, the energy required for domain formation will similarly reduce. Optically, these domains are not observed (§4.3) but that does not preclude their existence; only constraining that their size is smaller than the wavelength of the light used in the optical experiment. With the formation of domains comes the necessary domain wall formation; these ferroelastic domain walls will undergo a strain to accommodate the lattice mismatched neighbouring

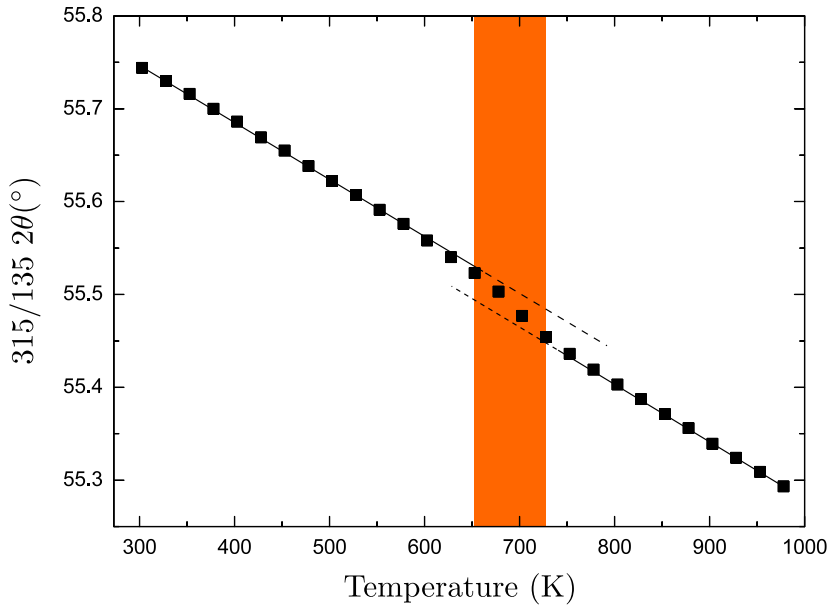

(a) 315/135 peak position as a function of temperature

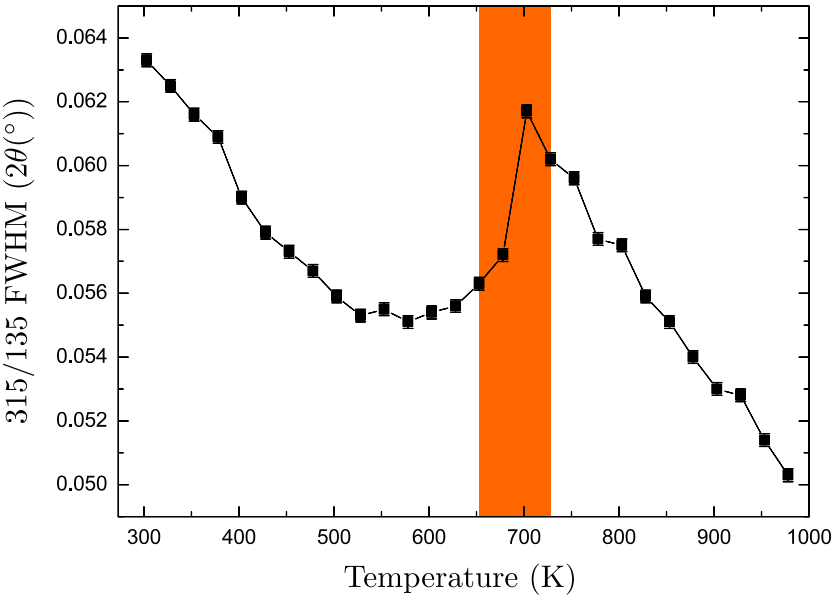

(b) 315/135 peak FWHM as a function of temperature

Figure 5-10: 315/135 peak parameters as a function of temperature; the peak position in 2θ, (a) and the peak FWHM in 2θ (b). The orange area highlights the temperature range where a non-linear shift in the peak position occurs and shows the correlation between this and the unusual peak width.

domains on either side. Due to the small size of these domains, which are envisaged as nano-domains, as they are not observed optically in single crystals, the volume density of domain walls will be relatively large, in turn producing a large effect on the diffraction pattern *via* broadening of the peaks. It is also possible that this broadening is due to a coexistence of phases region associated with a first-order phase transition. This might be discounted by studying the widths of the orthorhombic tilt peaks; however, as the intensities of these peaks are so low in this temperature region, a reliable measure of the peak width cannot be found from the present data. Of these three possible explanations the domain theory seems to carry the most credence: the fact the the broadening persists into the high temperature region (where the orthorhombic tilt peaks have reduced in intensity to the level of the noise) suggests that any coexistence region would have to still be present, in the absence of the orthorhombic structure. Close to the phase transition in an orthorhombic structure that is very nearly tetragonal, ferroelastic (90°) domain formation is energetically favourable. It is the conclusion, therefore, that this broadening, and the apparently increased resultant orthorhombicity near the phase transition, is the result of domain formation.

5.4 The $Sr_{1+x}Bi_{2-x}Nb_2O_{9-x}F_x$ Solid Solution

In order to investigate the chemistry of adding fluorine to an Aurivillius ferroelectric, $SrBi_2Nb_2O_9$ was fluorinated, to form $Sr_{1+x}Bi_{2-x}Nb_2O_{9-x}F_x$. Due to the method of synthesis there was a very small yield, and so for diffraction the powder was ground and dispersed in Apiezon vacuum grease on a slice of off-cut silicon. The diffraction patterns were taken at room temperature in-house on our PANalytical MPD. Each experiment took an extended time of around 15 hours, because of the low signal from the small sample volume. Since the electron number of chemically bound oxygen (O^{2-} and fluorine (F^-) are identical and hence cannot be distinguished by x-ray diffraction, refinements were carried out using the unfluorinated $SrBi_2Nb_2O_9$ model.

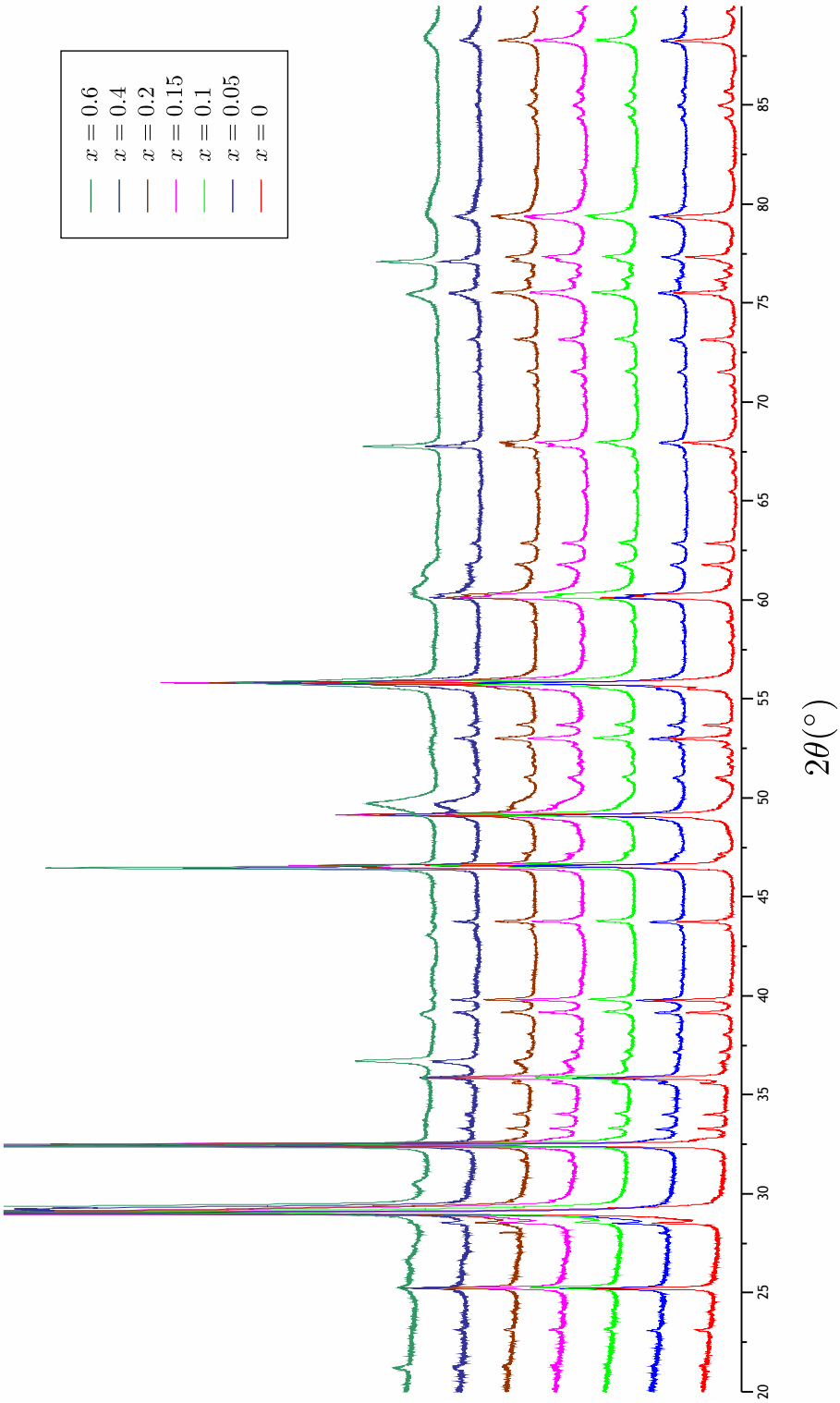

Figure 5-11: Powder x-ray diffraction patterns of $Sr_{1+x}Bi_{2-x}Nb_2O_{9-x}F_x$.

Table 5-5: Rietveld refinement details and refined structure of various $Sr_{1+x}Bi_{2-x}Nb_2O_{9-x}F_x$ compositions

x	5	10	15	20	40	60
wR_p	6.171	9.564	13.438	14.837	25.682	20.014
χ^2	1.566	2.461	3.756	3.895	3.884	5.346
a	5.51537(33)	5.51943(46)	5.52028(30)	5.52198(26)	5.5265(13)	5.535(11)
b	5.51543(32)	5.51886(48)	5.51660(31)	5.51640(28)	5.5267(14)	5.535(11)
c	25.05261(35)	25.05273(48)	25.04822(70)	25.04734(78)	24.7306(29)	24.5558(23)
Sr x	0	0	0	0	0	0
Sr y	0.2401(12)	0.2306(11)	0.2275(15)	0.2269(20)	0.2489(38)	0.247(38)
Sr z	0	0	0	0	0 0	
Sr SOF	0.7213(30)	0.6682(46)	0.7375(68)	0.7501(84)	0.395(77)	0.652(20)
Bi x	0.5346(15)	0.5287(24)	0.5185(43)	0.5082(55)	0.5112(41)	0.501(28)
Bi y	0.73356(44)	0.74045(72)	0.74259(82)	0.7453(10)	0.7517(30)	0.7517(45)
Bi z	0.199918(54)	0.199984(78)	0.20025(13)	0.20017(15)	0.2027(15)	0.20079(32)
Bi SOF	0.8607(15)	0.8341(23)	0.8687(34)	0.8751(42)	0.698(38)	0.8261(98)
Nb x	0.5229(16)	0.5322(22)	0.5285(33)	0.5227(41)	0.5189(47)	0.504(25)
Nb y	0.7489(13)	0.72458(95)	0.7253(13)	0.7244(14)	0.7397(38)	0.752(17)
Nb z	0.413961(74)	0.413785(84)	0.41347(11)	0.41335(13)	0.4054(11)	0.40788(31)
O1 x	0.5984(47)	0.535(12)	0.523(16)	0.501(19)	0.739(24)	0.787(60)
O1 y	0.2140(67)	0.1691(46)	0.1541(59)	0.1381(58)	-0.012(29)	0.504(53)
O1 z	0	0	0	0	0	0
O2 x	0.6013(32)	0.5381(93)	0.5382(93)	0.520(12)	0.4944(93)	0.50(11)
O2 y	0.7751(49)	0.7224(51)	0.7029(50)	0.6905(49)	0.7072(50)	0.752(71)
O2 z	0.35248(44)	0.35320(56)	0.35303(65)	0.35363(74)	0.3730(19)	0.3790(30)
O3 x	0.7619(56)	0.7856(91)	0.785(15)	0.770(21)	0.659(14)	0.793(43)
O3 y	0.0378(46)	0.0005(88)	-0.003(13)	-0.001(14)	-0.040(17)	0.025(52)
O3 z	0.25	0.25	0.25	0.25	0.25	0.25
O4 x	0.7538(56)	0.6735(55)	0.6042(93)	0.495(26)	0.418(26)	0.809(71)
O4 y	0.9654(57)	0.8763(57)	0.8777(87)	0.8755(77)	0.846(19)	0.948(64)
O4 z	0.08142(60)	0.08706(83)	0.0795(11)	0.0732(14)	0.0416(42)	0.0820(23)
O5 x	0.6815(41)	0.7817(96)	0.7336(78)	0.7073(76)	0.740(12)	1.01(16)
O5 y	0.9748(47)	1.0069(91)	1.009(10)	1.0159(77)	0.969(12)	0.75(14)
O5 z	0.57008(68)	0.57198(71)	0.57452(58)	0.57609(64)	0.5395(19)	0.5302(27)

It is seen from the diffraction patterns of $Sr_{1+x}Bi_{2-x}Nb_2O_{9-x}F_x$ in figure 5-11, and the corresponding Rietveld fits in figure 5-12, that a new phase becomes prevalent with increasing x, and that the crystallinity of the Aurivillius phase also decreases. This leads to significant errors in the refinement of the higher x compounds, particularly the x = 0.6 sample which is dominated by this new phase. The latter is unidentifiable because of the exceptionally broad peak-shapes, meaning that the d-spacing cannot be measured accurately. The gradual growth of this phase, rather than a sudden and complete transformation, implies that the fluorine substitutes into the $SrBi_2Nb_2O_9$ structure and forms a completely new phase rather than subtly modifying the parent structure. It is feasible, however, that the formation of a new phase at the expense of the parent structure causes vacancies and disorder in the $SrBi_2Nb_2O_9$, leading to the observed reduction in crystallinity. The idea of two separate structures therefore does not overturn the results derived from the refinements as seen in figure 5-13; these are (i) increasing disorder on the strontium site, and (ii) decreasing displacement of the bismuth. Close analysis of the x = 0.05 powder pattern indicates that the smaller disorder on the Sr-Bi site, as well as other anomalous results at this composition are related with the absence of a broad shoulder to higher angle in the *115* (and other) peaks, as seen in figure 5-14. This feature is present in all of the other samples fabricated in this series, but is absent, or at least significantly less prominent, in the x = 0.05 sample. This is suggestive of a subtle difference either in the structure/symmetry, or a difference in sample quality brought about by a slight variation in the sample synthesis.

5.5 $CsBiNb_2O_7$

Polycrystalline $CsBiNb_2O_7$ was taken to station D2B at the Institut Laue-Langevin (ILL) for variable-temperature constant-wavelength neutron diffraction[6]. Neutrons were used for this experiment as it was suggested that any ferroelectric phase transition would principally involve the oxygen octahedra. The experiment used D2B in the high-resolution mode, with neutrons at a wavelength of 1.5943 Å. Roughly 5 g of material was placed into a 10 mm diameter vanadium can, due to

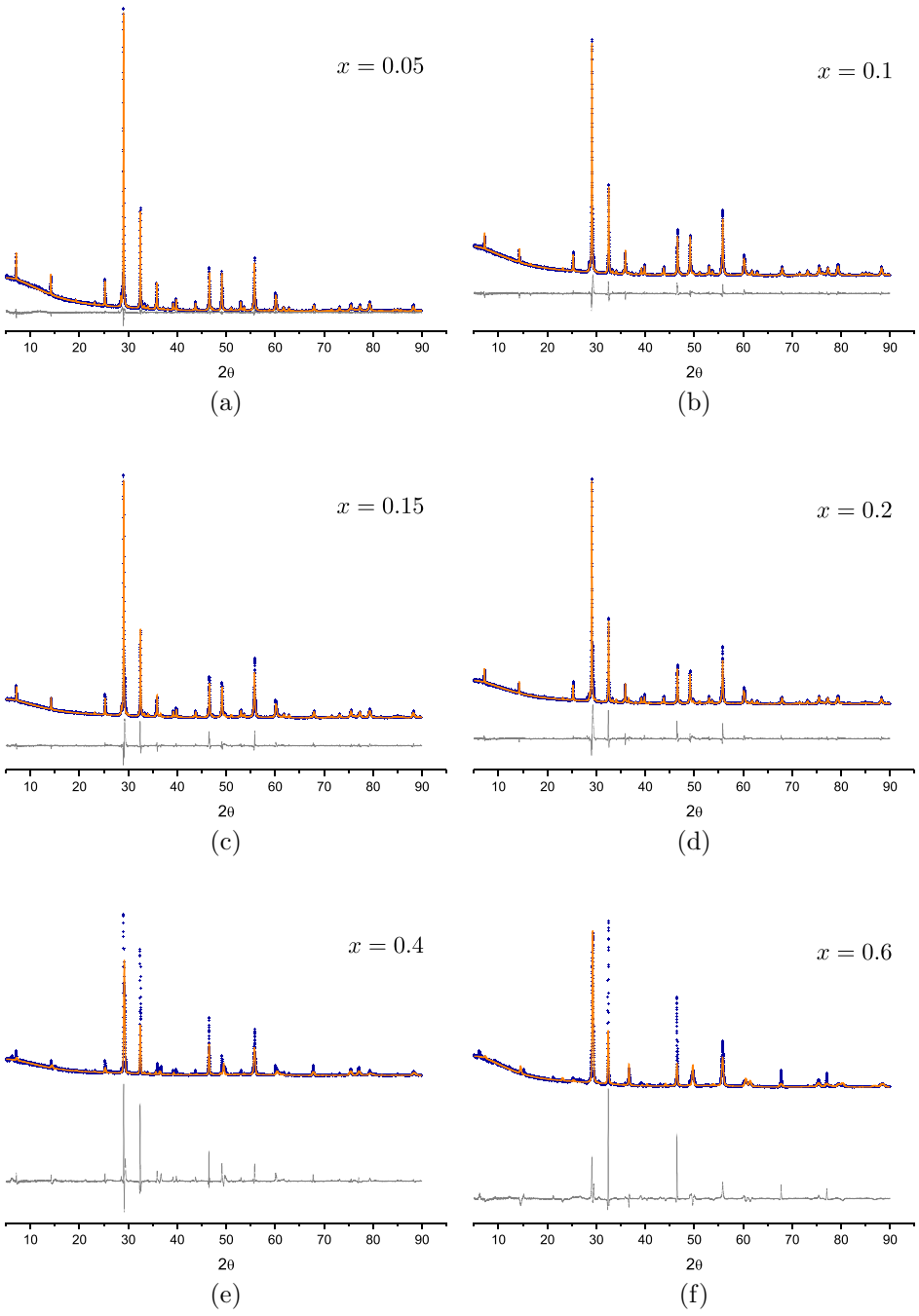

Figure 5-12: Rietveld refinements of structure of $Sr_{1+x}Bi_{2-x}Nb_2O_{9-x}F_x$ with increasing fluorine content; with x = 0.05, (a); with x = 0.1, (b); with x = 0.15, (c); with x = 0.2, (d); with x = 0.4, (e); and with x = 0.6, (f). Notice the drastic reduction in the quality of the fit from using a single phase, aurivillius structure.

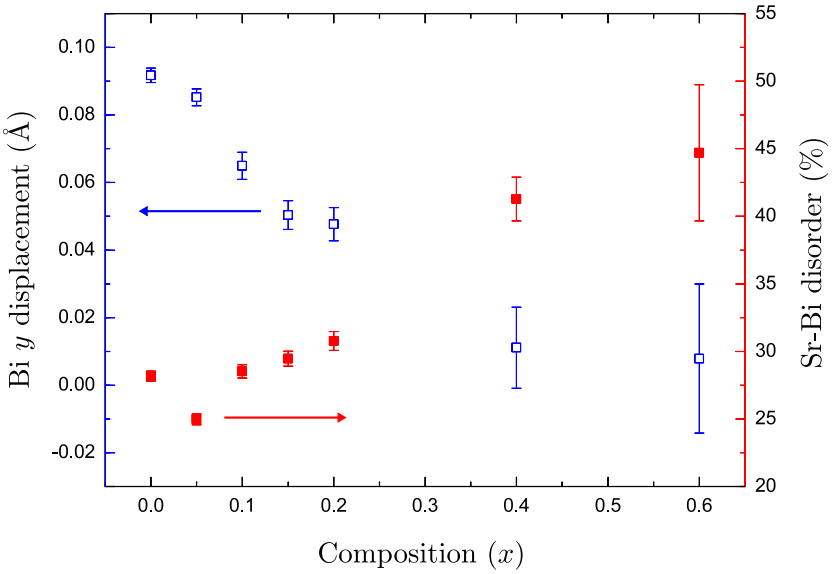

Figure 5-13: Bi y displacement (□) and strontium-bismuth disorder (■) in $Sr_{1+x}Bi_{2-x}Nb_2O_{9-x}F_x$ as a function of fluorination, x. As the composition moves toward higher x, the growth of another, non-Aurivillius phase causes the refinement to become less reliable.

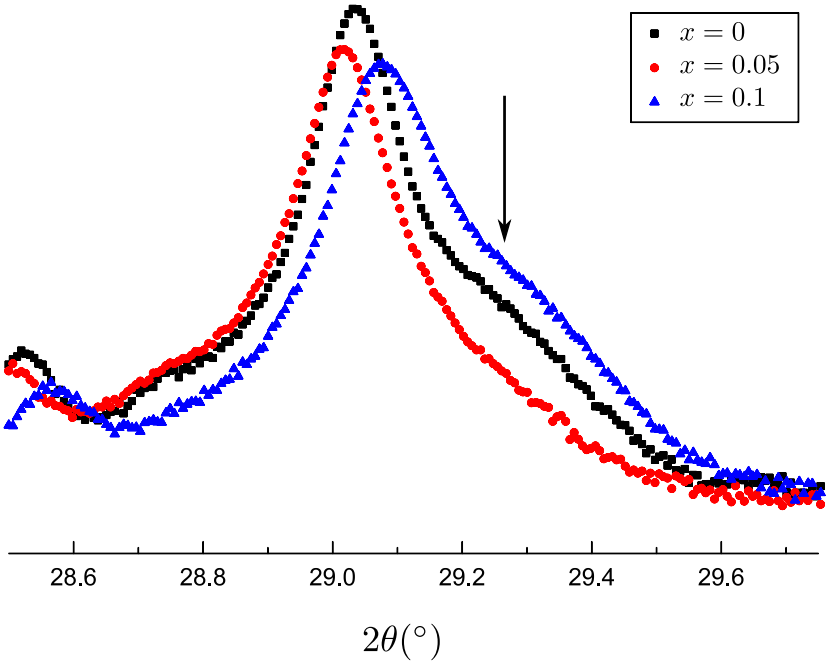

Figure 5-14: Powder XRD patterns of the *115* peakshape, in a logarithmic scale, for $Sr_{1+x}Bi_{2-x}Nb_2O_{9-x}F_x$ at $x = 0$, 0.05, and 0.1, highlighting an unusual shape in the $x = 0.05$ sample. The difference in d-spacing of the peak is due to the mounting procedure.

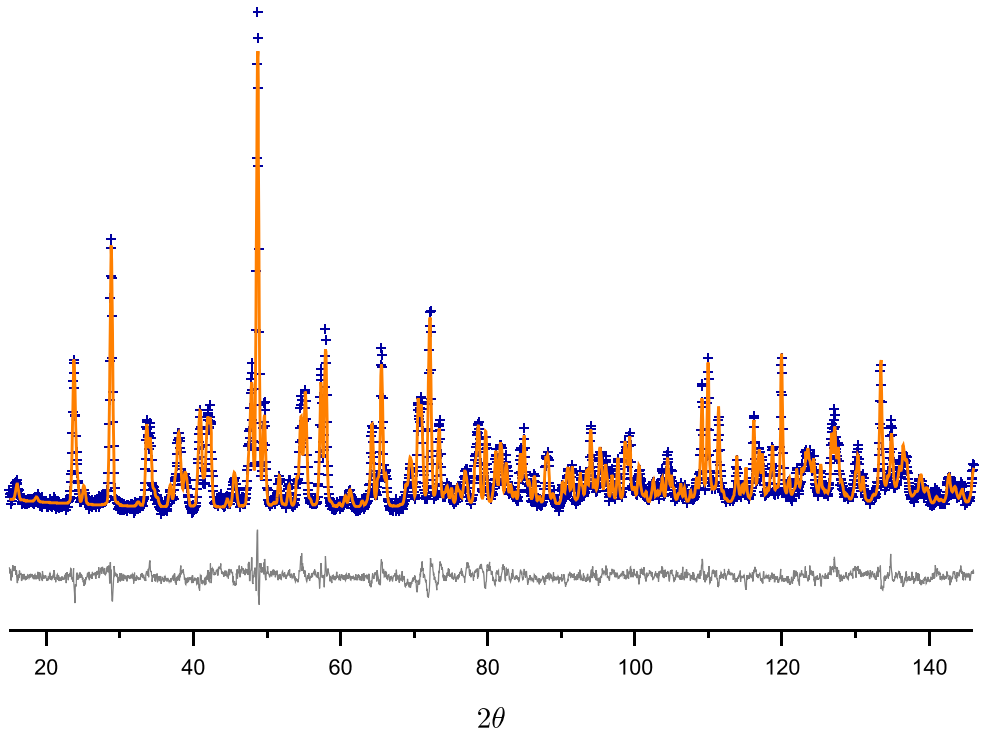

Figure 5-15: Neutron powder diffraction pattern (Blue +), final Rietveld refinement (Orange), and difference plot (Grey) for $CsBiNb_2O_7$ at room temperature

its very low neutron scattering length. Measurements lasting 3.3 hours were taken at room temperature, 393 K, and then every 100 K to 1173 K, in an evacuated furnace. The room-temperature pattern, the final Rietveld fit, and the subsequent difference plot are shown in figure 5-15. Experiments at higher temperatures were not feasible as the material volatilised and underwent sublimation at around 1220 K. The refinements were carried out in space group $P2_1am$, as proposed by Snedden et al. [2].

A common feature of all of the patterns is the intially low calculated intensity of the *220* peak. This miscalculation was accounted for with the introduction of preferred orientation, consistent with the observations on single crystals of $CsBiNb_2O_7$ forming as platelets. The refined structure at room temperature is very similar to that of Snedden et al. [2]. The pertinent information in a search for a ferroelectric phase transition, including the lattice parameters and the relevant bismuth position at each temperature, is presented in table 5-6. The Rietveld fits of the diffraction patterns are seen in figures 5-16, 5-17, and 5-18.

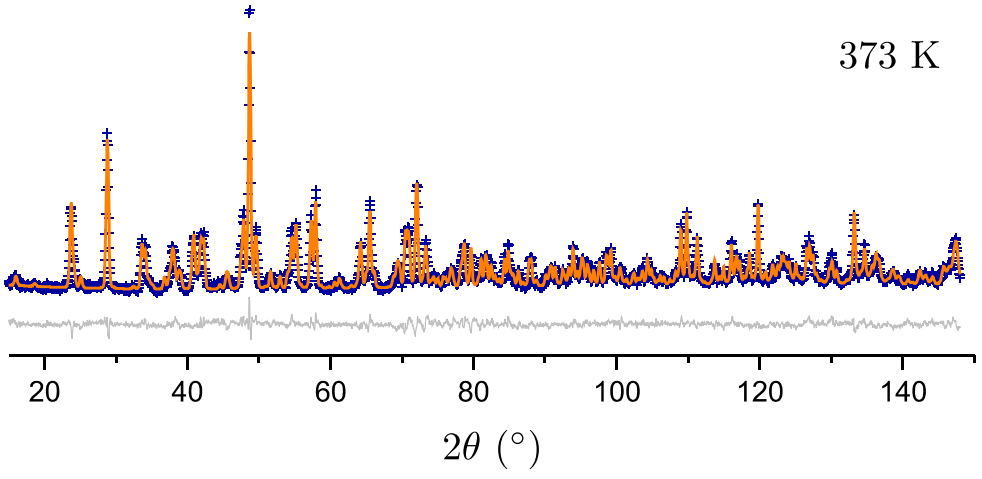

(a)

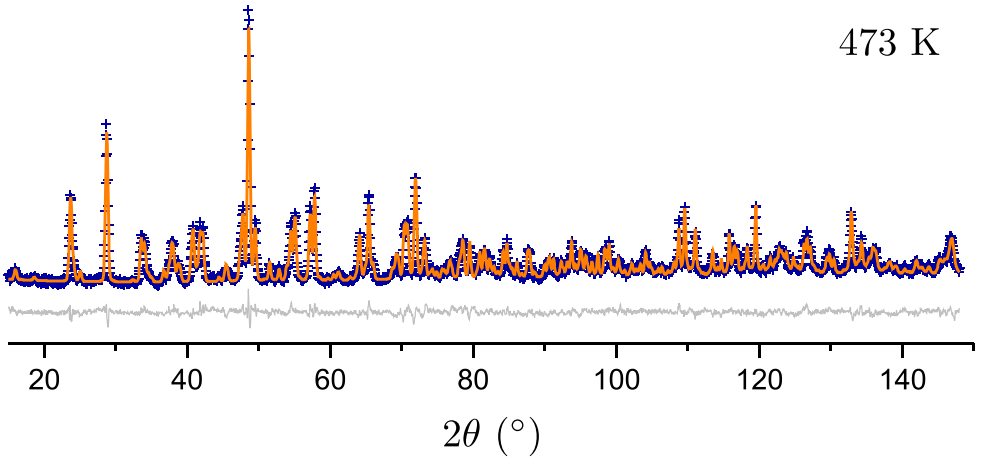

(b)

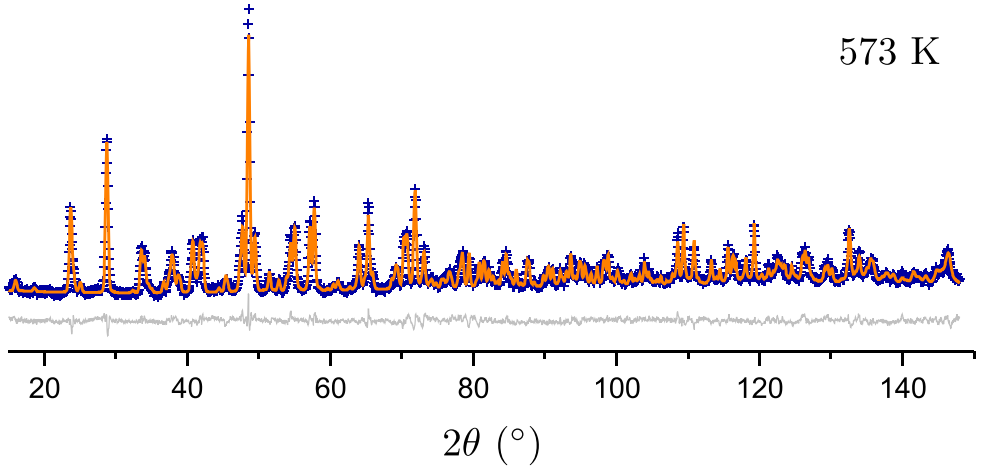

(c)

Figure 5-16: Rietveld refinement fits of variable temperature neutron powder diffraction of $CsBiNb_2O_7$; at 373 K, (a); at 473 K, (b); and at 573 K, (c).

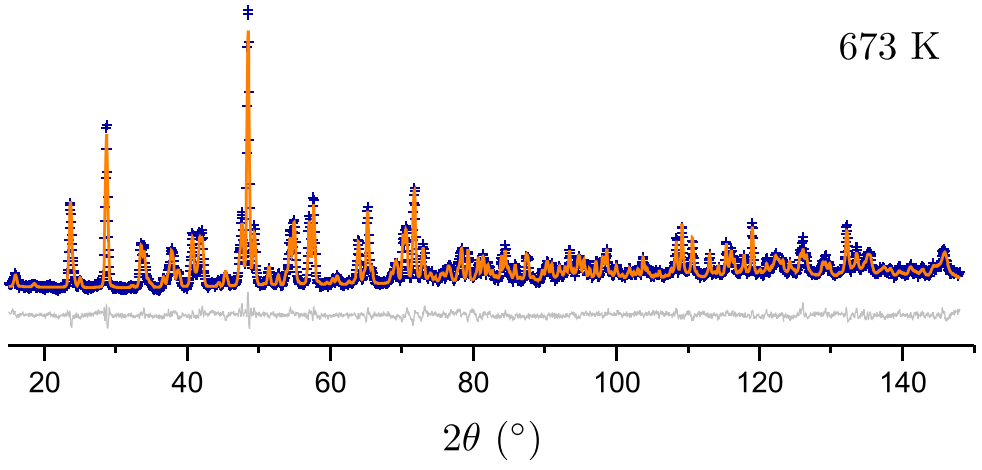

(a)

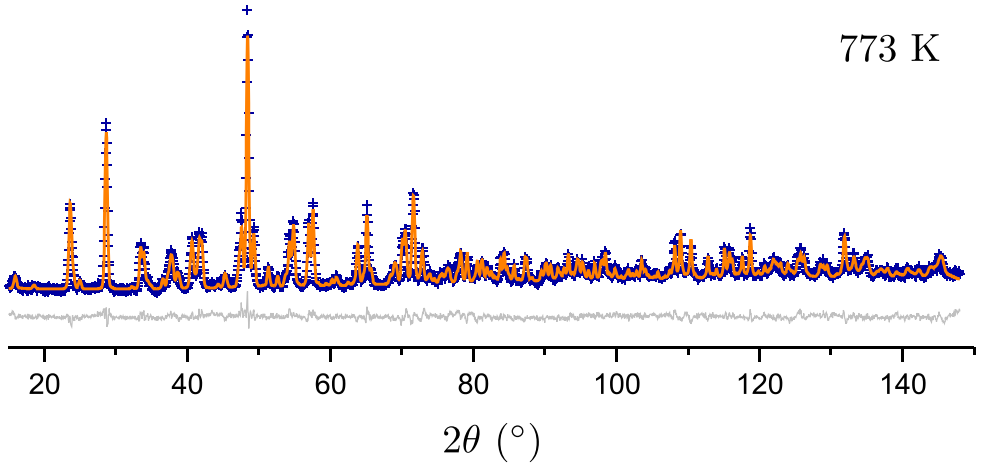

(b)

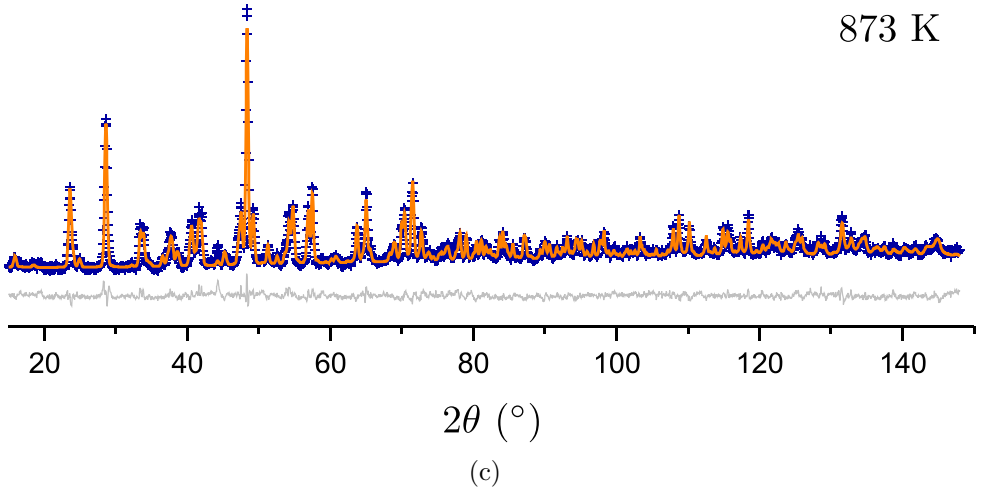

(c)

Figure 5-17: Rietveld refinement fits of variable temperature neutron powder diffraction of $CsBiNb_2O_7$; at 673 K, (a); at 773 K, (b); and at 873 K, (c).

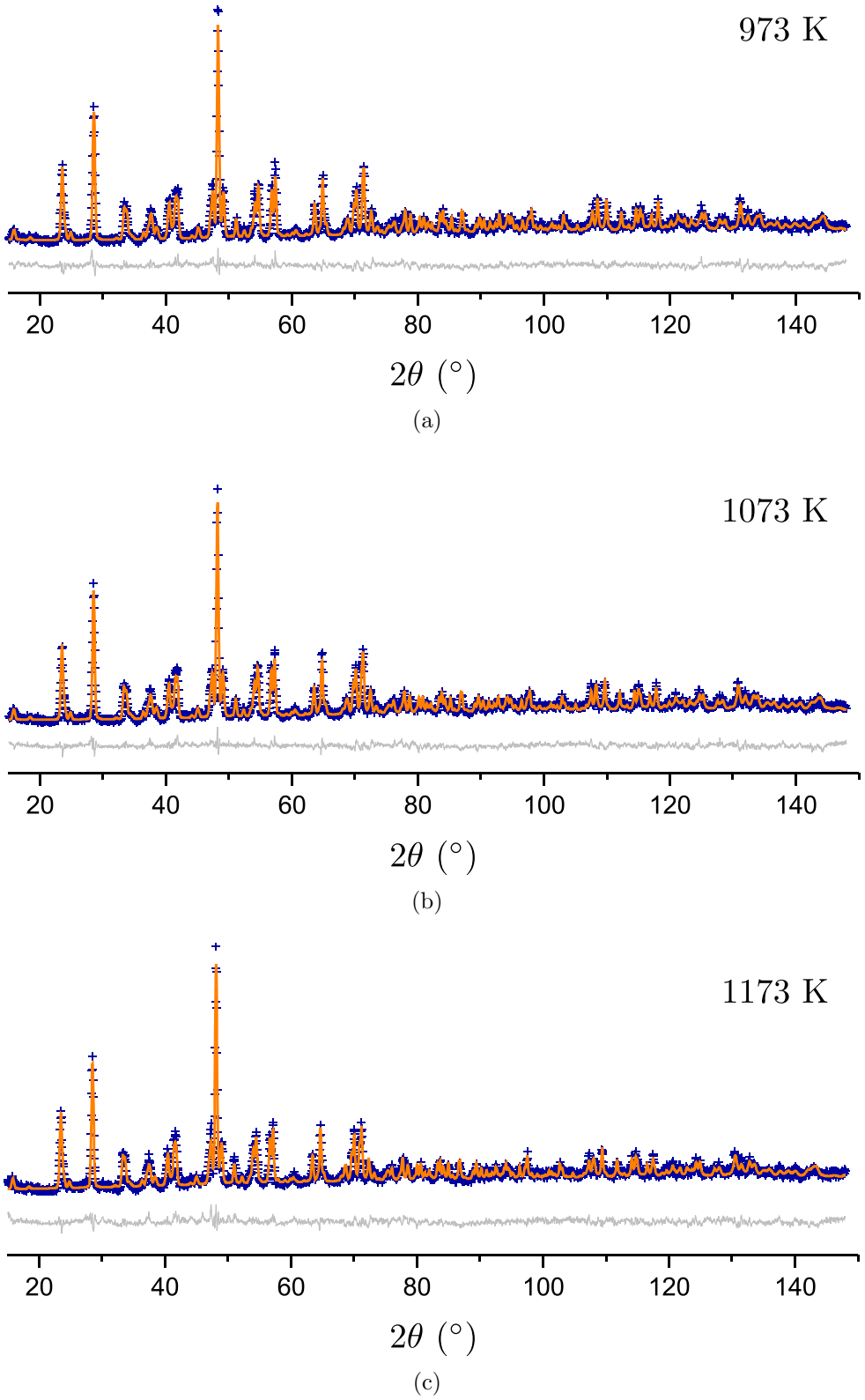

Figure 5-18: Rietveld refinement fits of variable temperature neutron powder diffraction of $CsBiNb_2O_7$; at 973 K, (a); at 1073 K, (b); and at 1173 K, (c).

Table 5-6: Brief refinement details of variable temperature neutron diffraction experiments performed on $CsBiNb_2O_7$, including the lattice parameters, and the weighted profile R-factor.

T (K)	a	b	c	R_{wp}	χ^2
298	5.49258(9)	5.41991(9)	11.36858(29)	4.874	0.632
373	5.49704(10)	5.42455(9)	11.38038(31)	5.057	0.629
473	5.50348(10)	5.43118(10)	11.39547(34)	5.156	0.629
573	5.51006(12)	5.43861(12)	11.41063(37)	5.073	0.616
673	5.51698(15)	5.44625(14)	11.42553(40)	5.131	0.623
773	5.52358(14)	5.45411(14)	11.44119(39)	5.551	0.676
873	5.53013(18)	5.46214(19)	11.45682(41)	5.183	0.632
973	5.53738(21)	5.47142(22)	11.47229(44)	4.956	0.606
1073	5.54428(22)	5.48194(23)	11.50212(49)	5.114	0.625
1173	5.55128(31)	5.49414(32)	11.48697(54)	6.916	0.925

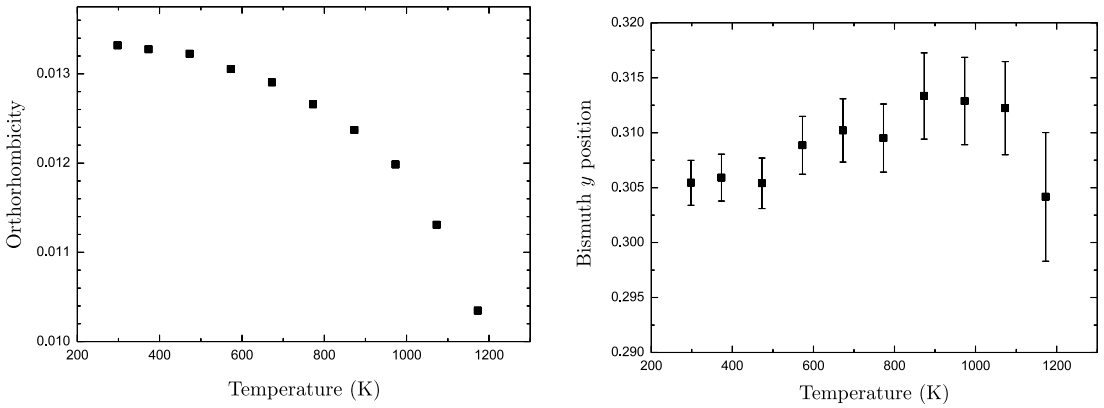

(a) Orthorhombicity (b) Bi y position

Figure 5-19: Refined orthorhombicity (a) and Bi displacement (b) of $CsBiNb_2O_7$ as a function of temperature from neutron diffraction. Neither of these measures suggest a ferroelectric phase transition in the temperature region studied.

Graphs of the orthorhombicity, defined as $o = 2(\boldsymbol{a}-\boldsymbol{b})/(\boldsymbol{a}+\boldsymbol{b})$, and the bismuth position as a function of temperature can be seen in figure 5-19. If a ferroelectric phase transition took place in this region, it would manifest itself as a reduction in the cation displacement and oxygen octahedra tilting, combined with a move towards the tetragonal high temperature phase. This phase is of space group $P4/mmm$, which has no displacements from the ideal positions.

Figure 5-20 shows a plot of Δx and Δy for the four oxygen sites as a function of temperature, where Δx is defined as the x-displacement of the atom from the ideal position in the prototypic phase. The Δz positions are not included as the mirror

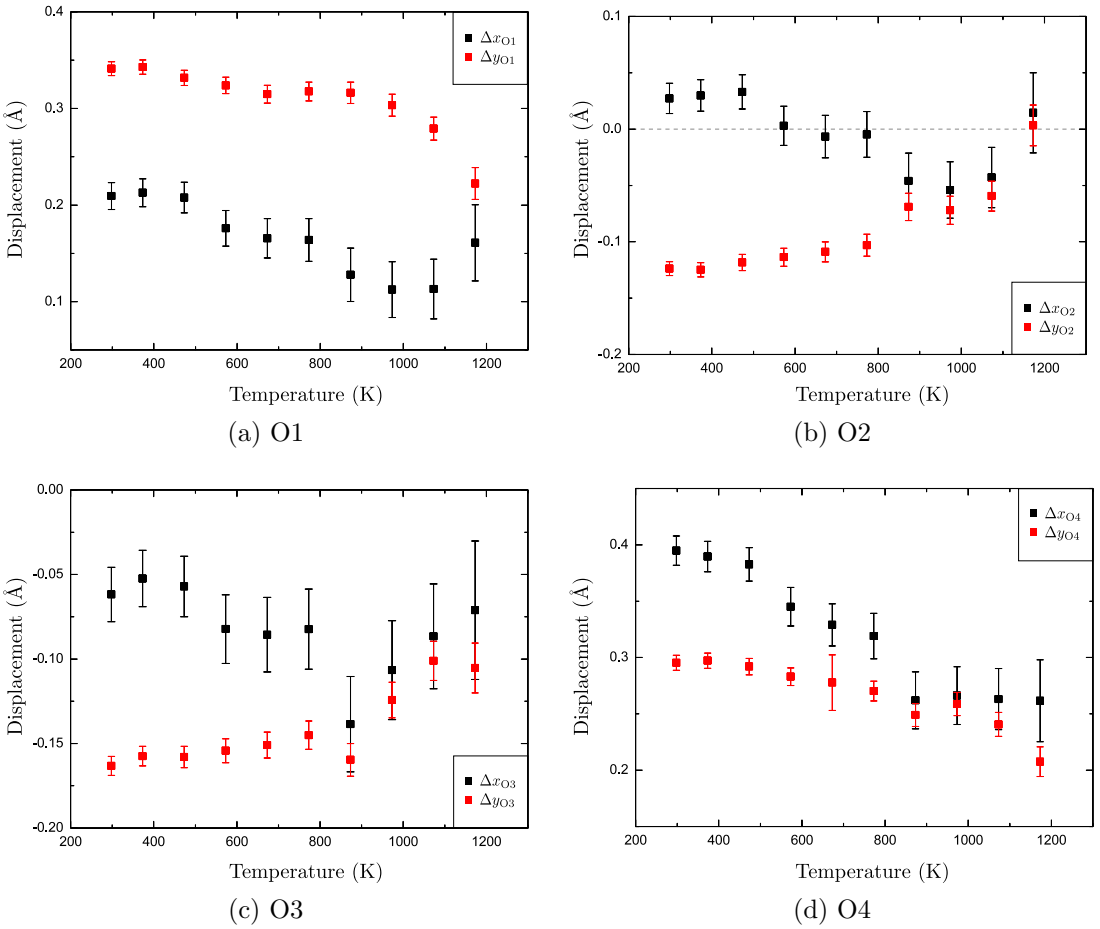

(a) O1 (b) O2

(c) O3 (d) O4

Figure 5-20: Refined x and y displacements of the four oxygen sites in $CsBiNb_2O_7$; the linking site O1, (a), the outer apical site O2, (b), and the equatorial sites, O3 (c) and O4 (d).

plane (space group $P2_1am$) precludes there being any net polarization in this direction. The displacements of the linking site (O1) do not suggest any transitions in this temperature range. The location of the other three sites, however, seem to indicate a change in the displacement direction from [010] to [110] between 773 K and 873 K, which is in agreement with the temperature predicted by Fennie and Rabe [7]. This change is especially noticeable in the O2 site, where the Δx appears to be near zero at below 773 K and seems to jump at 873 K. However, these changes in displacements are very small (~0.1 Å) and consequently will lead to a negligible change in polarization.

The neutron diffraction results suggest therefore that some form of phase "change" does occur at between 773 K and 873 K. This does not entail any change of space group, lattice parameters or orthorhombicity, just a very small tilting of

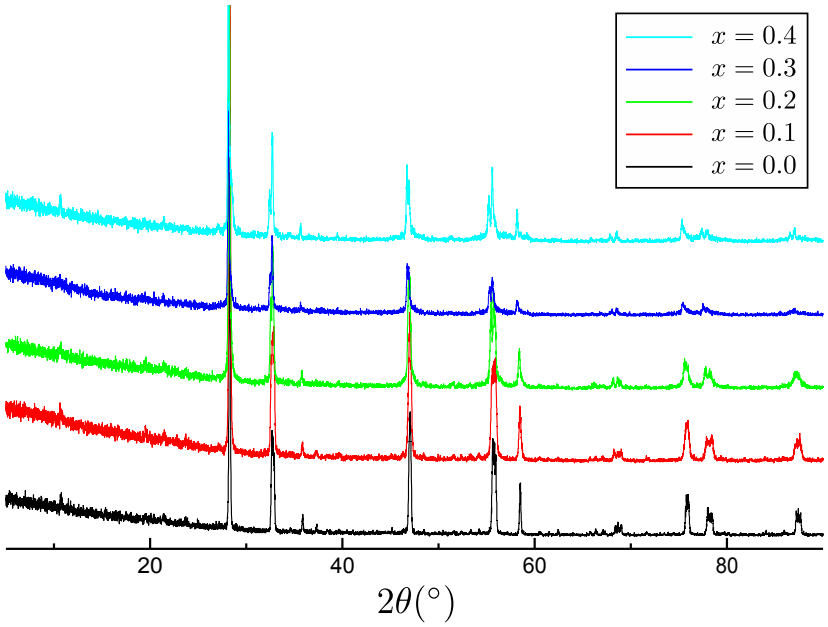

Figure 5-21: $Bi_2W_{1-x}Nb_xO_{6-x}F_x$ powder x-ray diffraction patterns

the oxygen octahedra. It is feasible that these changes just signify the first measurable signs of a second order phase transition that actually occurs at a much higher temperature, although since the displacements materialize in shifts away from the prototypic position, this seems unlikely.

5.6 $\mathbf{Bi_2W_{1-x}Nb_xO_{6-x}F}_x$

Powder diffraction was performed on the $Bi_2W_{1-x}Nb_xO_{6-x}F_x$ series, and the patterns obtained can be seen in figure 5-21. The relatively small volume of sample gained from the growth process required that the diffraction be done in transmission mode, and as such these patterns were taken by Richard Goff at the University of St Andrews, on a Stoe Stadi P diffractometer, with CuKα radiation.

The initial model structure of Bi_2WO_6 was based upon that of McDowell et al. [8], *i.e.* orthorhombic in space group $Pca2_1$. For refinements with non-zero values of x the relevant occupancies of Nb and W were assigned to the W site and were not allowed to refine. No fluorine was included in the refinement for the reasons outlined in section 5.4. The ***a*** and ***c*** lattice parameters are plotted in figure 5-22, and show a reduction in the orthorhombicity as a function of x. Many of the

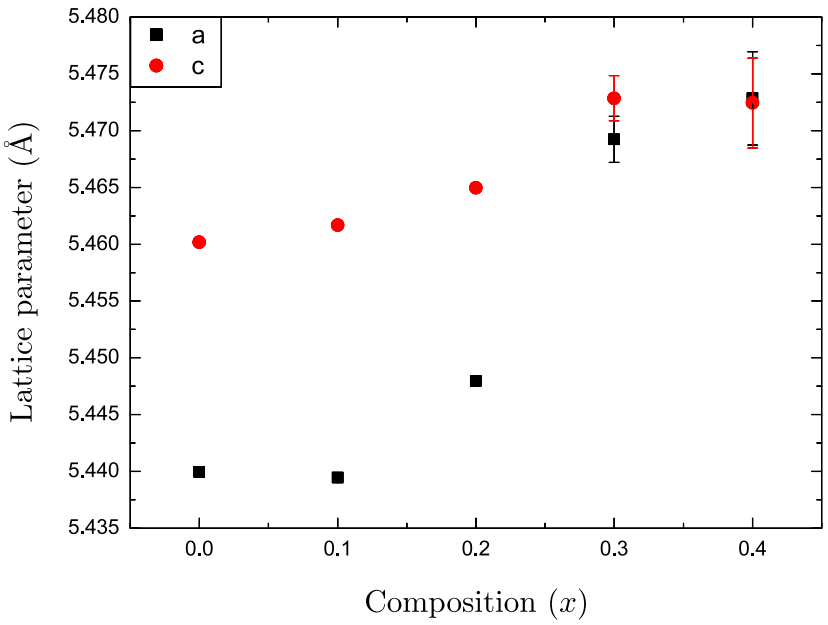

Figure 5-22: Lattice parameters of $Bi_2W_{1-x}Nb_xO_{6-x}F_x$from powder x-ray diffraction

structural elements of this material demonstrate large standard deviations because of the relatively low resolution and poor counting statistics of these measurements. Despite this, trends can be seen in the cation positions; all move towards the prototypic positions with increasing x. Also worthy of note is the structure of the x = 0.4 phase, wherein the oxygen sites in the fluorite layers demonstrate a displacement in the fluorite plane. The angle between the fluorite oxygen plane and the z–direction is 12.5°± 0.5°. The high temperature phase of Bi_2WO_6 loses the archetypal Aurivillius structure and forms in monoclinic space group $A2/m$, and this angle of oxygen displacement is remarkably close to β in this high temperature phase (102.334° – 90° = 12.334°) [8]. Attempts at refining the x = 0.4 sample in $A2/m$, however, were unsuccessful, suggesting a move toward the non-Aurivillius phase, but without the associated change in symmetry. This is also indicated in the oxygen octahedra, the tilt of which is 27.5° to the horizontal, where 45° indicates the side sharing octahedra as seen in the monoclinic phase. Attempts at synthesising the x = 0.5 composition were unsuccessful, suggesting that the structure is pushed beyond some threshold of stability by the introduction of this much substitution.

Table 5-7: Brief refinement details of variable temperature neutron diffraction experiments performed on $CsBiNb_2O_7$, including the lattice parameters, and the best measure of polarization, which is the bismuth site y position.

x	0	10	20	30	40
a	5.43995(11)	5.43934(18)	5.44718(32)	5.4689(19)	5.4727(30)
b	16.43991(33)	16.4657(54)	16.4881(86)	16.518(196)	16.563(14)
c	5.46016(11)	5.46180(18)	5.46519(30)	5.4700(20)	5.473(30)
Bi1 x	0.5226(13)	0.517(2)	0.522(2)	0.526(2)	0.512(7)
Bi1 y	0.4222(6)	0.4223(7)	0.4213(9)	0.4214(8)	0.421(3)
Bi1 z	0.9773(28)	0.976(2)	0.975(3)	0.943(2)	0.983(11)
Bi2 x	0.4790(11)	0.477(2)	0.486(2)	0.477(2)	0.486(7)
Bi2 y	0.0761(6)	0.0774(7)	0.0778(9)	0.07212(8)	0.078(4)
Bi2 z	0.9745(27)	0.975(2)	0.981(3)	0.990(2)	0.009(11)
W/Nb x	0.0129(17)	0.001(4)	-0.005(3)	-0.02(3)	-0.002(13)
W/Nb y	0.2497(9)	0.250(1)	0.249(1)	0.252(1)	0.250(7)
W/Nb z	0	0	0	0	0
O1 x	0.047(9)	0.080(14)	0.140(23)	0.035(15)	0.026(47)
O1 y	0.136(3)	0.128(3)	0.160(6)	0.134(4)	0.158(17)
O1 z	0.090(9)	0.101(12)	0.030(21)	0.116(13)	0.069(66)
O2 x	0.243(14)	0.235(22)	0.240(35)	0.256(45)	0.327(54)
O2 y	0.016(4)	0.993(6)	0.990(11)	1.003(14)	1.000(11)
O2 z	0.309(13)	0.258(16)	0.288(23)	0.287(22)	0.145(51)
O3 x	0.267(24)	0.271(21)	0.259(81)	0.242(58)	0.256(50)
O3 y	0.501(4)	0.504(6)	0.490(10)	0.510(11)	0.517(9)
O3 z	0.246(13)	0.171(15)	0.241(34)	0.182(32)	0.206(44)
O4 x	0.816(17)	0.809(14)	0.786(21)	0.755(35)	0.781(54)
O4 y	0.229(7)	0.223(3)	0.212(6)	0.205(6)	0.210(18)
O4 z	0.243(23)	0.161(17)	0.338(22)	0.252(35)	0.272(77)
O5 x	0.180(20)	0.274(12)	0.208(21)	0.187(13)	0.204(45)
O5 y	0.256(10)	0.242(5)	0.225(7)	0.251(7)	0.282(17)
O5 z	0.320(20)	0.322(13)	0.342(20)	0.313(13)	0.311(64)
O6 x	0.613(17)	0.604(13)	0.639(20)	0.598(12)	0.570(58)
O6 y	0.367(5)	0.342(3)	0.357(5)	0.359(3)	0.348(16)
O6 z	0.496(32)	0.525(15)	0.472(40)	0.500(17)	0.464(67)

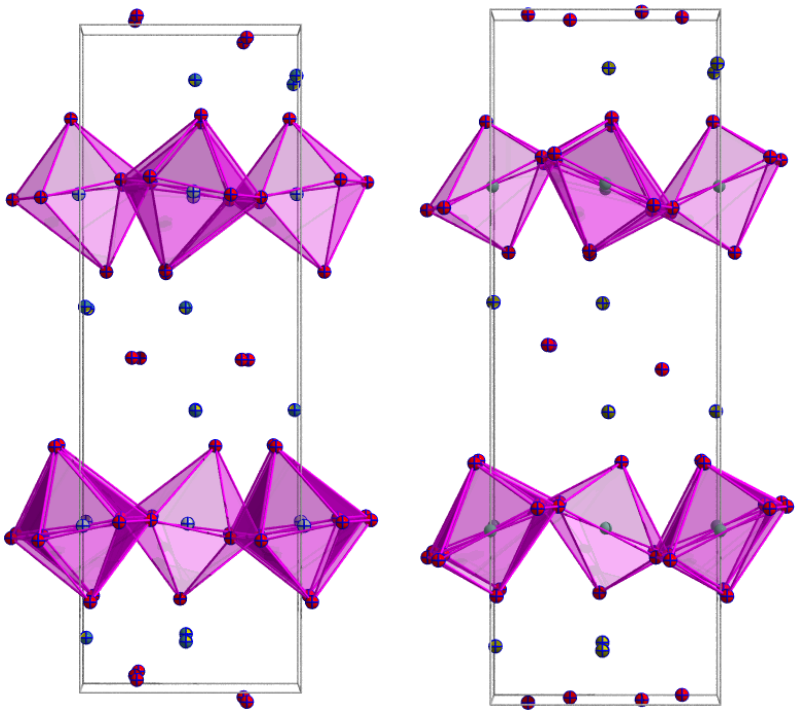

(a) $x = 0$ (b) $x = 0.4$

Figure 5-23: structures of $Bi_2W_{1-x}Nb_xO_{6-x}F_x$ for $x = 0$ and $x = 0.4$. Notice both the change in the octahedra tilt and the displacements of the oxygen sheets in the fluroite layers at $z = 0$.

It appears, therefore, that the addition of fluorine has a similar effect on Bi_2WO_6 as it does on $SrBi_2Nb_2O_9$. With even relatively small proportions of fluorine sharing the oxygen sites the structure starts to resemble the higher symmetry parent phase, and structural indicators of ferroelectricity reduce towards zero.

5.7 Powder Diffraction Conclusions

The powder diffraction experiments performed in this study have shown a number of interesting results. The variable temperature powder diffraction of $SrBi_2Nb_2O_9$ confirmed that the structure nears tetragonality some distance below T_c, and that, when left to refine, the tetragonality goes through a minimum at roughly $T = T_c - 100\,\mathrm{K}$. However, further observations made of the temperature dependence of the width of some selected peaks allowed the correct analysis of this artefact and indicates an effect associated with ferroelastic domain formation around T_c. This

conclusion is chosen over the alternatives—a coexistence of phases or a coincidental equilibrium between cation displacements and oxygen octahedral tilts—due to the persistence of the peak broadening above T_c. With the problem of the orthorhombicity overcome, and the cell constrained to be tetragonal in the region $T_c - 100 \gtrsim T > T_c$, the refinements showed a second order nature, and a structural element was chosen to represent the polarization, namely the displacement of the bismuth cation from its prototypic site.

Powder diffraction of fluorinated $SrBi_2Nb_2O_9$ showed the formation of a second phase with increased fluorination, that was unindexable. This was combined with a reduction in the quality of the patterns from the Aurivillius phase, consisting of a reduction in diffracted intensity and an increase in the peak widths. As a result, the refinements also reduced in quality of fit with increased fluorination, but did show a movement of many of the atoms toward their prototypic sites, and hence toward the the prototypic structure as a whole. The refined disorder on the strontium site also increased with fluorination, leading to the conclusion that the local defect structure introduced to accommodate the lower valency F^- ions on the O^{2-} site understandably involved the introduction of the higher valence Bi^{3+} on the Sr^{2+} site. The powder diffraction data of $Bi_2W_{1-x}Nb_xO_{6-x}F_x$ was of lower quality, yet the same trends could be observed as in $Sr_{1+x}Bi_{2-x}Nb_2O_{9-x}F_x$. With increased fluorination came a reduction in the orthorhombicity, and the structure appears to move toward the monoclinic prototypic phase. However, due to the quality of the data collection, it is difficult to assert much about the nature and movement of the oxygen octahedra.

The neutron diffraction of $CsBiNb_2O_7$ showed, for the first time, some experimental evidence of a high temperature structural phase transition, albeit a very subtle change in some of the oxygen site co-ordinates. Since attempts at indexing the high temperature phase in a higher symmetry space group—because any expected phase transition would be to higher symmetry—were unsuccessful, it is concluded that this transition is isosymmetric, and hence may not even be classifiable as a structural phase transition as a result. It is difficult to draw conclusions on the nature of the transition given that the model is refined from powder diffraction, and so a variable temperature single-crystal experiment would greatly help

to increase the validity of the conclusions made.

References

[1] S. M. Blake, M. J. Falconer, M. McCreedy, and P. Lightfoot, J. Mater. Chem. **7**, 1609 (1997).

[2] A. Snedden, K. S. Knight, and P. Lightfoot, Journal of Solid State Chemistry **173**, 309 (2003).

[3] Y. Shimakawa, Y. Kubo, Y. Tauchi, T. Kamiyama, H. Asano, and F. Izumi, Applied Physics Letters **77**, 2749 (2000).

[4] A. Snedden, C. H. Hervoches, and P. Lightfoot, Phys. Rev. B **67**, 092102 (2003).

[5] R. E. Newnham, R. W. Wolfe, and J. F. Dorrian, Materials Research Bulletin **6**, 1029 (1971).

[6] R. Goff, D. Keeble, P. A. Thomas, C. Ritter, F. D. Morrison, and P. Lightfoot, Chemistry of Materials **21**, 1296 (2009).

[7] C. J. Fennie and K. M. Rabe, Appl. Phys. Lett. (USA) **88**, 262902 (2006).

[8] N. A. McDowell, K. S. Knight, and P. Lightfoot, Chemistry - A European Journal **12**, 1493 (2006).

Chapter 6

Dielectric Properties of Ceramics

Preface

As the principle motivation behind this study is the development both of our understanding and the current technology of ferroelectrics, much of the study focused on the ferroelectric properties, which were examined using dielectric impedance spectroscopy. As discussed in §2.4, a ferroelectric phase transition is accompanied by a peak in the dielectric constant. This can be thought of as a "softening" of phonon modes of the crystal near the transition where the energy required to switch the polarisation is significantly lower than far from the transition, and hence yields a higher dielectric constant. This section deals with measurements of the dielectric constant of some of the materials in this study.

6.1 Experimental Details

A bespoke sample rig constructed in house was utilised for all non ambient measurements of dielectric constant. A HP4192A impedance analyser, utilising the four-point contact method, was connected to the sample *via* BNC cables and inconel rods, in areas where the temperature would be raised. The whole rig was lowered into a vertical tube furnace, and suspended from above at the optimum height for thermal homogeneity. As well as the built-in furnace thermocouple, another was added as close to the sample as was possible, and it was this that was used for measuring the actual temperature at the sample throughout the experiment. Small ceramic spacers were used at the junction of the stainless steel shield tubes and the bottom electrode to insulate the electrode from ground. An annotated photograph is shown in figure 6-1.

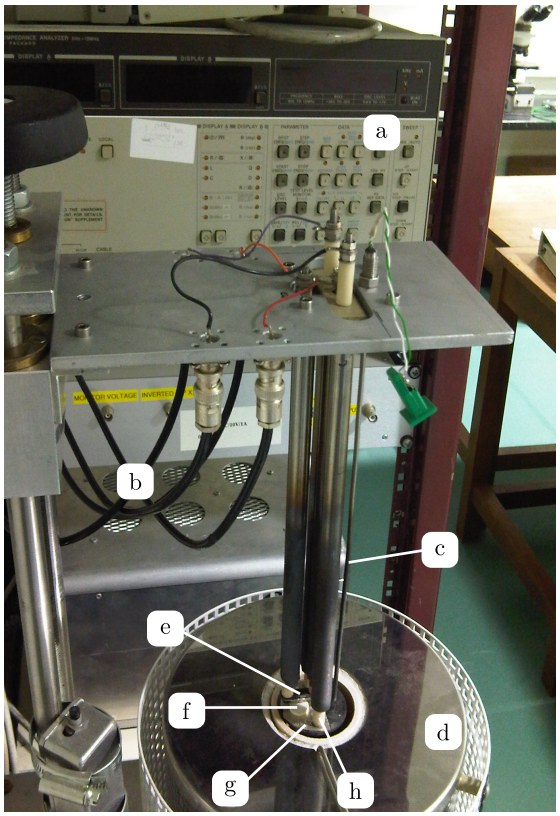

Figure 6-1: The dielectric constant measurement apparatus, in the raised position, including HP4192A analyser (a); four BNC connection cables (b); sample thermocouple (c); furnace (d); upper Pt electrode (e); sample (f); lower Pt electrode (g); and ceramic spacers (h).

6.2 $Sr_{1+x}Bi_{2-x}Nb_2O_{9-x}F_x$

To study the effect of fluorination on the phase transition in $SrBi_2Nb_2O_9$, dielectric constant measurements were performed. In order to perform these measurements on materials of the $Sr_{1+x}Bi_{2-x}Nb_2O_{9-x}F_x$ series, disks nominally 12 mm in diameter and 1 mm in thickness were fabricated *via* uniaxial pressing of the powders at room temperature and sintering. Electrodes were applied by way of a silver conductive paint (RS components 186-3600) painted on the two flat faces. The capacitance and conductance were measured as a function of temperature at frequencies f =10 kHz, 20 kHz, 30 kHz, ..., 100 kHz. These were computed by the impedance analyser assuming an equivalent circuit of a resistor and capacitor in parallel. The real and imaginary parts of the dielectric constant for $Sr_{1+x}Bi_{2-x}Nb_2O_{9-x}F_x$can be seen in figures 6-2 and 6-3 respectively. The variation with temperature of the

dielectric constant of the end member, $SrBi_2Nb_2O_9$, is in good agreement with previous work [1–3]. The change in the real part of the dielectric constant, ϵ', with increasing x (figure 6-4 is consistent with a reduction of the ferroelectricity in the sample. No substantial change in temperature of the dielectric anomaly is seen over the range of compositions studied, suggesting that the transition either disappears completely (*i.e.* the room temperature structure persists to high temperatures) or remains, with no dielectric anomaly associated with it. The continuous nature of the reduction in intensity of the anomaly, however, suggest that the latter is true, if one assumes that the material is homogeneous in composition. The overall picture given by the variation of ϵ' with composition and temperature is that with increased fluorination the dielectric anomaly is reduced, due to the overall reduction in the polarisation of the structure. This is in keeping with the structural refinements as seen in §5.4, which indicate the growth of a new phase with increased fluorination. From the dielectric measurements, we can say that this new phase is not ferroelectric. It is unclear whether all the added fluorine forms this new phase, with the net reduction in ϵ' due only to the reduction in fractional density of pure $SrBi_2Nb_2O_9$, or whether some fluorine combines with the $SrBi_2Nb_2O_9$ subtly to alter the ferroelectric behaviour. The peak temperature does reduce slightly with increased composition, implying the latter is true. The imaginary part of the dielectric constant, ϵ'', and its influence on the value of the dielectric loss tangent in figure 6-5 also shows us that with increased fluorine content the $Sr_{1+x}Bi_{2-x}Nb_2O_{9-x}F_x$ pellet becomes more conductive. The general trend of increased $\tan(\delta)$ with temperature results from increased conductivity, and the results show that this high temperature conductivity increases substantially with relatively small amounts of added fluorine.

6.3 $\mathbf{Ba_{1+x}Bi_{2-x}Nb_2O_{9-x}F_x}$

$BaBi_2Nb_2O_9$ is a well known example of a relaxor ferroelectric [4–6], as it exhibits a diffuse dielectric anomaly, the temperature of which is dependent on the frequency of the applied field. The origin of this behaviour has been well debated in the literature, with the majority agreeing that $BaBi_2Nb_2O_9$ contains polar nanodomains of

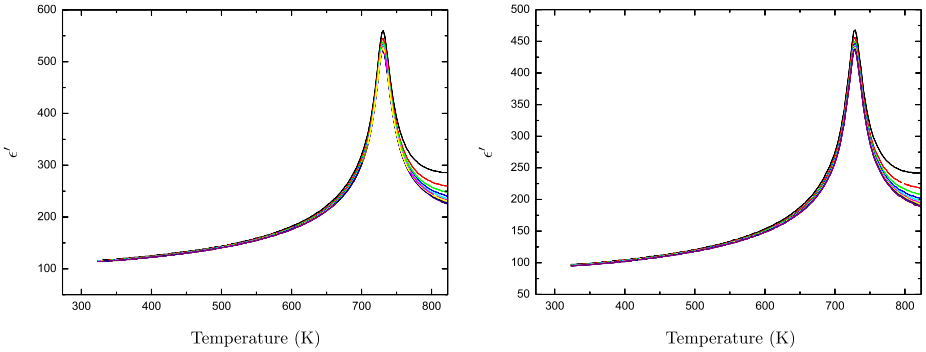

(a) SBN

(b) SBN-F0.05

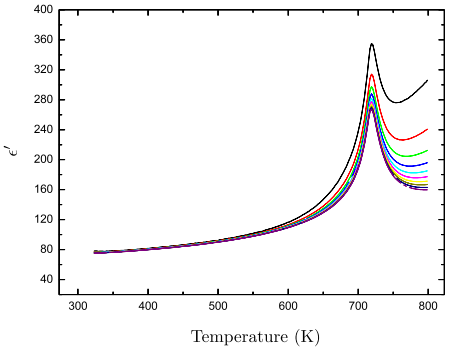

(c) SBN-F0.1

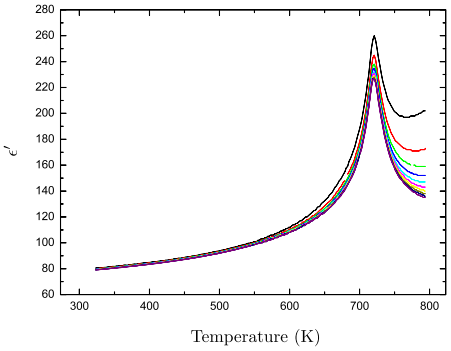

(d) SBN-F0.15

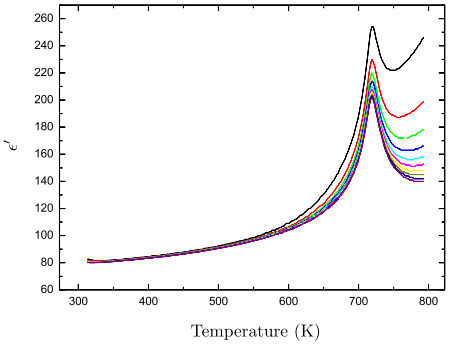

(e) SBN-F0.2

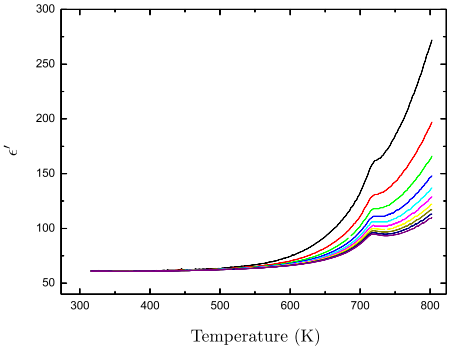

(f) SBN-F0.4

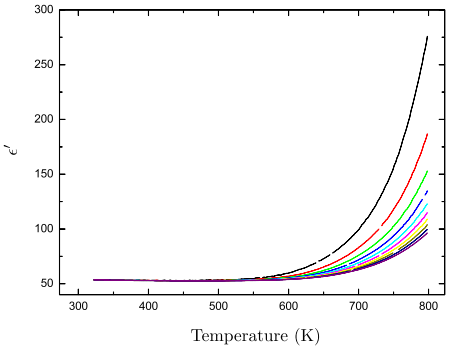

(g) SBN-F0.6

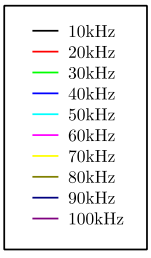

Figure 6-2: Real part of the dielectric constant, ϵ' of $Sr_{1+x}Bi_{2-x}Nb_2O_{9-x}F_x$ as a function of temperature and frequency for x = 0 (a); 0.05 (b); 0.1 (c); 0.15 (d); 0.2 (e); 0.4 (f); and, 0.6 (g).

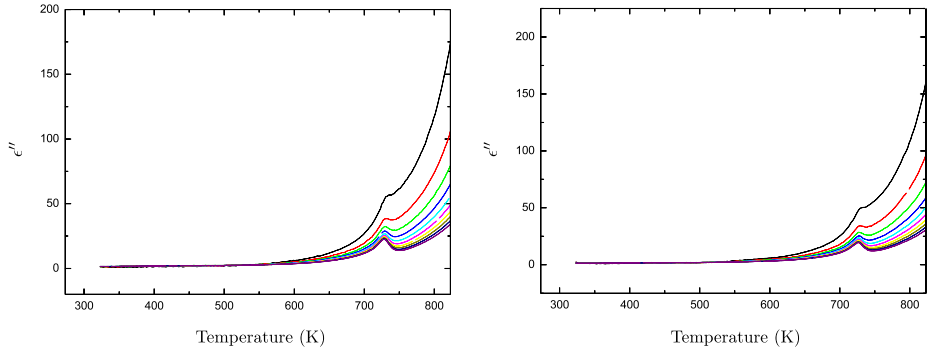

(a) SBN

(b) SBN-F0.05

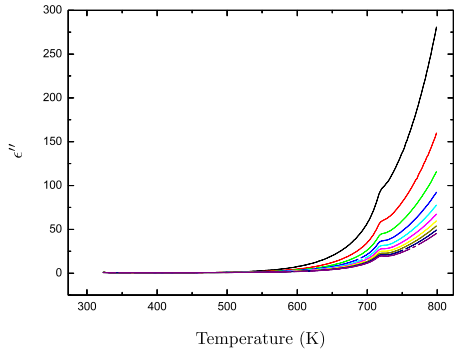

(c) SBN-F0.1

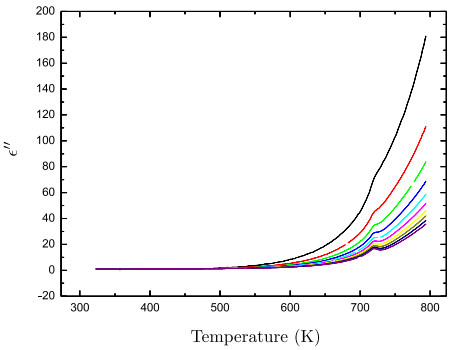

(d) SBN-F0.15

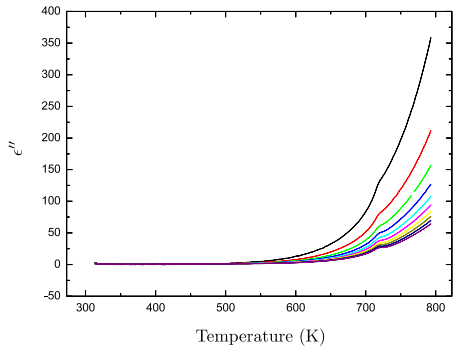

(e) SBN-F0.2

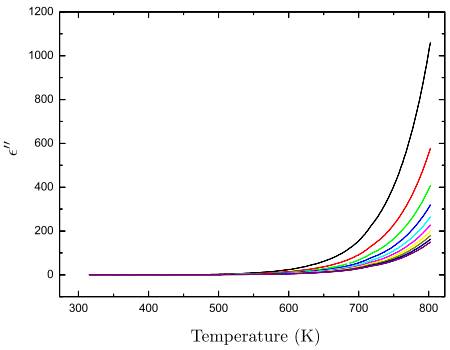

(f) SBN-F0.4

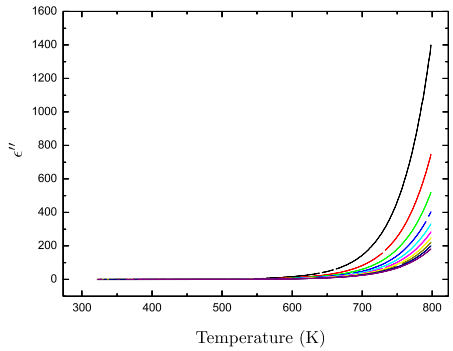

(g) SBN-F0.6

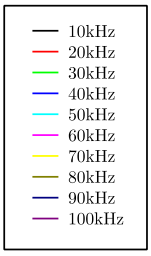

Figure 6-3: Imaginary part of dielectric constant, ϵ'' as a function of temperature and frequency for $Sr_{1+x}Bi_{2-x}Nb_2O_{9-x}F_x$ with x = 0 (a); 0.05 (b); 0.1 (c); 0.15 (d); 0.2 (e); 0.4 (f); and, 0.6 (g).

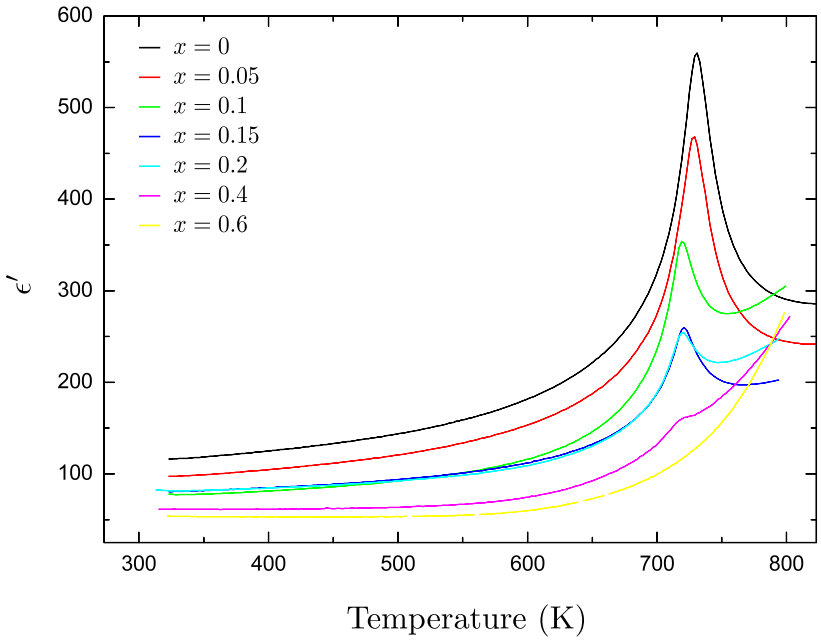

Figure 6-4: Plot of the dielectric constant for a range of compositions of $Sr_{1+x}Bi_{2-x}Nb_2O_{9-x}F_x$ at 10 kHz. The dielectric anomaly associated with the phase transition in $SrBi_2Nb_2O_9$ can clearly be seen to reduce in significance with increasing fluorine content, x. At $x = 0.6$, the peak has completely disappeared.

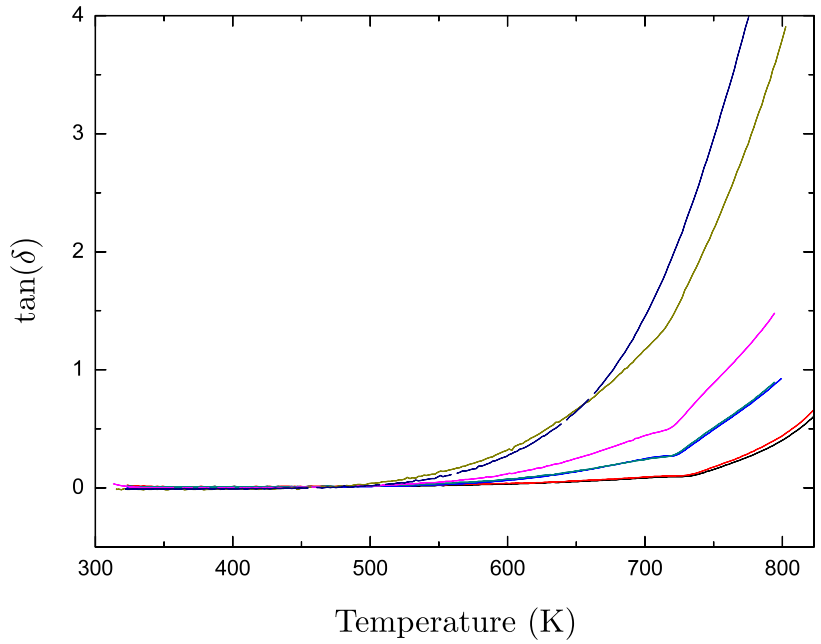

Figure 6-5: Plot of the dielectric loss tangent, $\tan(\delta) = \epsilon''/\epsilon'$, as a function of temperature at 10 kHz in $Sr_{1+x}Bi_{2-x}Nb_2O_{9-x}F_x$.

orthorhombic distortion from the average (centrosymmetric) tetragonal structure, as is the case for the archetypal relaxor $Pb(Mg_{1/3}Nb_{2/3})O_3$[7–9]. The structure of $BaBi_2Nb_2O_9$ is discussed in §3.4. Pellets of 12mm diameter and approximately 1mm thickness were uniaxially pressed from the as-made powders at room temperature and sintered to increase density. The compositions $x = 0, 0.15, 0.2, 0.4$ and 0.6 were successfully pelleted, and electrodes were applied using the same method as detailed above for $Sr_{1+x}Bi_{2-x}Nb_2O_{9-x}F_x$. The real and imaginary dielectric spectra are shown in figures 6-6 and 6-7. Upon first inspection the addition of fluorine to $BaBi_2Nb_2O_9$ has the same effect as it does to $SrBi_2Nb_2O_9$: increased fluorine content leads to a diminished dielectric anomaly. Of particular interest in this system, however, is the effect of the composition on the degree of relaxation.

The effect of composition on the temperature of the dielectric maxima, T_{max}, for frequencies of 10 kHz and 100 kHz is shown in figure 6-8. A clear correlation is seen between the effect on both these frequencies, suggesting that the addition of fluorine does not affect the degree of frequency dispersion of the transition in this material. However, in contrast with the effect on $SrBi_2Nb_2O_9$, where a new, non-ferroelectric phase seems to form and there is only a minimal effect on the temperature of the transition, the addition of fluorine to $BaBi_2Nb_2O_9$ has a noticeable effect on T_{max}. When one considers the differences in the structural origins of ferroelectricity in the classical ferroelectric $SrBi_2Nb_2O_9$ and the relaxor $BaBi_2Nb_2O_9$, this is most likely explained by domain effects. Whereas the relatively uniform domains of $SrBi_2Nb_2O_9$ (in structure, at least) are predominantly uninfluenced by the fluorine, the addition of fluorine to the existing polar nano-domains in $BaBi_2Nb_2O_9$enhances the relaxor effect. Our hypothesis is, therefore, that the doping with fluorine serves to emphasize the difference between the classical Sr-based ferroelectric and the relaxor Ba-based isomorph. The new phase that forms on increased fluorination of the Sr-based isomorph has little effect, other than to diminish the overall signal, as this phase is perceived to be non-ferroelectric.

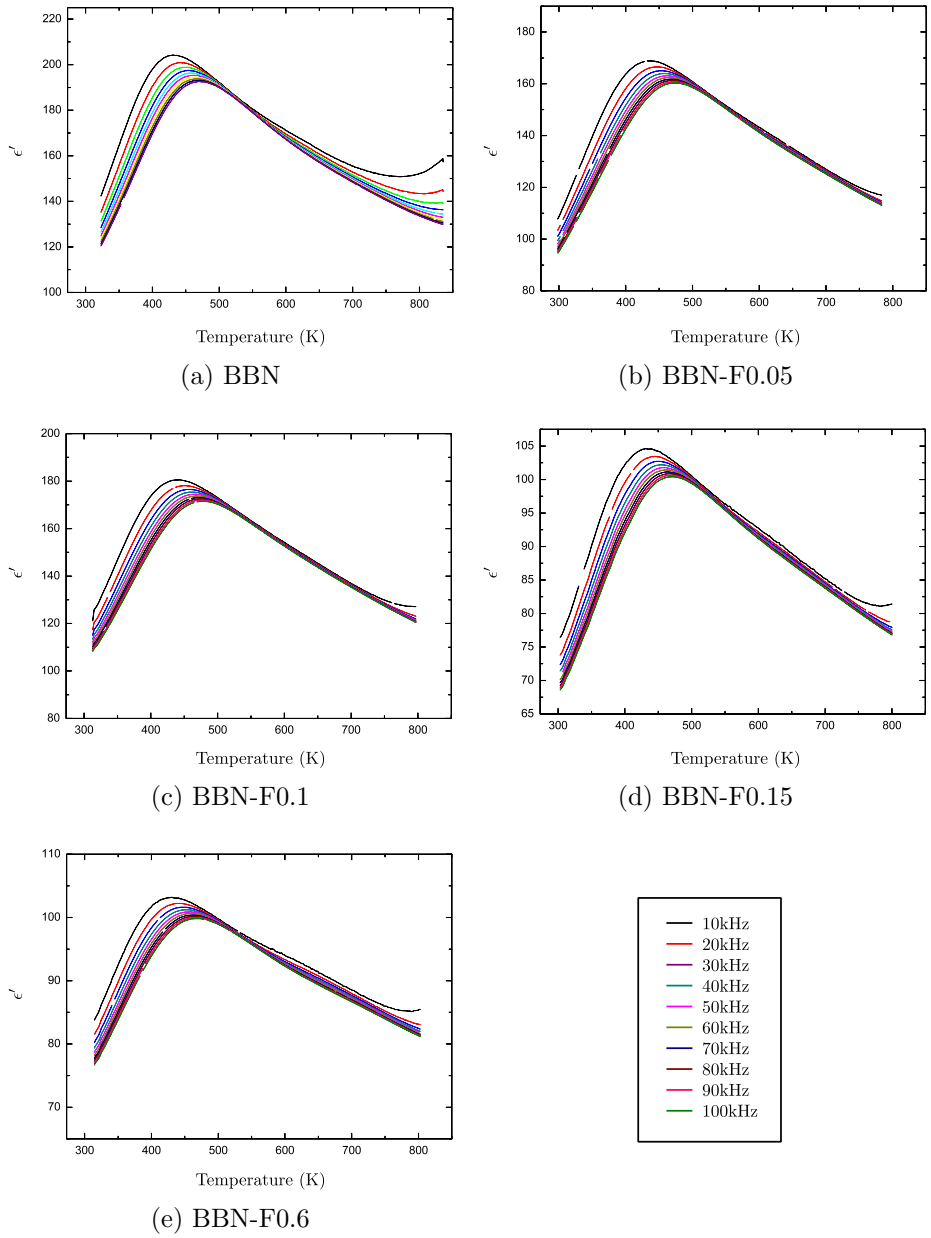

(a) BBN (b) BBN-F0.05

(c) BBN-F0.1 (d) BBN-F0.15

(e) BBN-F0.6

Figure 6-6: Real part of the dielectric constant, ϵ' of $Ba_{1+x}Bi_{2-x}Nb_2O_{9-x}F_x$ as a function of temperature and frequency with x = 0 (a); 0.15 (b); 0.2 (c); 0.4 (d); and, 0.6 (e).

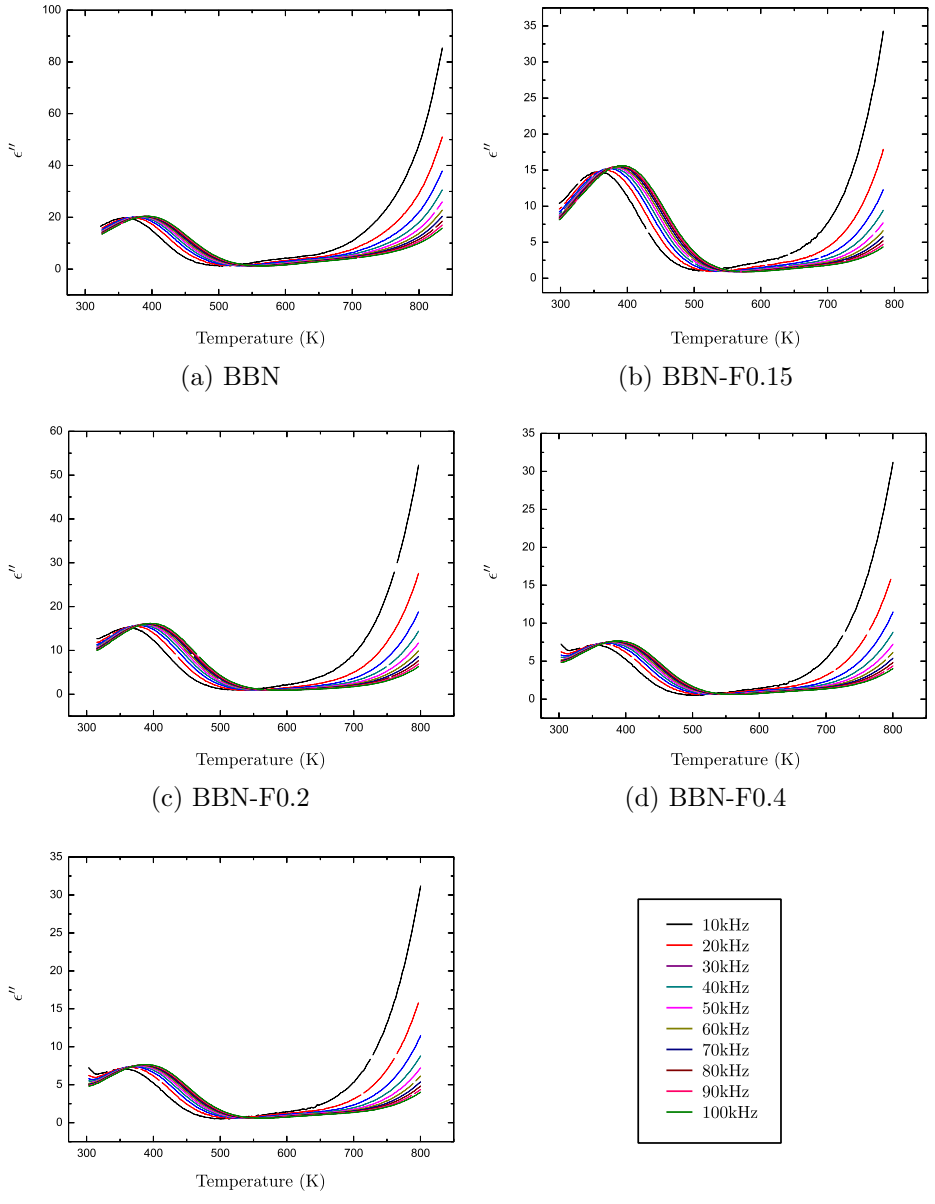

(a) BBN (b) BBN-F0.15

(c) BBN-F0.2 (d) BBN-F0.4

(e) BBN-F0.6

Figure 6-7: Imaginary part of dielectric constant, ϵ'' as a function of temperature and frequency for x = 0 (a); 0.15 (b); 0.2 (c); 0.4 (d); and, 0.6 (e).

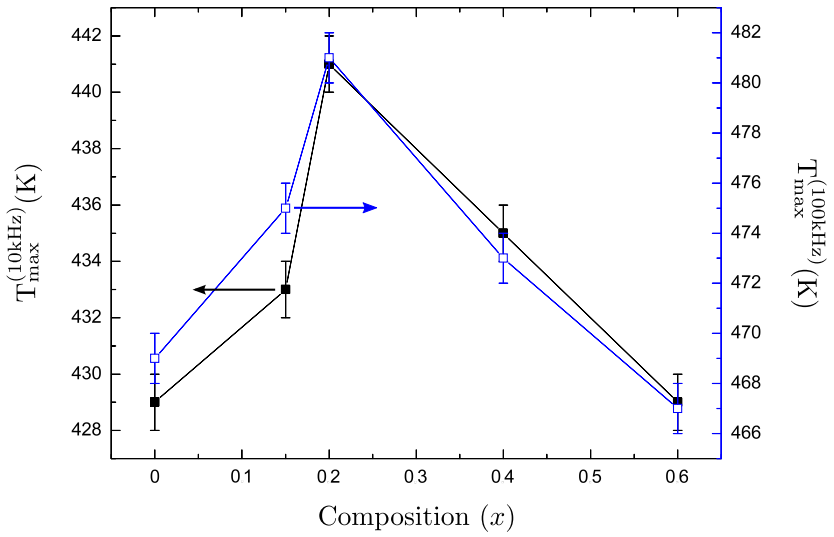

Figure 6-8: The variation of the temperature of the maximum of the dielectric constant T_{max} at 10 kHz and 100 kHz as a function of composition in $Ba_{1+x}Bi_{2-x}Nb_2O_{9-x}F_x$. Whilst the addition of fluorine does effect the temperature of the maximum, it seems to effect all frequencies similarly.

6.4 Dielectric Properties Conclusions

Fluorine was added to both a classical ferroelectric and relaxor ferroelectric Aurivillius parent material, and the effect of the substitution on the dielectric behaviour was measured. The hypothesis of Ravez and Simon [10] was that the substitution of fluorine onto an oxygen site in a classical ferroelectric oxide could drive a cross-over from classical to relaxor behaviour, and this hypothesis was tested on $SrBi_2Nb_2O_9$. The results show a distinct decrease in the dielectric anomaly associated with the ferroelectric phase transition, which could be consistent either with the introduction of another, non-ferroelectric phase (and hence the *amount* of ferroelectric material in the sample being reduced); a very significant change in the T_c of some of the material under study; or the modification of the parent structure as such to reduce the dielectric anomaly associated with the ferroelectric transition. Since no substitute dielectric anomaly is observed over the entire temperature range studied, it is concluded that rather than shifting the T_c of the ferroelectric behaviour, the dielectric anomaly is systematically reduced by the introduction of fluorine onto the oxygen site. Furthermore, the reduction in intensity is not accompanied by any dispersion of the peak of the dielectric anomaly with frequency—the defining characteristic of relaxor behaviour—and hence the nature of the phase transition is not altered from the original classical behaviour.

The dielectric behaviour of the fluorinated versions of $BaBi_2Nb_2O_9$ were studied, to investigate the affect of fluorination on a material that already exhibits relaxor behaviour. The same observation was made in this system as in the classical $Sr_{1+x}Bi_{2-x}Nb_2O_{9-x}F_x$; namely the systematic reduction in intensity of the dielectric maxima with increased fluorine content. With this observation common to both the series studied, it seems to indicate that if properties are truly to be tailored *via* the introduction of fluorine, the level of dopant would have to be appreciably small to ensure that the desired ferroelectric properties are not destroyed as a result. The degree of relaxation also seemed to be unchanged in $Ba_{1+x}Bi_{2-x}Nb_2O_{9-x}F_x$, although the temperatures of the dielectric maxima themselves seemed to vary as a function of temperature, with a maximum T_{max} being measured at the $x = 0.2$ composition.

References

[1] H. Gu, J. M. Xue, X. Gao, and J. Wang, in *Mater. Chem. Phys. (Netherlands)* (2002), vol. 75, pp. 105 – 9.

[2] M. Dong and R. Gerhardt, in *1998 Annual Report Conference on Electrical Insulation and Dielectric Phenomena* (1998), vol. 1, pp. 327 – 30.

[3] B. H. Venkataraman and K. B. R. Varma, J. Mater. Sci., Mater. Electron. (USA) **16**, 335 (2005).

[4] D. Nuzhnyy, S. Kamba, P. Kuzel, S. Veljko, V. Bovtun, M. Savinov, J. Petzelt, H. Amorin, M. E. V. Costa, A. L. Kholkin, et al., Phys. Rev., B, Condens, Matter Mater. Phys. **74**, 134105 (2006).

[5] R. Z. Hou, X. M. Chen, and Y. W. Zeng, J. Am. Ceram. Soc. **89**, 2839 (2006).

[6] P. Keburis, J. Banys, A. Brilingas, J. Prapuolenis, A. Kholkin, and M. E. V. Costa, J. Nanosci. Nanotechnol. **353**, 149 (2007).

[7] N. de Mathan, E. Husson, G. Calvarn, J. R. Gavarri, A. W. Hewat, and A. Morell, J. Phys., Condens. Matter. **3**, 8159 (1991).

[8] J. de Los S. Guerra, M. H. Lente, and J. A. Eiras, J. Eur. Ceram. Soc. **27**, 4033 (2007).

[9] Z. G. Lu and G. Calvarin, Phys. Rev. B **51**, 2694 (1995).

[10] J. Ravez and A. Simon, J. Solid State Chem. **3**, 260 (2001).

Chapter 7

Discussion, Conclusions, and Suggestions for Further Study

Preface

The discussion of the results, the conclusions that are drawn, and the subsequent suggestions for further study, are organized within this chapter by material.

7.1 $SrBi_2Nb_2O_9$

The room temperature structure of $SrBi_2Nb_2O_9$ was confirmed *via* both powder and single-crystal x-ray diffraction. The single crystal study gave an R_{obs} of 5.91 on data collected to 0.5 Å, and the refined structure was in agreement with those suggested previously from powder studies [1, 2]. This relatively low value of R_{obs}, however, was dependent on the introduction of cation disorder between the A-site cation (in this case, Sr), and the bismuth site in the fluorite layer, since this yielded a reduction in R_{obs} from 8.75. The refined site occupancy factors (SOF) for the cation sites are reproduced in table 7-1. Since the composition was not constrained to stoichiometry in this refinement, a refined composition of $Sr_{1.009}Bi_{1.991}Nb_2O_9$ was also found. Whilst it was the observation of Ismunandar and Kennedy [3] that around 20% substitution was allowed between the two sites without any significant effect on the structure, these refinements suggest that values of up to 27.5% substitution are possible. The room-temperature powder data were also refined satisfactorily, and resulted in a model very similar to that refined from the single crystal data. In the powder refinement, the overall stoichiometry was constrained to ensure physically realistic results, and observed from these refined occupancies is that the single-crystal refinement suggests a slightly larger degree

Table 7-1: Refined cation occupancies for $SrBi_2Nb_2O_9$ from refinements of single-crystal and powder diffraction data

Site	Cation	Refined SOF (single-crystal)	Refined SOF (powder)
Sr	Sr	0.725(6)	0.765(3)
	Bi	0.275(6)	0.235(3)
Bi	Bi	0.858(7)	0.882(2)
	Sr	0.142(7)	0.118(2)

of disorder than the powder counterpart. This is either because; (i) the single-crystal refinement is simply a more accurate reflection of the actual structure and the powder systematically underestimates the disorder, (ii) the single crystal does contain a larger degree of cation disorder because of the different synthesis method, or (iii) the relative occupancies were skewed by the constraint of fixed stoichiometry. It is difficult to discount any of these possibilities using the data collected in this study.

Variable-temperature powder x-ray diffraction experiments on $SrBi_2Nb_2O_9$ were performed to examine the structure closely through the phase transition, with the aim of plotting a structural element that represents the order parameter. The relatively low orthorhombicity, $o = 2(\boldsymbol{a}-\boldsymbol{b})/(\boldsymbol{a}+\boldsymbol{b})$, means that even at room-temperature, the $\boldsymbol{a}$ and $\boldsymbol{b}$ lattice parameters can be difficult to refine, and this becomes even more of a problem as T_c is approached and the orthorhombicity consequently drops to zero. Studies of the full-width-at-half-maximum of the *315* and *135* peaks—which almost fully overlap—highlighted this problem, showing that a broadening effect which occurs around the phase transition leads to physically unrealistic refined values of $\boldsymbol{a}$ and $\boldsymbol{b}$, and the resulting orthorhombicity. Even a marginal broadening of the peaks led to relatively large changes in the refined $\boldsymbol{a}$ and $\boldsymbol{b}$ lattice parameters, and so for powder patterns where the orthorhombic tilt peaks were not observable, the patterns were refined as tetragonal. The broadening of the *315* and *135* peaks was not due to thermal or compositional inhomogeneities, since the broadening persists to high temperatures where the orthorhombic peaks are not observed. This argument also discounts the possibility of the broadening being caused by the existence of a coexistence region, resulting from a first-order phase transition. Our conclusion is that as the ferroelectric

structure approaches T_c, and the orthorhombicity approaches zero, nano-domains begin to form, and that the diffraction peaks are then broadened by the relatively large density of the associated domain walls. This broadening persists beyond T_c, since the domain walls will not disappear immediately upon the crystal becoming isotropic across them. What is clear from the experiments performed solely on this peak (figure 5-10a) is that the peak positions do move substantially in the region of the broadening, and so the refined changes in $\boldsymbol{a}$, $\boldsymbol{b}$ and $\boldsymbol{c}$, are ostensibly correct.

It is suggested that the Bi y-displacements are a good representation of the order parameter when the refinements are of x-ray data, since the suggestion by Newnham et al. [4] was that the apical oxygen is the overall best measure of the order parameter. The form of the Bi y-displacement is suggestive of a 2nd-order-dominated phase transition, since $\frac{\partial \Delta y_{(\mathrm{Bi})}}{\partial T}$ appears to be continuous.

The birefringence study shows a Δn *vs.* temperature which is not characteristic of a purely ferroelectric or ferroelastic phase transition. Close to the transition, we observe that Δn has a critical exponent of 0.94 ± 0.04, and this result being very close to 1 means that in this region, to a close approximation, $\Delta n \propto T_c - T$. In the region further from the phase transition a different behaviour is observed, *i.e.* the critical exponent is 0.43 ± 0.03. This relates to an approximate behaviour of $\Delta n \propto (T_c - T)^{1/2}$.

Upon comparison of the birefringence of $SrBi_2Nb_2O_9$ with that of $SrBi_2Ta_2O_9$, it is seen that $SrBi_2Ta_2O_9$ clearly exhibits two distinct transitions, which can be modelled separately. The experiment on $SrBi_2Ta_2O_9$ serves to demonstrate the applicability of birefringence microscopy to characterizing phase transitions, and its ability to solve individually the contribution from strain and polarization in a ferroelectric sample.

A comparison of the Bi y–displacement and the birefringence is shown in figure 7-1. The difference in the temperatures where these measurements attain zero is most likely caused by incorrect thermal calibration in one or both of the furnaces used. The results of the birefringence indicated that the there were two regions of temperature, each with its own characteristic temperature dependence. The values of the critical exponents in these regions also suggested the dominant

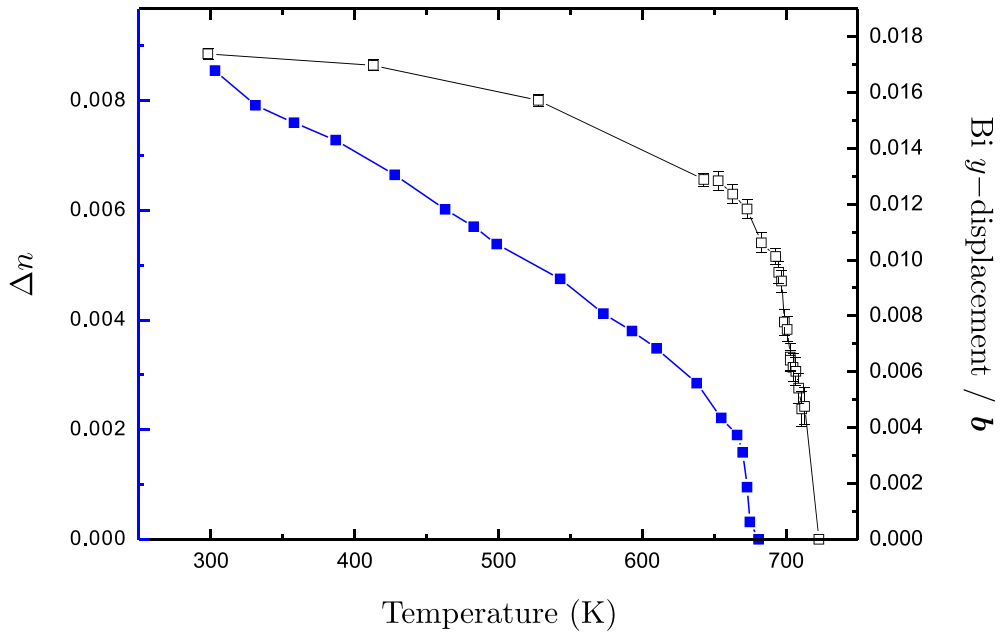

Figure 7-1: Comparison of the forms of the Bi y−displacement, from powder x-ray diffraction, and the birefringence Δn in $SrBi_2Nb_2O_9$.

mechanism behind the variation in Δn. Equation 4-2 showed the dependence of Δn on the polarization and the strain:

$$\Delta n = n_e - n_o = k_1 P_s^2 + k_2 \epsilon \tag{7-1}$$

and so we concluded that if polarization is dominant, the real critical exponent will be half that which is measured, or conversely, where polarization is dominant, a critical exponent of 1 should be measured. This meant that the observed data suggested the region close to the phase transition should be dominated by polarization. The refinement of the Bi y−displacement shows that the Bi atom does not move linearly with temperature, rather that it initially moves quickly as the material is cooled, and then slows as the temperature continues to fall. This observation, coupled with the temperature dependence of the orthorhombicity, as shown in figure 5-7, which shows us that the strain will continue to rise at a constant rate as the temperature falls, indicate that the analysis of the birefringence study is correct. It is also possible to further manipulate the combined birefringence and powder diffraction data to reveal the strain within the material, especially since the strain is so difficult to measure with powder diffraction in this system, where the orthorhombicity is so low. Since we know that the birefringence should

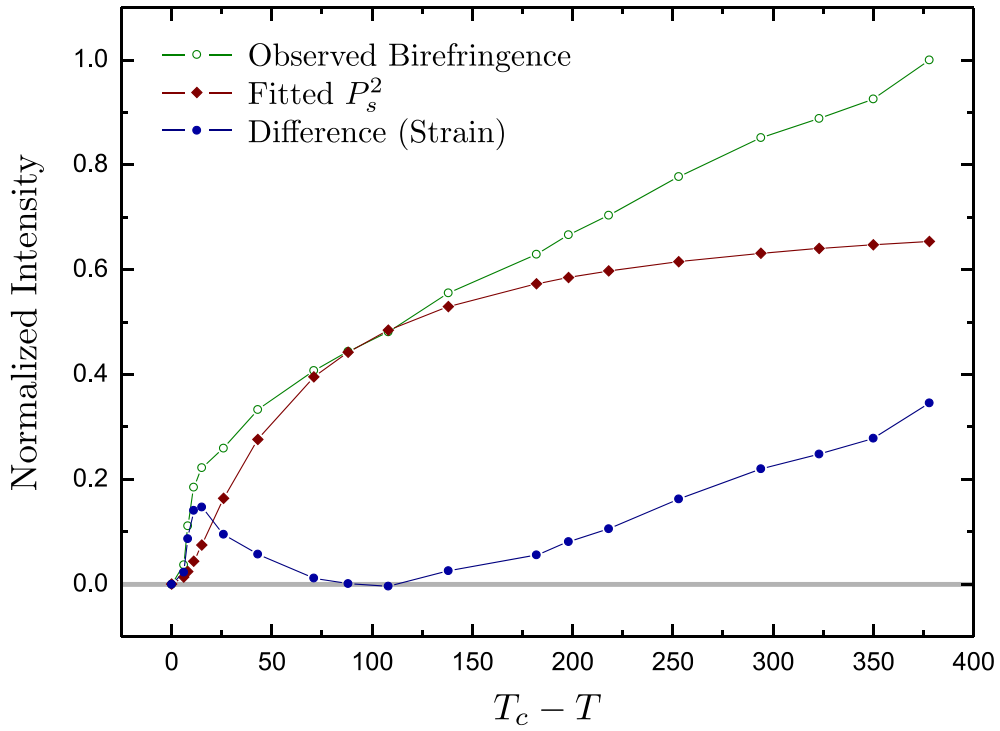

Figure 7-2: Subtracting a "polarization function" from the observed birefringence yields the residual birefringence, which is most likely to be explained by strain. The polarization function is simply a function fitted to the refined polarization data from powder diffraction.

just be a linear combination of strain and polarization squared, it is possible to subtract the polarizations' contribution from the overall birefringence to leave the birefringence that results from the strain. The results from this process are shown in figure 7-2. This figure shows that there is a large amount of birefringence that is unaccounted for very close to the phase transition; within $0 < T_c - T < 20$. This value then falls away to a value of zero difference, and hence zero strain, corresponding to the minima in the graph of the full-with-at-half-maximum of the *315/135* doublet from the powder diffraction (figure 5-10b). This observation also corresponds to the refined values of the lattice parameters from the powder diffraction (figure 5-7), which shows a negligible distortion from the tetragonal cell over a 100 K range below T_c. All of these results indicate that there exists a region in temperature where domain wall formation occurs more freely, and the resulting strain fields lead to an increased observed birefringence.

Suggestions for Further Study

Whilst this study has gone some way toward fully characterizing the phase transition in $SrBi_2Nb_2O_9$, further insights could be gained from performing low temperature diffraction to plot the lattice parameters, and hence measure the variation of the strain with temperature. This would allow a full comparison of the structure and the birefringence to be made, in an area where the measurement of the orthorhombicity is significantly more accurate. Another possibility would be to use high resolution synchrotron diffraction to characterize fully the nano-domain peak broadening effect, and hence enabling the refinement of the lattice parameters near the phase transition.

A variable-temperature single-crystal synchrotron study would be very powerful in refining the atomic displacements and lattice parameters, and would possibly demonstrate further evidence for the existence of nano-domains close to the phase transition. Even a synchrotron experiment performed on a ground single crystal, may also reveal the source of the discrepancy between the refined Sr/Bi disorder from single-crystal and powder diffraction.

Neutron diffraction, on both powders and single crystals, would allow for a significantly more reliable refinement of the apical oxygen site, as originally suggested by Newnham et al. [4].

Variable temperature ^{93}Nb NMR could also help to ascertain the chemistry and symmetry of the Nb site across the phase transition, especially when performed as part of a larger study on several isomorphous materials. ^{93}Nb NMR is a highly sensitive tool for investigating the short-range order and local structure, and so would also show evidence for the formation of nano-domains around the phase transition.

7.2 $BaBi_2Nb_2O_9$

Single-crystal diffraction was performed on $BaBi_2Nb_2O_9$ to supplement the wealth of powder x-ray and neutron diffraction that exists in the literature [1, 3, 5, 6]. Initially, the data were integrated on the basis of a tetragonal cell, and the resulting refinement was not satisfactory, suggesting that part of the model was incorrect.

The addition of cation mixing to the model did improve the refinement but did not make it satisfactory, and the refined occupancies, as shown in table 3-3, were 0.535 and 0.737 for the Ba and Bi sites respectively.

The refined values of the occupancy were significantly higher than had been previously reported from powder diffraction, and showed a similar trend to that which was observed in the experiments on $SrBi_2Nb_2O_9$, *i.e.* larger refined cation mixing from single crystal diffraction than from powder diffraction. This infers, therefore, that this observation is characteristic of the experiment and refinement, but may still be correct. Since the refined values of the ADP's and the SOF's are co-dependent, it still stands to reason that these will both be measured more accurately from good-quality single-crystal data than from powder data. For this reason, the ADP's were inspected to ascertain whether the large cation mixing was simply a result of their mutual co-dependence. Inspection of the Fourier difference plots suggested a large discrepancy between the calculated and observed electron density around the Ba and Bi sites that demonstrated 4-fold symmetry, which appeared in the form of "lobes". To ensure the apparent symmetry of these lobes wasn't a result of merging the data in the Laue group $4/mmm$, the data were re-merged in Laue group 1 and the unusual shape of the Ba site remained. Anharmonic atomic displacement parameters were added to the model to allow the observed distribution of density to be accounted for, and this led to a reduction of R_{obs} from 17.72 to 8.97.

The birefringence experiment demonstrated that $BaBi_2Nb_2O_9$ is tetragonal to within 1 part in 10^7, since a birefringence of ~ 0 was measured at room temperature, and this value was independent of temperature. This then supports the Laue group of $4/mmm$ as suggested from the single-crystal refinements.

The dielectric spectroscopy on the $Ba_{1+x}Bi_{2-x}Nb_2O_{9-x}F_x$ series does show that, despite the high symmetry refined from the single-crystal data, $BaBi_2Nb_2O_9$ shows dielectric spectroscopy data typical for a relaxor ferroelectric. Since the diffraction experiments showed an average structure that was centrosymmetic, it is our conclusion that the mechanisms behind the relaxor behaviour is similar to that in $Pb(Mg_{1/3}Nb_{2/3})O_3$, *i.e.* polar domains. Whilst these are observed as micro-domains in $Pb(Mg_{1/3}Nb_{2/3})O_3$, the fact that they are not observed in birefrin-

gence microscopy in $BaBi_2Nb_2O_9$ suggests that in the current case these domains form on the nano-scale. It is a possibility that the features in the electron density around the cations are a direct measurement of the distortion within these domains.

Suggestions for Further Study

A variable-temperature high-resolution synchrotron single-crystal diffraction experiment would provide high-quality data for a more precise refinement of the structure, and would therefore support or refute the observation of features in the observed electron density maps, particularly around the Ba and Bi sites.

^{135}Ba, ^{137}Ba and ^{93}Nb NMR, in the former cases requiring some degree of isotopic enrichment, would allow the direct measurement of the chemical environment of the Ba and Nb sites to discover if evidence for the unusual electron density maps can be observed, and to determine if the observed densities are simply a superposition of four, 90°−rotated twins with a small Ba offset in each, or a real representation of the probability distribution function.

7.3 $CsBiNb_2O_7$

The room-temperature single-crystal study of $CsBiNb_2O_7$ shows both twinning and diffuse scattering, shown in figures 3-6b and 3-6a respectively, which makes the refinement of this data non-trivial. Despite this, the refinement still attains an R_{obs} of 6.54, which means that the model is predominantly correct. Inspection of the Fourier difference plots around the modelled atoms does show a systematic pattern of peaks, with each atom present in the model having a counterpart of smaller intensity. Intuitively, one would look at the existence of an unmodelled twin component in this crystal to explain this, but using just the high angle data (where the separation of the main and twin peaks is large enough to be resolved) still yields these peaks in the Fourier difference plot. The diffuse scattering, which is also not directly modelled in the current study, suggests there exists some disorder in the [001] direction, and we suggest that this disorder is the stacking of two different structures, denoted “A” and “B”. Structure A is that which is modelled in the

refinement, and structure B is that which causes the extra peaks seen in the Fourier difference plot. From the position of these peaks, particularly those of the equatorial oxygen sites, we can suggest that the difference between structures A and B is predominantly a rotation of the octahedra around [001].

The objective of the variable temperature neutron diffraction experiment performed on $CsBiNb_2O_7$ in this study was to investigate the claim of Fennie and Rabe [7] of the predicted existence of ferroelectricity in this material. They also predicted a T_c of 810 K from their calculations, and since no detailed variable-temperature structural study had been performed previously, our experiment was intended to show the existence of structural evidence for a phase transition in this temperature region, or the lack thereof. Although initial analysis of the refined structure did not demonstrate any evidence for a structural phase transition in the temperature region studied, the refinements were repeated using the Rietveld package Topas Academic. Close inspection of the results of these refinements showed that the direction of displacement from the prototypic site of some of the oxygen sites do, in fact, show evidence that could be resulting from the proximity of a phase transition. Whilst the "connecting" apical oxygen shows no real change in its $x - y$ position over the temperature range measured, the other three oxygen sites indicate a change in the temperature region 773K – 873K. The outer apical site—*i.e.* the oxygen site closest to the alkali metal cation layer—shows evidence of a change in the displacement direction from ~[010] to ~[110]. The equatorial oxygen sites also show a change from ~[110] to ~[110], suggesting an overall rotation of the oxygen octahedra, which leave the central oxygen site relatively unaffected. This movement is very subtle, however, and a change of space group at this temperature is not necessary to maintain a good refinement. We therefore suggest the possible existence of a phase transition in the temperature range 773K – 873K, which is most likely isosymmetric.

It is possible that the transition observed in the models refined from the neutron data is connected to the diffuse scattering from the single crystal. Because the diffuse scattering is unobservable in conventional powder diffraction, this connection is only speculative. It is possible that at a temperature between 773K and 873K, it becomes energetically favourable for the second of the two structures (B)

to reform back into structure A. However, without further knowledge of structures A and B, it is impossible to say whether such a transformation should be observed in powder diffraction.

Suggestions for Further Study

A variable-temperature single-crystal diffraction experiment would show unequivocally the thermal evolution of the diffuse scattering, and would also allow for a more rigorous structural refinement at elevated temperatures, to understand fully the structural changes that take effect as the material is heated. The evidence for a phase transition occurring at all is only tentative and as such, the increased information collected in a single crystal experiment would mean that even in the absence of diffuse scattering, a single-crystal experiment would still be beneficial. However, since the diffuse scattering is very weak compared to the Bragg peaks, it may be difficult to observe in single-crystal neutron diffraction, which would be preferred for plotting the oxygen displacements, and so for a diffuse scattering study x-ray diffraction would possibly be the starting point.

Another avenue is modelling of the diffuse scattering, using software such as DISCUS[8], furthermore, a low-temperature single-crystal diffraction experiment would also reveal the possibility of the cause of the diffuse scattering being frozen in, to form extra Bragg peaks caused by the new modulation of the structure. Observing the modulated structure at low temperature, if such a structure exists, would certainly aid in the modelling of the diffuse scattering.

7.4 Fluorination of Aurivillius phases

The powder diffraction experiments on the fluorinated Aurivillius materials $Sr_{1+x}Bi_{2-x}Nb_2O_{9-x}F_x$ and $Bi_2W_{1-x}Nb_xO_{6-x}F_x$ show that as the fluorine concentration is increased, the parent structures reduce in crystallinity, and in the case of $SrBi_2Nb_2O_9$, a new phase is formed. This new phase in unindexable from the diffraction data taken here, and thus remains of unknown structure to date.

Because of the electronic similarity between oxygen and fluorine, it was impossible to discern any site within the parent structures that is preferentially occupied

by the fluorine, if indeed this is the case. An effect on the cation positions was noted though, with a decrease in the Bi y−displacements in both the series studied. Since it is predicted that the bismuth displacement is the main source of the polarization, the structural study predicts that ferroelectricity should decrease with the addition of fluorine. As the orthorhombicity of $SrBi_2Nb_2O_9$ is negligible, and upon fluorination there appears a reduction in crystallinity, no plot of the orthorhombicity could be refined for this series, but the $Bi_2W_{1-x}Nb_xO_{6-x}F_x$ showed a systematic reduction in the orthorhombicity with fluorine content.

The dielectric spectroscopy results show that the prediction of reduced ferroelectricity is indeed the case; there is a systematic reduction in the intensity of the dielectric anomaly associated with the ferroelectric phase transition with the addition of fluorine in $Sr_{1+x}Bi_{2-x}Nb_2O_{9-x}F_x$. The temperature of the anomaly also marginally falls with increased fluorination, from 731 K for $SrBi_2Nb_2O_9$ to 721 K for the $x = 0.2$ composition. Beyond $x = 0.2$, the temperature of the anomaly becomes difficult to measure accurately, because of the the low intensity. An effect on the temperature of the anomaly at any given frequency in $BaBi_2Nb_2O_9$ also seems dependent on x, although a linear trend is not observed, with the temperature peaking at $x = 0.2$.

In conclusion, the fluorination of Aurivillius phases is a difficult process and the samples dramatically reduce in quality with even small concentrations of substituted fluorine. In the case of $SrBi_2Nb_2O_9$ the dielectric peak associated with classical ferroelectric behaviour just reduces in intensity. A small effect on the temperature of the dielectric anomaly is observed which is, however, negligible compared with those that can be achieved with cation substitution. In general, the addition of fluorine seems only to degrade the crystallinity of the material, whilst forcing the structure to move toward that of the high temperature prototype, without significantly affecting the transition temperature. For this reason, on the basis of this study, fluorination is not seen as a helpful mechanism for the tailoring of enhanced ferroelectric behaviour in Aurivillius phases.

References

[1] S. M. Blake, M. J. Falconer, M. McCreedy, and P. Lightfoot, J. Mater. Chem. **7**, 1609 (1997).

[2] A. Snedden, C. H. Hervoches, and P. Lightfoot, Phys. Rev. B **67**, 092102 (2003).

[3] Ismunandar and B. J. Kennedy, J. Mater. Chem. **9**, 541 (1999).

[4] R. E. Newnham, R. W. Wolfe, and J. F. Dorrian, Materials Research Bulletin **6**, 1029 (1971).

[5] E. C. Subbarao, J. Phys. Chem. Solids **23**, 665 (1962).

[6] Ismunandar, B. J. Kennedy, Gunawan, and Marsongkohadi, Journal of Solid State Chemistry **126**, 135 (1996).

[7] C. J. Fennie and K. M. Rabe, Appl. Phys. Lett. (USA) **88**, 262902 (2006).

[8] T. Proffen and R. B. Neder, J. Appl. Cryst. **30**, 171 (1997).

Appendix A

Barium Titanate Recripocal Lattice Images

The *Crysalis* software package from Oxford diffraction was used to form undistorted images of principle lattice planes in reciprocal space. The $h0l$ plane showed splitting in opposite quadrants, and is the subject of discussion in §3.6. Included here for completeness are the $hk0$ and $0kl$ reciprocal lattice planes, which show no such splitting. Although the data collection collecte data to a resolution of 0.4 Å, these precession images only show data to 0.8 Å for clarity.

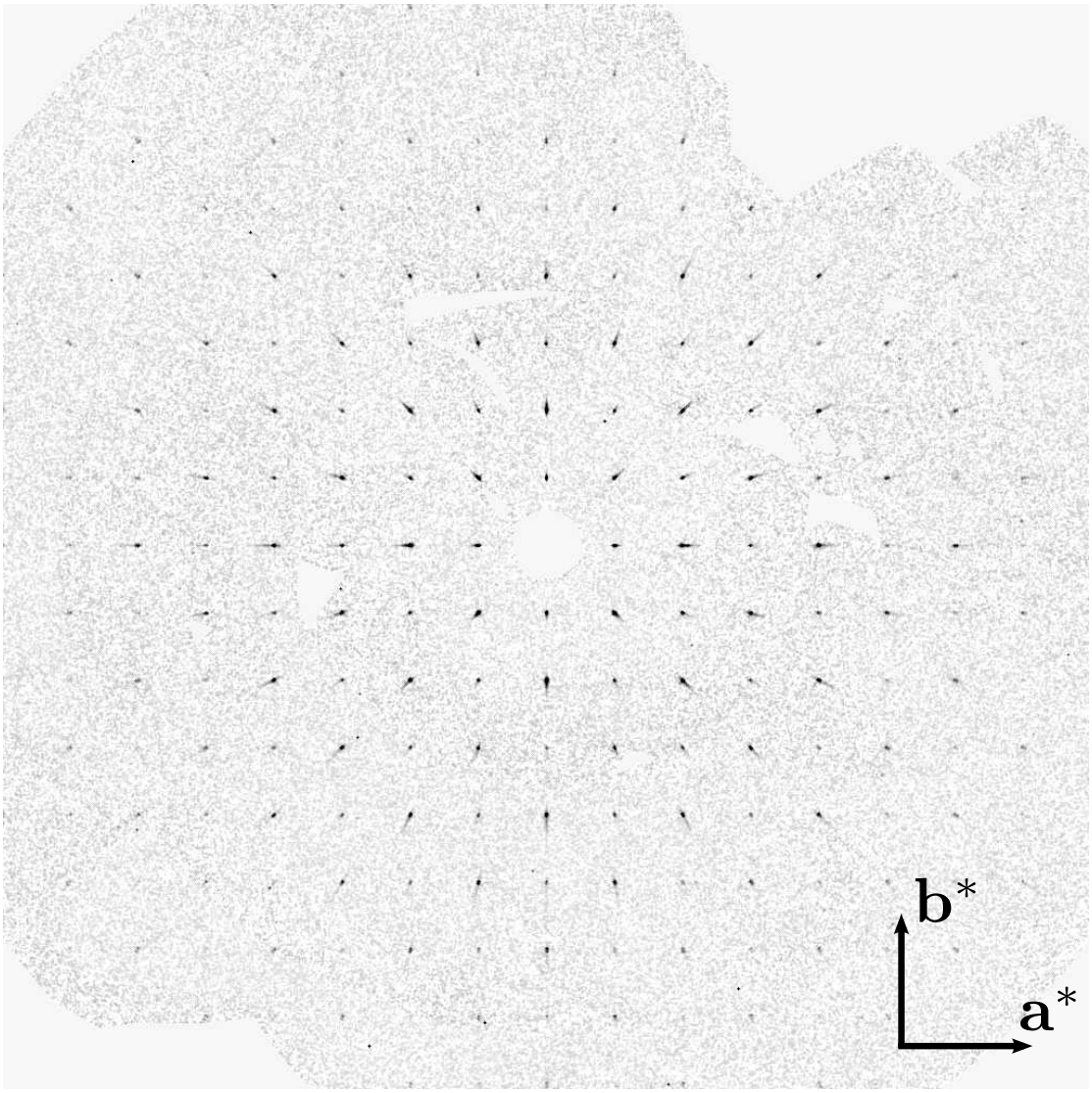

Figure A-1: Unwrapped equivalent precession image of the $hk0$ reciprocal lattice plane in $BaTiO_3$

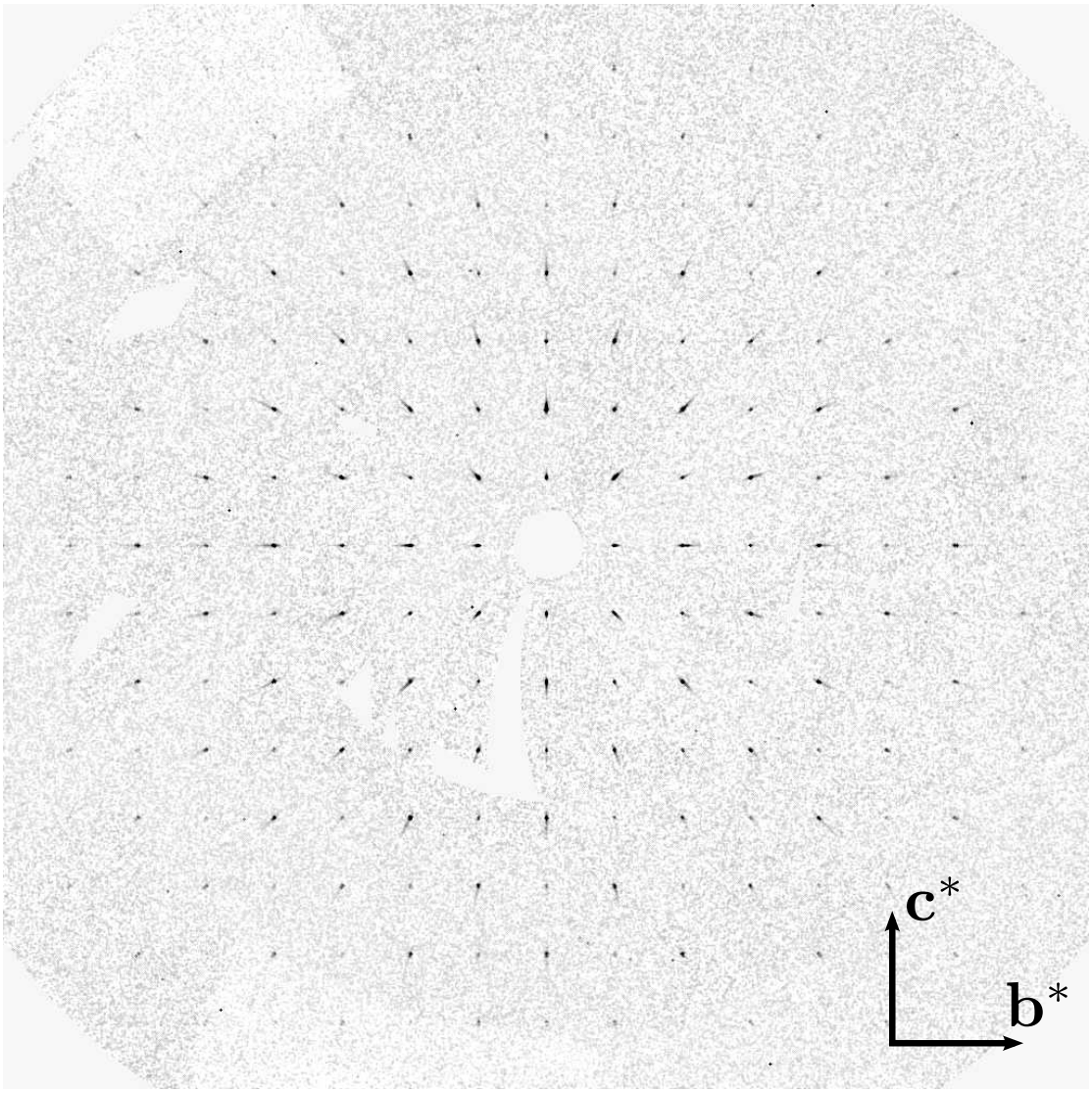

Figure A-2: Unwrapped equivalent precession image of the $0kl$ reciprocal lattice plane in $BaTiO_3$

Appendix B

Example Topas input file

An example topas input file for powder refinement.

```
'Powder Refinement
r_wp  9.952 r_exp  2.127 r_p  6.104 r_wp_dash  14.780 r_p_dash  12.032 r_exp_dash  3.159
weighted_Durbin_Watson  0.146 gof  4.679
chi2_convergence_criteria 0.0001 'convergence limit for refinement to stop
do_errors 'shows errors on refined parameters
iters 100000 'how many loops to process for the refinement

xdd 10-70-15hr_0.006_1500s_1.xy 'inputting data file
x_calculation_step = Yobs_dx_at(Xo); convolution_step 4 'reads the data into topas
bkg  @  1530.1995‘_3.21133218 -1958.14129‘_5.99508415  1228.36414‘_5.5683394 -707.56146‘_5.33465536  318.442094‘_5.0257485
CuKa1(0.0001)
LP_Factor(27.3)
Radius(240)
Specimen_Displacement(@,-0.05798‘_0.00547)
Zero_Error(zero, 0.00336‘_0.00253)
Absorption(abscorr, 74.69047‘_1.83464)

str
a lpa  5.51417‘_0.00007
b lpb  5.51275‘_0.00007
c lpc  25.07065‘_0.00015
al 90
be 90
ga 90
volume  762.102947‘_0.0141853856
space_group "A21am"

site Sr1 x !sr1x 0                y sr1y  0.24080‘_0.00060 z !sr1z 0              occ Sr+2  Srocc  0.7646‘_0.0031
                                                                                  beq cat_beq  0.8035‘_0.0390
                                                                                  occ Bi+3 = 1 - Srocc; :  0.2354‘_0.0031
                                                                                  beq cat_beq  0.8035‘_0.0390
site Bi2 x bi1x  0.50851‘_0.00107 y bi1y  0.73260‘_0.00020 z bi1z 0.20060‘_0.00004 occ Bi+3 = Srocc/2 + 0.5; :  0.8823‘_0.0016
                                                                                  beq cat_beq  0.8035‘_0.0390
                                                                                  occ Sr+2 = 1 - (Srocc/2 + 0.5); :0.1177‘_0.0016
                                                                                  beq cat_beq  0.8035‘_0.0390
site Nb1 x @  0.48190‘_0.00103    y @  0.75105‘_0.00059    z @  0.41363‘_0.00006   occ Nb+5 1.
                                                                                  beq nb_beq  0.4007‘_0.0765
site O1  x @  0.43732‘_0.00433    y @  0.20593‘_0.00424    z 0                     occ O-2  1.
                                                                                  beq o_beq  0.5439‘_0.2139
site O2  x @  0.46687‘_0.00391    y @  0.78751‘_0.00261    z @  0.35003‘_0.00041   occ O-2  1.
                                                                                  beq o_beq  0.5439‘_0.2139
site O3  x @  0.71925‘_0.00436    y @ -0.01392‘_0.00686    z 0.2500                occ O-2  1.
                                                                                  beq o_beq  0.5439‘_0.2139
site O4  x @  0.66028‘_0.00314    y @  0.98369‘_0.00361    z @  0.08751‘_0.00049   occ O-2  1.
                                                                                  beq o_beq  0.5439‘_0.2139
site O5  x @  0.72128‘_0.00521    y @  0.98146‘_0.00430    z @  0.57139‘_0.00043   occ O-2  1.
                                                                                  beq o_beq  0.5439‘_0.2139

scale @  0.000130408181‘_4.84e-007
r_bragg  2.92988911

TCHZ_Peak_Type(@, 0.02381‘_0.00113,@,-0.01965‘_0.00086,@, 0.00518‘_0.00015,, 0,@, 0.06631‘_0.00050,, 0)
```

Appendix C

Publications

The following published papers contain work which is submitted as part of this thesis.

Goff, Richard J. and Keeble, Dean and Thomas, Pamela A. and Ritter, Clemens and Morrison, Finlay D. and Lightfoot, Philip;
Leakage and proton conductivity in the predicted ferroelectric $CsBiNb_2O_7$;
Chemistry of Materials, **21**, 1296, (2009).

Keeble, D. S. and Thomas, P. A.;
On the tetragonality of the room-temperature ferroelectric phase of barium titanate, $BaTiO_3$;
J. Appl. Cryst., **42**, 480, (2009).